KAUNAS UNIVERSITY OF TECHNOLOGY

ALEKSANDRAS ŠEVČIK

MONTE CARLO SIMULATION AND EXPERIMENTAL VERIFICATION OF PHOTON RADIATION-INDUCED POLYMERIZATION IN DOSIMETRIC MATERIALS

Doctoral dissertation
Technological sciences, Materials engineering (T 008)

Kaunas, 2024

This doctoral dissertation was prepared at Kaunas University of Technology, Faculty of Mathematics and Natural Sciences, Department of Physics during the period of 2018–2023.

Scientific Supervisor:
Prof. dr. Diana ADLIENĖ (Kaunas University of Technology, Technological Sciences, Materials Engineering, T 008).

Edited by: English language editor Dovilė Blaudžiūnienė (Publishing House *Technologija*), Lithuanian language editor Rozita Znamenskaitė (Publishing House *Technologija*).

The public defense of the dissertation will be held at 1 p.m. on 12 April, 2024 at the public meeting of the Dissertation Defense Board of Materials Engineering Science Field in Rectorate Hall at Kaunas University of Technology.

Address: K. Donelaičio 73-402, Kaunas LT-44249, Lithuania.
Phone: (+370) 608 28 527; email doktorantura@ktu.lt

The doctoral dissertation was sent out on 12 March, 2024.
The doctoral dissertation is available on the internet at http://ktu.edu and at the library of Kaunas University of Technology (Gedimino 50, Kaunas LT-44239, Lithuania).

KAUNO TECHNOLOGIJOS UNIVERSITETAS

ALEKSANDRAS ŠEVČIK

FOTONŲ SPINDULIUOTĖS SUKELTOS POLIMERIZACIJOS DOZIMETRINĖSE MEDŽIAGOSE MONTE-KARLO MODELIAVIMAS IR EKSPERIMENTINIS TYRIMAS

Daktaro disertacija
Technologijos mokslai, medžiagų inžinerija (T 008)

2024, Kaunas

Disertacija rengta 2018–2023 metais Kauno technologijos universiteto Matematikos ir gamtos mokslų fakultete, Fizikos katedroje.

Mokslinė vadovė:
prof. dr. Diana ADLIENĖ (Kauno technologijos universitetas, technologijos mokslai, medžiagų inžinerija, T 008).

Redagavo: anglų kalbos redaktorė Dovilė Blaudžiūnienė (leidykla „Technologija“), lietuvių kalbos redaktorė Rozita Znamenskaitė (leidykla „Technologija“).

Medžiagų inžinerijos mokslo krypties disertacijos gynimo taryba:
prof. habil. dr. Arvaidas GALDIKAS (Kauno technologijos universitetas, technologijos mokslai, medžiagų inžinerija, T 008) – **pirmininkas**;
prof. habil. dr. Juozas Vidas GRAŽULEVIČIUS (Kauno technologijos universitetas, technologijos mokslai, medžiagų inžinerija, T 008);
vyr. m. d. dr. Gediminas STANKŪNAS (Lietuvos energetikos institutas, gamtos mokslai, fizika, N 002);
prof. habil. dr. Sigitas TAMULEVIČIUS (Kauno technologijos universitetas, technologijos mokslai, medžiagų inžinerija, T 008);
prof. habil. dr. Piotr ULAŃSKI (Lodzės technologijos universitetas, Lenkija, gamtos mokslai, chemija, N 003).

Disertacija bus ginama viešame Medžiagų inžinerijos mokslo krypties disertacijos gynimo tarybos posėdyje 2024 m. balandžio 12 d. 13 val. Kauno technologijos universiteto Rektorato salėje.

Adresas: K. Donelaičio g. 73-402, Kaunas LT-44249, Lietuva.
Tel. (+370) 608 28 527; el. paštas doktorantura@ktu.lt

Disertacija išsiųsta 2024 m. kovo 12 d.
Su disertacija galima susipažinti interneto svetainėje http://ktu.edu ir Kauno technologijos universiteto bibliotekoje (Gedimino g. 50, Kaunas LT-44239).

CONTENTS

LIST OF FIGURES

LIST OF TABLES

LIST OF ABBREVIATIONS

3D	Three Dimensional
ABS	Acrylonitrile Butadiene Styrene
BNCT	Boron Neutron Capture Therapy
CG	Coarse-Grained
CT	Computed Tomography
CUDA	Compute Unified Device Architecture
DD	Percent Dose Difference
DOSXYZnrc	Dose Distribution Using XYZ Directions (Code)
DFT	Density Functional Theory
DTA	Distance-To-Agreement
EBT3	(Acronym for the radiochromic film type)
FFF	Flattening Filter Free
FLUKA	Fluktuierende Kaskade (Code)
GEANT4	Geometry And Tracking 4 (Code)
HZETRN	High Charge And Energy Transport (Code)
IAEA	International Atomic Energy Agency
ICRP	International Commission On Radiological Protection
IHEP	Institute Of High Energy Physics
KMC	Kinetic Monte Carlo
MAA	Methacrylic Acid
MC	Monte Carlo
MCNP	Monte Carlo N-Particle Transport Code
MCS	Monte Carlo Simulations
MD	Molecular Dynamics
MIT	Massachusetts Institute of Technology
MKL	Math Kernel Collection
MOM	Method Of Moment
MPI	Message Passing Interface
MRI	Magnetic Resonance Imaging
NASA	National Aeronautics And Space Administration
OARs	Organs At Risk
OpenMP	Open Multi-Processing
PAA	Poly(acrylamide) Polymer
PDD	Percentage Depth Dose
PDF	Probability Distribution Function
PEG	Poly(ethylene Glycol)
PEEK	Poly(etheretherketone)

PES	Potential Energy Surface
PENELOPE	Penetration And Energy Loss Of Positrons And Electrons (Code)
PHITS	Particle And Heavy Ion Transport Code System
PLP	Pulse Laser Polymerization
PLP-SEC	Pulse Laser Polymerization With Size Exclusion Chromatography
PMMA	Polymethyl Methacrylate
PVA	Poly(vinyl Alcohol)
QA	Quality Assurance
RCF	Radiochromic Film
RNG	Random Number Generator
RTQA2	(Acronym for the radiochromic film type)
SEC	Size Exclusion Chromatography
TVs	Target Volumes

1. INTRODUCTION

1.1. The relevance of the doctoral dissertation

Orthovoltage therapy is highly used in the field of radiation oncology. It involves the use of X-rays with energies typically ranging to 400 kiloelectron volts (keV). These X-rays have a relatively low penetrating power and are mainly used to treat superficial tumors located near the surface of the body as well as head and neck cancers [1]. In certain cases, when near critical structures, orthovoltage therapy may be selected to minimize radiation exposure to healthy tissues and is effective in delivering radiation to shallow depths.

One major concern is the lack of dependable dose planning systems, which impedes accurate therapy delivery. Dose planning is crucial to optimize treatment, target tumor volumes accurately, and reduce radiation exposure to healthy tissues. The development of reliable dose planning systems tailored to orthovoltage therapy is essential for improving treatment precision and safety. Furthermore, the presence of teeth or jaw implants, or other high density foreign bodies creates complex cases for the optimal dose deliveries. These geometric variations can perturb the radiation beam, leading to dose inhomogeneities and uncertainties. Accurate understanding of the radiation dose distribution in the presence of such complexities is vital for effective treatment planning. Clinicians can utilize this technology to enhance treatment strategies, predict potential complications, and guarantee precise delivery of the prescribed dosage to the intended area, all while minimizing harm to neighboring healthy tissues. This is where the Monte Carlo (MC) simulation model comes in, providing a vital tool for addressing these issues.

MC simulation serves as a key tool in radiation therapy research and clinical practice, providing accurate modeling and prediction of radiation dose distributions. In the context of orthovoltage therapy, MC simulation allows for precise calculation of dose distributions by simulating photon interactions and tracking the path of radiation within the patient's anatomy. This simulation technique incorporates material properties, geometry, and radiation transport processes, providing valuable insights into the impact of complex geometries and metal artifacts on dose perturbations.

Experimental verification is essential to validate the simulation results and ensure their clinical relevance. Combining MC simulation with experimental data enables a comprehensive and robust approach to investigating photon radiation-induced polymerization and its implications in orthovoltage therapy. Experimental verification contributes to the validation and refinement of simulation models, enhancing their accuracy and reliability. One commonly used method for experimental verification is the utilization of radiochromic films. These films consist of a radiochromic material that undergoes a color change proportional to the absorbed radiation dose. By placing radiochromic films within a phantom or patient-specific geometry, the dose distribution can be measured and compared with the simulated

results. This method provides a practical and cost-effective way to validate the dose calculations and assess the accuracy of the MC simulation model.

Another approach for experimental verification is the use of 3D polymer gel dosimeters. These dosimeters are made of radiation-sensitive gel materials that alter their physical properties upon exposure to radiation. The gel dosimeters can be shaped to mimic complex anatomical structures and provide three-dimensional dose distribution information. By comparing the measured dose distribution from the gel dosimeters with the simulated results, researchers can validate the accuracy and reliability of the MC simulation model and verify the delivered dose to the targets.

It is essential to have a robust method for comparing the data obtained from MC simulations with experimental results. One widely used technique for dose distribution comparison is the gamma index analysis. The gamma index evaluates the level of similarity between the measured and computed dose distributions, taking into account both the discrepancies in dose values and the proximity requirements. By defining threshold values for dose difference and distance-to-agreement, the gamma index provides a quantitative assessment of the agreement between the simulated and experimental dose distributions. A low gamma index value indicates a high level of agreement between the simulated and measured dose distributions, providing confidence in the reliability of the simulation results. A high gamma index value suggests discrepancies between the simulated and measured data, highlighting the need for further investigation and refinement of the simulation model. The convenient tool to compare the results from simulations and experimental verifications is necessary.

3D gel dosimetry represents a cutting-edge technique with immense potential as the only method to experimentally capture the radiation field in three dimensions. In contrast to conventional dosimeters that only measure dose at specific points or in a 2D plane, gel dosimeters offer comprehensive spatial data regarding absorbed dose distribution throughout the entire volume. This capability allows for precise validation of intricate treatment plans. One of the main challenges that must be addressed to ensure reliable and accurate results lies in understanding the complicated radical polymerization process that occurs under irradiation. The absorbed radiation causes polymerization and crosslinking of the monomers, leading to changes in the physical properties of the gel. This polymerization process should be well investigated to accurately interpret the outcome of the irradiated polymer gel for comparison with biological tissue irradiation. The various models are used to analyze the mechanisms of radical polymerization.

Specifically, when it comes to understanding the polymerization under radiation exposure, the existing knowledge and available models are relatively scarce and mainly limited to the kinetic models [2]. This scarcity arises from the intricate nature of radical-initiated polymerization, which involves numerous chemical reactions and kinetics that are challenging to capture accurately. In polymer engineering, MC simulations enable the modeling of different polymer characteristics such as chain length, branching, monomer sequence, functionality, and cross-linking density[3]. However, the majority of the research studies that utilize MC in polymerization

research focus on the projection of some properties of macromolecular polymer chains of known properties, meaning that the initial size and branching characteristics are known[4]. Another significant area of study, which is more aligned with polymer chemistry rather than polymer physics, focuses on predicting specific properties of the polymer. A novel contribution is presented in this work by introducing a coarse-grained MC model that simulates the polymerization of approximately 6,000 methacrylic acid monomers under irradiation, in which the initial parameters are derived from quantum chemistry calculations. The model we have developed exhibits the potential for wide-ranging applications across different materials and conditions, making it highly versatile and suitable for various scenarios in the context of radical polymerization. This versatility and adaptability indicate its potential for generalization, making it applicable in diverse contexts within the field of radical polymerization.

1.2. The aim of the doctoral dissertation

The aim of this work is to investigate low energy deposition in heterogeneous media with complicated geometry using polymer-based dosimeters and Monte Carlo simulations. A focus is placed on developing an MC-based computational model for assessing radiation-induced polymerization dynamics.

1.3. Tasks of the doctoral dissertation

1. Investigate orthovoltage X-ray energy distributions in complicated irradiation scenarios containing metal artifacts and validate the simulation results with experimental methods.
2. Develop and experimentally validate a software tool for calculating 2D-dose/distance index (2DDI) in orthovoltage X-ray therapy.
3. Develop a novel Monte Carlo code for simulating radiation-induced polymerization, with the ability to analyze structural changes within the material.

1.4. Statements carried out for defense

1. MC simulation with polychromatic beam model and a virtual phantom geometry minimizes energy distribution uncertainties in orthovoltage X-ray therapy when high-density artefacts are presented.
2. A developed gamma-index-based software tool enables quantitative comparison of different dosimetry methods in orthovoltage X-ray therapy.
3. The novel developed Monte Carlo model provides valuable insights into radiation-induced polymer dynamics, allowing to quantify polymer growth parameters.

1.5. Novelty of this work

The initial part of this research focuses on the potential of MC simulation (MCS) in addressing challenges faced in orthovoltage and superficial X-ray therapy. While the impact of metal implants on megavoltage beam therapies has been on research for a while, this study aims to be the first to analyze the dose discrepancies caused by such implants during orthovoltage X-ray therapy by utilizing the Fluka MC simulation

package and 3D printed models [A1]. By better understanding the impact of high-density implants and by providing more accurate dose assessments, the proposed approach can significantly enhance treatment efficacy and patient safety.

Specialized in-house derived software tool is introduced to quantitatively compare different dosimetry methods in orthovoltage therapy, allowing for the comparison of simulated results with irradiated radiochromic films[A2]. The significance of this approach lies in its potential to prevent errors and increase confidence in the accuracy of recommended treatments in unique situations involving metal objects, thus improving quality assurance (QA) techniques. The overall objective is to contribute to a better understanding of the difficulties caused by metal implants in X-ray therapy.

A new coarse-grained (CG) MC model from scratch is developed, which allows to simulate the polymerization process in hydrogels under the influence of external radiation [A3]. The model has been meticulously designed and implemented using the C++ programming language, specifically targeting high-performance computing (HPC) clusters. The model allows visualizing the probable polymer structures in 3D and examines the distribution of polymer chains, network density, and other structural properties and is capable of graphically presenting the predicted structure of polymeric networks. It may help to increase the understanding of the polymerization process in hydrogels under external radiation and could be a valuable tool to the purpose of creating new dosimetric gels with improved characteristics and performance for use in a variety of applications, including radiation treatment and dosimetry.

1.6. The object and methodology

The research work benefitted from the utilization of various tools, methods, and contributors, including:

FLUKA, a widely used MC simulation program, was employed for modeling the transport of photons and electrons. Known for its versatility, FLUKA is the primary MC tool employed at CERN.

Radiochromic EBT3 and RTQA2 films were utilized in the experimental investigations.

The PMMA phantom, employed in the experimental setup, was made by Severina Paukštytė at Kaunas Oncology Hospital.

The 3D printed phantom, employed in the experimental setup, was created by Benas Gabrielis Urbonavičius and Ieva Masiulytė at Kaunas University of Technology.

The irradiation procedures were conducted using the X-ray therapy unit GULMAY D3225 by Jurgita Laurikaitienė at Kaunas Oncology Hospital.

Quantum chemistry calculations, serving as input for the MC polymerization model, were performed by Žilvinas Rinkevičius at KTH Royal Institute of Technology, Stockholm. Žilvinas Rinkevičius also provided consultations during the development of the MC polymerization model.

1.7. Author's contribution

The author has developed software tools to compare various radiation dosimetry techniques as well as a computer program that simulates the growth of polymers when exposed to radiation.

All simulations have been performed at Kaunas University of Technology/Lithuania and using resources of KTH Royal Institute of Technology (Sweden). The investigation of results and comparisons with experimental research was performed in collaboration with other co-authors.

1.8. PhD thesis approbation

The main results of doctoral dissertation were published in five scientific publications: three papers related to dissertation topic were published in journals included in Clarivate Analytics Web of Science database, and two papers were published in the conference proceedings included in CA WoS data base. A. Ševčik was the first author in all CA WoS publications.

Additionally, five diverse conference articles, abstracts, and posters have been presented at international conferences.

1.9. The structure of doctoral dissertation

The dissertation consists of five chapters. The first chapter describes the relevance of the doctoral dissertation, its aim and tasks, the author's contribution, a methodology, contributors, an approbation, and novelty of the work. The second chapter includes literature overview related to the newest information about MC simulations, the existing codes and their framework, the applications of such simulations, and brief theoretical foundation. The instruments and methodology described in third chapter presents the used experimental means, materials as well as used computational resources. The fourth chapter presents the results and their interpretation. The dissertation is completed with the conclusions in the fifth chapter.

At the end of the work, a compilation of references, an annex, a list of scientific publications, and published journal articles are provided, together with acknowledgements and author's CV. The dissertation consists of a total of 148 pages, including 50 figures and 9 tables, 271 references.

2. LITERATURE REVIEW

This review provides an overview of the current advancements in the respective fields and is divided into two main sections. The first part describes the fundamentals of MCS of radiation transport, the second part introduces polymer hydrogels and their studies and outlines the state-of-the-art in the attempt to simulate polymerization under the action of added energy.

2.1. MC simulations of radiation transport

MCS are widely used in various fields to model and predict the behavior of systems with a high degree of complexity. These simulations involve the use of random sampling techniques to calculate the probability of various outcomes and are well-suited for solving problems in which the underlying physics is complex or uncertain. The following section of the literature review provides a thorough overview of the use of MC simulations to address problems related to radiation (energy) transport in matter. This review is divided into three parts: (1) a general overview of MC simulation codes and their applications; (2) a discussion of the fundamental principles of MC simulations of radiation transport and (3) MC simulations of energy transport in inhomogeneous media with the application in X-ray therapy treatment of patients with metal artefacts inside.

2.1.1. Fundamentals of MC simulations of radiation transport

MCS is based on repeated random sampling from probability distributions representing the possible physical interactions applicable for the simulation. The independently simulated histories are summed up and post-processed to a numerical solution of the problem based on the defined geometry, materials, and the cross sections for the relevant interactions [5].

The MC method is used to solve the equations of radiation transport when analytical, spectral, or numerical quadrature integration solutions are not applicable. It can treat arbitrary radiation fields and geometries efficiently and often is the only applicable solution in radiation transport problems. The MC simulation of a particular experimental configuration is a probabilistic technique that entails the computational creation of random events.

Simulating these events necessitates an "interaction model," which is essentially a compilation of differential cross sections associated with the relevant interaction mechanisms. These cross sections determine the probability distribution functions (PDF) of the random variables that describe a track:

- free path between consecutive interaction events,
- type of interaction taking place,
- energy loss and angular deflection in an event,
- initial state of emitted secondary particles if any.

Upon determining these Probability Density Functions (PDFs), random trajectories can be generated through the application of appropriate sampling techniques. These histories are tracked in arbitrary geometries, and each track

accumulates the contribution to statistical estimator of the chosen physical observables.

If a substantial number of histories are generated, the law of large numbers facilitates the extraction of quantitative data on the transport process by averaging across the simulated histories.

A phase space of a dynamical system is a space in which all possible states of a system are represented, with each possible state corresponding to one unique point [6]. Each phase space dimension corresponds to a particle degree of freedom. Generally, three dimensions correspond to position in real space, another three dimensions represent the moment of the particle, the other dimensions are the particle type itself, evolution time, quantum numbers, etc. Each particle is characterized by a point in a phase space, and the overall number of particles in an infinitesimal phase-space region can be expressed:

$$dN = f(x,p,t,\alpha)d^3pd^3xdtd^n\alpha, \quad (1)$$

where:

dN: the differential number of particles.

- $f(x,p,t,\alpha)$: the particle distribution function, where:
  - x: position vector.
  - p: momentum vector.
  - t: time.
  - α: additional particle properties (like spin, charge).
- d^3p: differential volume in momentum space.
- d^3x: differential volume in real space.
- dt: differential time element.
- $d^n\alpha$: differentials of other particle properties.

Particle transport is reflected through the evolution of $f(x,p,t,\alpha)$ due to transport, scattering, particle absorption, decay, external forces, particle production, and other related factors [7]. This evolution is described by Boltzmann's transport equation [8]. The equilibrium equation in phase space posits that at any point within this space, the incremental change in angular flux Ψ within an infinitesimally small phase space volume is equivalent to the sum of all incoming particles subtracted by the sum of all outgoing particles. If we name the initial particle distribution function in a given phase space region as source, while a phase space region where the modified $f(x,p,t,\alpha)$ is to be calculated is to be a detector, the solution can be written as:

$$f(x,p,t,\alpha) = \iint G(x,p,\alpha,x',p',\alpha')f_0(x',p',\alpha')d^3p'^{d^3}x'\,d^n\alpha' \quad (2)$$

where:

- $f(x,p,t,\alpha)$: the particle distribution function.
- $G(x,p,\alpha,x',p',\alpha')$: a multi-dimensional operator that includes all the microscopic processes.

- (x',p',α'): initial distribution function.
- $'d^3p'$, $'d^3x'$, $'d^n\alpha'$: differential volume elements in momentum space, real space, and for other properties, respectively.

It may be seen as the solution to any particle transport problem is a multi-dimensional integral in which all processes are described by probability distributions. The simplest solution can be written as an integral of $f(x,p,t,\alpha)$ over the region of interest:

$$N = \iint_{\Delta p \Delta x \Delta \alpha} f(x,p,t,\alpha) d^3p d^3x d^n\alpha \quad (3)$$

where:

- N: the total number of particles within specific ranges of momentum (Δp), position (Δx), and other properties ($\Delta\alpha$).
- $f(x,p,t,\alpha)$: the particle distribution function.
- d^3p, d^3x, $d^n\alpha$: differential elements in momentum space, real space, and for additional properties, respectively.

The solution of the actual problem involving scattering, absorption, various interactions, etc. involves complex integrations in many variables and makes a numerical solution hardly achievable. Multidimensional numerical integration is required to solve the system of coupled transport equations for problems in radiation therapy, for example, for dose calculation, and similar.

The MC method serves as an integration technique that enables the solution of multi-dimensional integrals by sampling from a well-suited stochastic distribution. The fundamental concept behind MC simulation involves utilizing random samples of parameters or inputs to analyze the behavior of a complex system or process. The mathematical foundation of this method is Central Limit Theorem (CLT) which states the arithmetic mean of a sufficiently large number of iterates of independent random variables, each with finite expected value and finite variance, will be approximately normally distributed [9]. In other words, if there is an observable quantity x that can be represented as the outcome of combining multiple random processes, the average value of x can be calculated by sampling numerous x values based on the probability distributions of the random processes.

The accuracy of MC estimator depends on the number of samples [5]:

$$\sigma \propto \frac{1}{\sqrt{N}} \quad (4)$$

where:

- σ: standard deviation,
- N: denotes the number of observations or trials in a dataset or experiment.

The foundation of MC integration lies in the random sampling from probability distributions associated with the outcomes of physical events. This is achieved through the utilization of pseudo-random numbers, which are sequences generated by mathematical algorithms that emulate the uniform distribution. Various sampling

methods are subsequently employed to obtain the desired values for analysis. Being named as the most accurate simulation method MC is often used as a reference method to verify the dose distribution. The simulation gives the flexibility to include various parameters such as different media properties and complex geometries and is equivalent to the experiment itself due to the stochastic nature of the radiation itself. The unbiased analogue MC simulation takes a huge amount of time but allows it to be used as "black box" with care. Analogue MC samples actual phase space distributions and gives a prediction of all statistical moments of any order and average quantities. In addition, it preserves correlations and reproduces fluctuations in the most accurate way.

General photon interaction processes that should be simulated by a photon MC code [7,9,10] consist of:

- Photoelectric interaction;
- The Compton interaction;
- Pair production;
- The Rayleigh interaction.

The dominant low energy photon process is the photoelectric effect. In this process, a photon transfers all its energy to an electron located in one of the atomic shells. A photoelectron is ejected if the photon energy exceeds the electron's binding energy.

The electron shell that best satisfies the constraint and exhibits the highest binding energy is the most probable candidate for electron loss. However, quantifying the probability of this interaction is a complicated operation that requires the application of quantum mechanics for accurate calculations.

The general cross section formulae as a function of the photon energy E_γ:

$$\sigma_{ph}(E_\gamma) \propto \frac{Z^m}{E_\gamma^n}, \tag{5}$$

where Z is the atomic number and *m* ranges from 4 (energy below 100 keV) to 4.6 (energy above 500 keV), and *n* ranges from 3 (energy below 100 keV) to 1 (energy above 500 keV). Most MC codes use a tabulated data for the photoelectric interaction. Angular distributions of the photoelectron can be determined according to the theory of Sauter [11].

The Compton interaction refers to the inelastic scattering of a photon off an electron in an atomic nucleus shell. It occurs when electromagnetic radiation interacts with a free electron, resulting in energy transfer to the electron. The energy range involved in this process requires the use of relativity and quantum mechanics to derive accurate expressions for the cross section. At large energies, the Compton interaction approaches asymptotically:

$$\lim_{\alpha\to\infty} \sigma_{inc}(\alpha) = \sigma_0^{inc} \frac{Z}{\alpha}, \tag{6}$$

where $\sigma_{inc}(\alpha)$= 3.33^{-25} cm^2/nucleus and is directly proportional to Z and decreases as $1/E_\gamma$, α is the ratio of the photon's energy to the rest energy of the electron. The Compton cross section decreases with increased energy. At low energies, the Compton cross section becomes:

$$\lim_{\alpha \to 0} \sigma_{inc}(\alpha) = 2\sigma_0^{inc} Z\,, \tag{7}$$

where Z represents the atomic number. In all applications, the electrons are bound to atoms and this binding has a profound effect on the cross section at low energies. Nevertheless, once the photon energy surpasses approximately 100 keV, the bound electrons can be approximated as "free," allowing for the neglect of atomic binding effects. This threshold is determined by the energy of the K-shell, although these effects can still have an impact above it, particularly for low atomic number (Z) elements. Below this energy, the cross section is reduced since the K-shell electrons are too tightly bound to be liberated by the incident photon. The cross section for the scattering of a photon with energy $h\nu$ at a given angle θ was initially derived in 1928 by Klein and Nishina using the Dirac theory of the electron within the lowest order Quantum Electrodynamics, without any further approximations. The expression for the differential cross-section for scattering of photons by a single free electron is:

$$\frac{d\sigma_{KN}}{d\Omega} = \frac{r_0^2}{2}(1 + cos^2\theta) f_{KN} \tag{8}$$

Where:

- r_0: Classical electron radius;
- θ: Scattering angle;
- f_{KN}: Klein-Nishina function, which depends on the energy of the incident photon and the scattering angle;
- Ω: Solid angle.

When a high-energy photon comes close to an atomic nucleus, it can interact with the nuclear Coulomb field through a process known as pair production. In this process, the photon is transformed into an electron-positron pair, each possessing its own kinetic energy. However, pair production can only occur for photons with energies greater than the energy threshold of $2m_0c^2$= 1022 keV, where m_0 is the rest mass of an electron and c is the speed of light. As pair production takes place in the presence of the nucleus, the cross-section for this interaction is proportional to the square of the nuclear charge, denoted as Z. Consequently, materials composed of high atomic number elements are more prone to converting photons into charged particles compared to materials with lower atomic numbers. The high-energy limit of the pair production cross section per nucleus takes the form:

$$\lim_{\alpha \to \infty} \sigma_{pp}(\alpha) = \sigma_0^{pp} Z^2 \left(\ln(2\alpha) - \frac{109}{42}\right), \tag{9}$$

where:

- σ_0^{pp}: A constant related to the proton-proton cross-section.
- Z: The atomic number.

When a high energy photon passes near to an orbital electron, the photon may interact with the Coulomb field of this electron by a process called triplet production. The target electron, in this case, is ejected with a significant amount of energy. As a result, two electrons and one positron are set into motion as a consequence of the pair production process. The energy threshold for triplet production is $4m_0c^2$.

The other interaction that needs to be discussed is Rayleigh interaction, also known as coherent scattering. In coherent scattering, the photon transfers momentum to the atom and is scattered at an angle θ without losing any energy. The scattering by individual electrons is in phase, resulting in an interference pattern that is specific to the atom and determines the angular distribution of the scattered photons. In terms of cross-section, the Rayleigh cross section for coherent scattering is typically at least an order of magnitude lower than the cross section for photoelectric interactions. The Rayleigh differential cross section has the following form:

$$\sigma_{coh}(E_\gamma\Theta) = \frac{r_e^2}{2}(1 + cos^2\Theta)[F(q,Z)]^2 \quad (10)$$

where:

- r_e is the classical electron radius (2.8179E^{-13} cm),
- q is the momentum-transfer parameter, $q = (E/hc)\ sin(\Theta/2)$, and
- $F(q,Z)$ is the atomic form factor.

The simplified version of photon transport logic is illustrated in **Fig. 1**.

To simplify the simulation, certain assumptions are made. Electron creation is neglected, and the transport is considered to take place within a single volume element and a single medium. At the beginning of the simulation, the initial parameters of the photon are defined and stored in an array known as the stack, which retains the phase space characteristics of the particles for processing.

During the simulation, the transport of a particle is terminated if it exits the geometry of interest or if its energy falls below a predetermined minimum energy, also known as the cut-off parameter. If the particle's energy is above the cut-off, the distance to the next interaction site is determined. If the photon has left the volume of interest, it is discarded. Otherwise, the branching distribution is sampled to determine which interaction will occur. The surviving particles have their energies, directions, and other characteristics chosen from the appropriate distributions. Finally, the suitable cross-section tables must be chosen and assigned to each material in the simulation geometry. The modern cross-section data are based on quantum mechanical models of each scattering and absorption process. The approximate models of orbital electron wave functions are used, with validation from available experimental measurements [12].

The transport of electrons and positrons is significantly more problematic than for photons. The interactions of these charge particles can be divided to two groups [9]: “hard” events, which can be sampled discretely within a reasonable amount of computing time for a wide range of practical problems; and the so called “soft” events, which are accounted in a cumulative sense including the effect of many such interactions at the same time. These are the so-called “statistically grouped” interactions.

- “Hard” events:
  - large energy-loss Møller scattering ($e-e- \rightarrow e-e-$),
  - large energy-loss Bhabha scattering ($e+e- \rightarrow e+e-$),
  - hard bremsstrahlung emission ($e\pm\_N \rightarrow e \pm \gamma N$),
- positron annihilation “in-flight” and at rest ($e+e- \rightarrow \gamma\gamma$).
- “Soft events”:
- low-energy Møller (Bhabha) scattering (modeled as part of the collision stopping power),
- atomic excitation (modeled as another part of the collision stopping power),
- soft bremsstrahlung (modeled as radiative stopping power), and
- elastic electron (positron) multiple scattering from atoms

Bremsstrahlung refers to the emission of electromagnetic radiation that occurs when a charged particle undergoes deceleration due to its interaction with another charged particle. During this process, the moving particle loses kinetic energy, which is then converted into a photon. The primary mode of interaction for bremsstrahlung is with the atomic nucleus. The deceleration and subsequent acceleration of an electron as it scatters off nuclei can be highly energetic, leading to the generation of photons with very high energies, including up to the total kinetic energy of the incoming charged particle. The total cross section depends approximately like $1/E\gamma$. Model formulae is described through Koch and Motz’s as well as Tsai’s works [13,14].

Møller and Bhabha scattering involve the collision of incident electrons or positrons with atomic electrons. In the case of $e-e+$ pair, the electrons can undergo annihilation and recreation, which introduces an additional interaction channel to the cross section. However, for $e-e-$ collisions, the primary electron can only transfer a maximum of half its energy to the target electron due to the indistinguishability of the two electrons. In the $e+e-$ case, the positron can transfer all its energy to the atomic electron. The Møller and Bhabha cross sections exhibit scaling with the atomic number (Z) for different media. The cross section is approximately scaled as $1/v^2$, where v is the velocity of the scattered electron. Compared to bremsstrahlung, Møller interactions produce a greater number of low-energy secondary particles. Electron-positron annihilation refers to the collision between an electron (e-) and a positron (e+). At lower energies, this collision results in the mutual annihilation of the electron and positron, leading to the creation of energetic photons. Two-photon “in-flight” annihilation can be modeled using the cross section formulae of

Heitler[15]. It is conventional to consider the atomic electrons to be free, ignoring binding effects.

The energy loss resulting from soft bremsstrahlung and soft collisions can be effectively considered by assuming a continuous loss of energy along the path of the particle. Bethe-Bloch theory of charged particle energy loss is used formalism as expressed by Berger and Seltzer [16] and in ICRU-37 [17]. In the process of continuous energy loss, the contribution from collisions increases with the atomic number (Z) of the medium, while the radiative part increases with Z^2. Additionally, charged particles have the ability to induce polarization in the medium they traverse. This phenomenon, known as the "density effect," becomes significant at high energies and for dense media. Default density effect parameters are available from NIST tables [18]. Atomic binding effects are coarsely treated by the Bethe-Bloch formalism which assumes that each electron can be treated as if it were bound by an average binding potential.

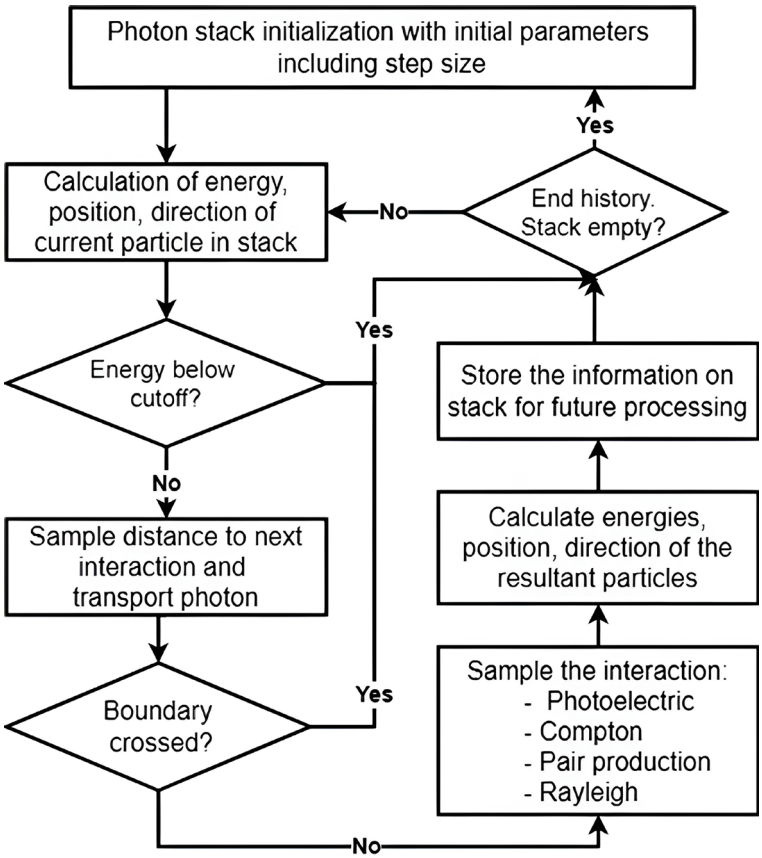

Fig. 1 Simplified photon transport model scheme

The elastic scattering of electrons and positrons from nuclei is primarily characterized by small-angle scattering events, with occasional occurrences of large-angle scattering. Multiple scattering phenomena are addressed by various statistical theories. For example, the simulation package FLUKA incorporates a modified version of the Moliere theory. The standard Moliere theory accounts for single-event large-angle scattering, such as electron backscattering from individual atoms. However, the Moliere theory does not differentiate between the scattering of electrons and positrons and employs screened Rutherford cross sections to describe the scattering process. A typical MC electron track simulation is shown in **Fig. 2**. When an electron traverses through a medium, it continuously loses energy due to interactions with subthreshold knock-on electrons and bremsstrahlung. To accurately simulate the electron's path, it is divided into small straight-line segments known as multiple scattering steps. The length of these sub-steps can be adjusted to ensure that the electron loses a specified portion of its energy during each step. At the end of each step, the multiple scattering angle is determined based on a theoretical distribution. In some cases, a catastrophic event may occur, such as the emission of a single knock-on electron, which subsequently initiates motion in other particles. These secondary particles are then individually tracked using the same methodology.

If the original electron does not fall below the transport threshold, it continues to be transported, undergoing subsequent steps until it completes its trajectory.

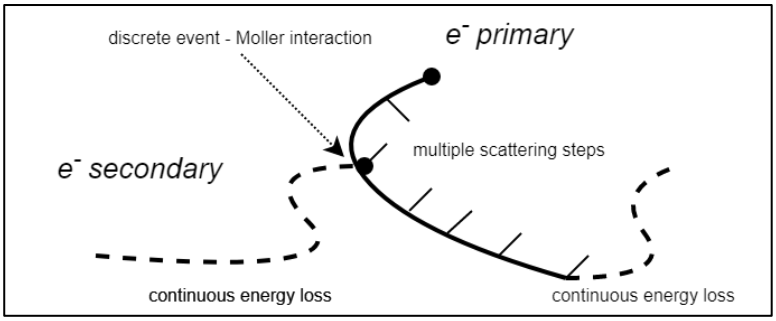

Fig. 2. A basic electron track simulation example

To sum up the principles of MC simulation of radiation transport, a localized collection of particles at time moment can be described as radiation field, in which each particle contains position r, energy E, and direction Ω described with polar angle θ and azimuthal angle φ. Each particle can go through various interaction processes that can be characterized by a differential cross section. The solution to such radiation field is given by the transport equation that can efficiently be solved by MC method. Basic MC algorithm for radiation transport can be described in the following way:

- Initialize the stack of primary particles with known position and momentum.
- Start the cycle with particle from the stack:
  - If particle is within material boundary, determine the total interaction cross section at present energy in that material.
  - Evaluate the mean free path to the interaction.

- Sample step length to the interaction.
- Determine the interaction mechanism.
- Sample the change of energy and direction from differential cross section of the selected interaction mechanism.
- Update the energy and direction of the particle and add generated secondary particles to the stack if any.
- Record the history of particle regarding desired physical observables.
- Repeat the cycle until particle energy drops below set energy threshold or particle exits the geometry.

- Start new cycle with another particle from the stack.

2.2. Applications of MC simulations of radiation transport

Applications of MCS of radiation transport have a very broad spectrum, which will be briefly discussed here, touching on the most important areas in which these simulations serve as an indispensable tool. The descriptions and fundamentals of MCS itself are provided in section 2.1.1.

MCS packages

The following are the cutting-edge MCS packages used for energy transfer: EGSnrc, Geant4, Fluka, Penelope, MCNP, MCX, PHITS, GATE, Shield-HIT, HZETRN, and RITRACKS.

Developed by the National Research Council of Canada, EGSnrc (Electron Gamma Shower - nrc) is a MC simulation package that is widely used for dose calculation in radiation therapy [19,20]. It is highly accurate and can be used to simulate a broad range of radiation sources. It can simulate the propagation of photons, electrons, and positrons with kinetic energies between 1 keV and 10 GeV. In the fields of particle physics, medical physics, and environmental science, EGSnrc is used extensively. It is a basis for DOSXYZnrc and BEAMnrc packages that is specifically designed for the simulation of external photon and electron beams. It is widely used for dose calculation in radiation therapy and has been validated for use in clinical treatment planning systems. A wide range of external photon and electron beams can be simulated, including megavoltage X-ray beams, electron beams, and bremsstrahlung photon beams. The packages have been validated for use in clinical treatment planning systems, making it a reliable tool for use in patient treatment.

Geant4 (GEometry ANd Tracking 4) is a MC simulation toolkit that is developed and maintained by CERN [21–23]. It is widely used in the field of high energy physics, but it also has applications in medical physics, including dose calculation in radiation therapy. Geant4 includes a large library of cross-section data and physical models that are needed to accurately simulate the transport of particles in different materials. It is capable of simulating a wide range of physical phenomena, including particle interactions, energy deposition, and material damage. It has an additional toolkit Geant4-DNA [24–27] which is specifically designed for simulating the interactions of ionizing radiation with DNA molecules and cellular structures. It

can be used to study the effects of radiation on cells and tissues and is commonly used in the fields of radiation biology and medical physics.

Developed by the European Organization for Nuclear Research (CERN), FLUKA (FLUktuierende KAskade) [28–31] is a MC simulation program that is widely used for simulating the transport of particles, including photons, electrons, and protons. It is a general-purpose simulation program that is capable of simulating a wide range of physical phenomena, including particle interactions, energy deposition, and material damage. It is commonly used in a variety of fields, including particle physics, nuclear engineering, medical physics, and environmental science. FLUKA is highly accurate and has been validated against a wide range of experimental data and was used as the main radiation particle transport simulation tool in this thesis. A thorough description of this MCS package is provided in Chapter 2 Instruments and Methods.

PENELOPE (Penetration and Energy LOss of Positrons and Electrons) [32] is a MC simulation package developed by the Spanish National Research Council and is specifically designed for the simulation of low-energy photons and electrons. Penelope is extensively used in a variety of fields, including medical physics, material science, and nuclear engineering, making it a good choice for researchers looking to compare their results with those of others. Penelope can be used to model a wide range of physical processes, including particle transport in solids, gases, and liquids, as well as radiation transport in various media.

Developed by Los Alamos National Laboratory, MCNP-X (MC Neutron-Particle eXtended) [33,34] is a general-purpose MC simulation code that is widely used for a variety of applications, including dose calculation in radiation therapy. The code is versatile in that it can assist the general-purpose transport of many different kinds of particles. This comprises not just neutrons, photons, and electrons, but also ions and a variety of additional fundamental particles with energies up to 1 TeV per nucleon. It is used in a variety of fields, including particle physics, nuclear engineering, medical physics, and environmental science. MCNP is highly accurate and has been validated against a wide range of experimental data. It also includes a set of tools for analyzing and visualizing simulation results, making it a potent instrument for a variety of applications.

Developed by the Massachusetts Institute of Technology (MIT), MCX (MC eXtreme) [35–37] is a MC simulation program that is specifically designed for simulating the transport of photons in complex geometries. This is a simulation software specified for the three-dimensional transport of photons in heterogeneous media. By taking advantage of the abundant parallel threads and the exceptionally low memory latency characteristic of graphics processing unit (GPU), the software significantly enhances the efficiency of MC (MC) photon simulations. Compared to traditional CPU-based MC implementations, MCX accelerates the process by several hundred to a thousand times.

PHITS (Particle and Heavy Ion Transport Code System) [38–41] is a MC simulation program developed by the Japan Atomic Energy Agency (JAEA). It is designed for simulating the transport of protons and other heavy ions. The latest

version of the software, PHITS 3.02, has been greatly improved and extended in terms of accuracy and the applicable energy ranges, thanks to adjustments to the nuclear reaction models and the integration of new atomic interaction models. The PHITS 3.02 software can manage the transport of electrons and positrons utilizing both condensation history and track-structure methodologies. However, the reliability of the latter is limited to simulations performed in liquid water. To improve user experience, a variety of supportive features have been integrated, such as the inclusion of new tallies designed to acquire statistically superior results, a function for generating radioisotope sources, and an array of software tools tailored to facilitate the application of PHITS in the field of medical physics. Owing to its wide-ranging capabilities, PHITS 3.02 has found extensive application across diverse domains, including but not limited to, accelerator design, radiation shielding and protection, medical physics, and cosmic-ray research.

The GATE26 (OpenGATE Collaboration) is a simulation toolkit that incorporates the GEANT4 libraries and is specifically tailored to the demands of nuclear medicine. It facilitates the simulation of time-dependent processes and detector movements including source decay kinetics, thus enabling the emulation of time curves under practical acquisition conditions. This toolkit finds its major application in emission tomography. GATE26 is a valuable instrument in supporting the development of innovative medical imaging devices, evaluating new image reconstruction algorithms, refining scatter correction techniques, and optimizing scan protocols.

Developed by the Institute of High Energy Physics (IHEP) in China, SHIELD-HIT [42] is a MC simulation program that is specifically designed for simulating the transport of photons in shielding materials by modeling the interactions of ions with the material and predicting the amount of energy deposited in the material as the ions pass through it. SHIELD-HIT can be used to simulate radiation in a variety of shielding materials, including metals, plastics, and concrete, and can be used to optimize the design of shielding materials for a given application.

HZETRN (High Charge and Energy TRaNsport) [43–45] is a MC simulation program designed by the U.S. Air Force Research Laboratory which is specifically designed for simulating the transport of high-energy particles in the Earth's atmosphere and space. HZETRN is commonly used to study the effects of space weather on satellite systems and to predict the radiation environment in space. It contains a huge collection of cross-section data and physical models needed to accurately simulate the transport of ions in various materials, as well as a set of tools for analyzing and displaying simulation results. HZETRN has been validated against a vast array of experimental data and possesses a high degree of precision.

RITRACKS [46] is a simulation code developed at the NASA Johnson Space Center to investigate the effects of ionizing radiation at the atomic scale and to analyze the impacts of space radiation on biological systems. The software is based on the stochastic simulation of radiation track structure of heavy ions, and it is capable of calculating pertinent measures such as radial dose and voxel dose in spherical and cylindrical targets of varied dimensions. Recently, RITRACKS has integrated DNA

structure and damage simulations at the molecular level. This is achieved through a minor adaptation of the pre-existing particle transport algorithms and a sequential diffusion-reaction program premised on the Greens functions of the diffusion equation. This enhancement enables the simulation of both direct and indirect effects of ionizing radiation on DNA.

Application of MCS in radiation therapy: planning, delivery, dosimetry, and quality assurance

From the calculation of fundamental dosimetric values to simulations of radiation treatment planning, the spectrum of MC applications is vast. MCS are widely used in medical physics to model and predict the behavior of ionizing radiation in the body. Their accuracy depends on consistent data, and it is important to recognize and assess the uncertainty factors that accompanies the MC calculations [47].

There are numerous dosimetry systems used for routine measurements in radiotherapy, and most of them have been improved or optimized through the use of MC simulations, including but not limited to ionization chambers [48,49], thermoluminescent dosimeters [50,51], semiconductors [52–54], diamonds [55–57], optically stimulated luminescent dosimeters [58,59], scintillators [58,59], radiochromic films [60,61], and gels dosimeters [62].

MCS are used to evaluate the dosimetric accuracy and radiobiological effectiveness of proton or photon therapy in the treatment of various cancers [63–69] and for automated patient dose calculation systems to obtain an independent dose validation of treatment plans [70–73] and is used to verify the accuracy of treatment planning systems. Various optimization studies are utilizing MCS to significantly improve treatment quality and reduce the planning margin values [74–76] in clinically viable computational times. The MCS is a basis for multimodal treatment planning systems that allow to incorporate several kinds of therapies, including but not limited to boron neutron capture therapy (BNCT), proton therapy, X-ray therapy, and heavy ion therapy [77]. A framework for comparing the precision and uniformity of treatment planning for various therapies has been developed utilizing MCS [78].

MCS can be used to calculate the radiation doses received during certain procedures, such as interventional radiology procedures both for patient [79] or for the medical personnel [80]. The simulations can be used to create patient-specific models of the body, taking into account the specific characteristics of an individual patient's anatomy and the location and size of any tumors [81,82]

The simulations are also heavily used in the brachytherapy field [78,83]. RapidBrachyMCTPS is a novel treatment planning system for brachytherapy that uses MC for dose calculation. It includes a graphical user interface, optimization tools, and a Geant4-based MC engine called RapidBrachyMC [84,85]. GGEMS-brachy is another MCS platform for brachytherapy low dose rate (LDR) applications using graphics processing units (GPUs) [86].

Medical imaging and nuclear medicine

MC simulations are widely used in medical imaging to support the design of new imaging devices, assess the performance of existing imaging systems, and optimize scan protocols. Additionally, he simulations are used to study the distribution and pharmacokinetics of radiopharmaceuticals in the body. Today, MC simulations are an important tool in the field of nuclear medicine imaging, both in single-photon emission computed tomography (SPECT) and positron emission tomography (PET) [87–90]. MC simulations can be used to optimize the design of PET scanners and to predict the performance of different scanner configurations [91,92] and assess the performance of CT scanners, including their spatial resolution, contrast-to-noise ratio, and dose efficiency [93]. MCS can be used to optimize scan procedures in medical imaging, including the selection of radiotracer, injection rate, and scan duration [94,95].

New imaging techniques, such as new reconstruction algorithms or scatter correction methods, can be assessed with the utilization of MCS and their performance in different imaging scenarios can be predicted [96,97]. Simulations permit predicting the radiation dose administered to patients during medical imaging exams and modifying the dose to limit patient risks while retaining image quality [98,99]. MCS are an essential tool in targeted radiotherapy applications. In these applications, a radiopharmaceutical is designed to bind specifically to cancer targets, allowing for the selective irradiation of tumor cells, while sparing healthy tissues [100] and assessing the effectiveness of numerous nano-sized radiosensitizers [101–103].

Radiobiology and radiochemistry

MCS are used to study the effects of ionizing radiation on biological systems, including DNA damage response (DDR) [104–107]. DDR refers to the mechanisms that cells use to repair or remove damaged DNA in order to maintain the integrity of their genome, where the simulations provide detailed, quantitative information about the interactions of ionizing radiation with biological systems at different scales, ranging from small DNA segments to populations of cells. MCS is also used to estimate the risk of developing cancer or other health effects following exposure to ionizing radiation [108,109]. This can be useful for informing radiation protection guidelines and for understanding the potential health impacts of radiation exposure in different populations. In addition, the MCS are useful in assessing the impacting factors in the radiotherapy, such as oxygen role in the damage response, including estimates of oxygen consumption rates and investigations of oxygen depletion during the chemistry stage of radiolysis [110,111]. Radiochemistry further utilizes the simulations to analyze the production and properties of various radiopharmaceuticals [112,113].

Summary

MCS plays a crucial role in the field of radiation physics. It provides researchers with the means to simulate and comprehend the dynamics of radiation and its

interactions with matter across diverse scenarios. MCS are used in a variety of applications, including medical purposes such as radiotherapy and medical imaging, as well as in the design of shielding materials and in fundamental research in experimental physics. The aforementioned list only touches the surface of the numerous applications of MCS in radiation physics. It is an essential tool for researchers studying this field, as it provides a way to accurately model and understand the behavior of radiation and its interactions with matter in a variety of contexts.

2.3. Use of Monte Carlo Simulations in X-ray therapy in the presence of metal artefacts

The first part of this work, which used the MC simulation package to analyze the effects of radiation on the material, in addition to the baseline studies, specifically focused on clinically relevant practical issues. Standard superficial and orthovoltage radiotherapy treatment planning software does not accurately account for the presence of metal artefacts in the irradiation field, leading to reduced accuracy of the treatment delivery to the tumor. MC simulation software can be used to validate dosimetric data.

Orthovoltage X-ray therapy is used to treat superficial or near-surface tumors or skin lesions [114–121]. Few software resources are available for dose planning or visualization in low-energy X-ray therapy, and various other means are used to evaluate dose discrepancies in the complicated cases [122,123]. MC simulations are used in the orthovoltage therapy to replicate the functions of treatment planning systems (TPS) used in megavoltage therapy and predict the dose distribution in the patient's body, thus optimizing the delivery of radiation therapy to the tumor and minimizing the risk of side effects [124–126].

The delivered dose largely depends on the density of the media in which the radiation beam propagates. The dose assigned at the patient in orthovoltage radiotherapy is calculated through absolute dose calibration using a water phantom. However, differences in the delivered and prescribed doses can arise due to anatomical changes in the patient. MCS allows to evaluate the effect of heterogeneity of the medium and estimate the possible dose discrepancies [127,128]. Breast dose in mammography is approximately 30% lower when realistic, heterogeneous glandular distributions are taken into consideration [129], while other reports state even bigger deviations if heterogeneity of the medium is not taken into account in the X-ray - radiotherapy [130].

High-density objects, such as metal implants or implants made from other high-density materials, can significantly affect the dose distribution during radiotherapy treatment. This can lead to underdosing or overdosing of the targeted tissue, potentially diminishing the effectiveness of the treatment, and increasing the risk of side effects. The study [131] that examined the effect of high-density objects on dose distribution used Geant4/GATE to simulate the treatment of orthopedic implants, specifically titanium and PEEK (polyetheretherketone) implants. The findings of this study indicate that high dose gradients were present along the boundaries of the titanium implants, a phenomenon that was not observed for the

corresponding PEEK implants. The dose to the internal cavities of the titanium implants was also found to be enhanced by 10–15%. These findings suggest that the presence of high-density objects can significantly alter the dose distribution in the treatment area and highlight the importance of considering their impact on the treatment planning process.

The high atomic number and density of dental implants present significant challenges in accurately delivering a dose of radiotherapy and accurately contouring tumors and organs in the head and neck region [132]. This is due to the artifact that is created by these implants, which can disrupt the normal distribution of the radiation and hinder the ability to accurately visualize and target the affected tissue. In the same study, it was demonstrated that MC simulation is an effective method for determining the dosage distribution in heterogeneous media. It aimed to assess the effect of titanium dental implants on the dose distribution of high-energy X-rays and gamma rays in head and neck cancer patients using MC simulation. The presence of the implants was found to cause differences in the dose distribution and significant scattering of the radiation, particularly in the bone in direct contact with the implant. These findings suggest that dental implants should be taken into consideration by therapists when planning radiation treatment to prevent the potential risk of osteoradionecrosis. Sarigul [133] examined the influence of field size on the percentage depth dose (PDD) in heterogeneous media exposed to 6 MV flattening filter free (FFF) radiation using MC simulation and the AXB algorithm. The results showed that when metal materials were placed in a water phantom, there was a rapid increase in dose immediately before the surface of the metal, while the dose after the metal materials was found to be affected by the field size, with a greater effect observed for materials with a higher atomic number. These findings suggest that the field size should be taken into consideration when using radiation in the presence of metal materials, particularly those with high atomic numbers, in order to accurately deliver the desired dose.

Kim et al. [134] confirms that the presence of dental metal artifacts in computed tomography (CT) data sets used for planning radiation therapy in the head and neck region can result in discrepancies in the doses received by organs at risk (OARs) and target volumes (TVs) when compared to a reference data set that more accurately represents the patient's anatomy. Specifically, these artifacts can cause relative hot spots in OARs and relative cold spots in TVs.

Rousselle et al. [134] highlights that the presence of metal artifacts can significantly impact three main areas of radiotherapy: the treatment of prostate cancer in patients with hip implants, the treatment of spinal metastases in patients with stainless steel or titanium rods, plates, screws, and/or spinal fusion cages, and the treatment of head and neck cancers in patients with dental fillings or implants. These artifacts can cause image degradation and present challenges in the treatment planning process. Nonetheless, there is a significant gap in medical data regarding the direct impact of metallic hardware on local tumor management and the rate of adverse effects in normal tissues among cancer patients who have metallic implants.

2.4. Modelling of radiation-induced polymer growth

Polymer hydrogels have gained significant attention in recent years due to their unique properties, such as high sensitivity to irradiation and similarity to the tissues. These characteristics make them well-suited for use as dosimetric gels, which are materials used to measure and evaluate radiation doses in a variety of applications.

This section of the literature review focuses on the state-of-the-art research in the field of polymer hydrogels, specifically their use as three-dimensional dosimetric gels. The review is divided into three main parts: (1) the use of polymer hydrogels in dosimetry; (2) the fundamental principles of polymer hydrogel growth mechanisms, including the various factors that influence the growth and structural properties of these materials; and (3) an overview of current frameworks for polymer growth models which involve the use of mathematical and computational tools to predict and analyze the growth of the polymer chains and their structural properties.

2.4.1. Polymer hydrogels and their application. Methacrylic acid

Polymer hydrogels are hydrophilic, three-dimensional polymeric networks that can absorb large amounts of water or other polar solvents [135,136]. They are highly porous, soft, and flexible materials that can mimic the structure and function of natural hydrogels, such as cartilage and tissue. There are several methods for manufacturing polymer hydrogels, including physical, chemical, and biological approaches. Physical methods involve the mechanical entanglement or crosslinking of polymer chains through processes such as freezing and thawing [137,138], solvent evaporation [139,140], or irradiation [141–143]. Chemical methods involve the chemical crosslinking of polymer chains through the use of various chemical agents [144,145]. Biological methods include the enzymatic crosslinking of polymers through the use of proteins or enzymes [146], or the production of hydrogels through the fermentation of microorganisms [147,148].

There are many types of polymers that can be used to make hydrogels, including natural polymers such as collagen [149], chitosan [150,151], and alginate [152,153], and synthetic polymers such as poly(acrylamide) [154], poly(ethylene glycol) [155], and poly(vinyl alcoho)l [156,157], or even a combination of them[158,159]. The choice of polymer depends on the desired properties of the hydrogel and the intended application in various fields, including medicine [160,161], food science [162,163], agriculture [164], and environmental engineering [165]. Polymer gels have gained significant attention in recent years for their potential use in three-dimensional (3D) dosimetry, which involves the measurement and evaluation of radiation doses in three-dimensional space. Polymer gel dosimeters are made of radiation-sensitive compounds that polymerize in response to the absorbed radiation dose when exposed to radiation [166].One area of research has focused on the use of polymer gels as dosimetric media for medical imaging [167–169] and radiation therapy [170–173]. 3D dosimeters have distinct advantages over one-dimensional dosimeters like ion chambers and two-dimensional dosimeters like film, which is especially important in dosimetry

settings with steep dose gradients like intensity-modulated radiation treatment (IMRT) and stereotactic radiosurgery [174,175]. These gels can be used to evaluate the spatial distribution of radiation doses within the body, providing valuable information for the optimization of treatment plans and the assessment of treatment outcomes. Polymer gels possess the capacity to replicate the physical and chemical characteristics of human tissue, making them suitable as tissue-equivalent phantoms for radiation dosimetry purposes. These gels can be formulated in two main ways: Fricke-type gels [176] or monomers dispersed in a gelatinous medium [177]. There are several different kinds of polymers used for that purpose: methacrylic acid, polyacrylamide polymer, polyethylene glycol, polyvinyl alcohol, and others.

Methacrylic acid (MAA) have been used in several studies as a potential material for polymer gel dosimetry due to their good radiation sensitivity and ability to create stable gels [178–180]. However, it is relatively expensive compared to some other polymers that are commonly used in polymer gel dosimetry, such as polyacrylamide. In addition, MAA-based polymers can be sensitive to humidity, which can affect their stability and accuracy.

Poly(acrylamide) polymer (PAA) is widely used in polymer gel dosimetry due to its high radiation sensitivity and low cost [181–183]. It is also relatively easy to prepare and handle. PAA has good mechanical properties and is able to maintain its shape and structure during the dosimetry process. This is important for maintaining the accuracy and reliability of the dosimetry measurements.

Polyethylene glycol (PEG) polymer is highly hydrophilic and can be used to create polymer gels that are stable and easy to handle[184–186]. PEG is relatively nontoxic and has a low potential for causing adverse effects in patients. This makes it a safe choice for use in polymer gel dosimetry.

Polyvinyl alcohol (PVA) polymer has high stability, non-toxicity, sensitivity, and ease of manufacture. It is used in radiochromic (Fricke-type) gels [187,188] which demonstrate high sensitivity and dose rate independence. The results are consistent and the reproducibility of the outcomes between different batches is very high. Some of the gel combinations are reversible by heating treatment and can be re-used [189].

Irradiation of various gel types leads to alterations in proton relaxation rates that are directly proportional to the absorbed dose. These changes can be visualized using magnetic resonance imaging (MRI) techniques [190,191]. Furthermore, the gels undergo color variations and/or become opaque upon irradiation, enabling the application of optical tomography methods [192–194]. Another area of research has focused on the development of novel polymer gel formulations with improved physical and chemical properties for use in 3D dosimetry. This includes the optimization of the water content, swelling behavior, and mechanical properties of polymer gels, as well as the incorporation of various types of nanoparticles and other materials to enhance their dosimetric performance, such as inorganic salts [195,196] or nanoparticles [197–199].

Methacrylic acid (MAA) is a colorless liquid organic monomer compound with the chemical formula $CH_2=C(CH_3)CO_2H$ that contains a carboxylic acid group, which can be ionized in solution to form a negatively charged carboxylate ion.

Methacrylic acid has a pungent odor and is highly reactive, making it a suitable building block for a wide range of chemical compounds. In recent years, significant progress has been made in the field of controlled and living polymerization techniques, which allow for the synthesis of highly defined polymer structures, including graft copolymers, star polymers, and polymer brushes [200]. This has led to a growing interest in the synthesis and characterization of complex polymer systems that contain (meth)acrylic acid segments.

These polymers have the potential to be customized with respect to their chemical structure and three-dimensional architecture, enabling their use in a diverse range of applications. These applications include the stabilization of colloids, modification of crystal growth, induction of micelle formation, and development of intelligent materials. In scientific research, methacrylic acid is polymerized to form poly(methacrylic acid), a type of hydrogel with unique properties. These properties include biocompatibility, biodegradability, and swelling behavior, which make poly(methacrylic acid) hydrogels well-suited for use in drug delivery [201], tissue engineering [202], and wound healing applications [203,204].

2.4.2. Polymer chain-growth and branching of MAA

The degree of branching of polymers can significantly influence their properties, ranging from dendritic long chains to compact, soft nanoparticles [200]. The degree of branching (DB) is a measure of the extent to which a polymer chain branches off from the main chain. A high degree of branching can result in polymers with a more compact, soft structure, while a low degree of branching can result in polymers with a more linear, rigid structure. It is challenging to study the properties of methacrylic acid polymers with a high degree of branching, or a high degree of polymerization, due to the complexity of their structure and the difficulty of synthesizing well-defined branched polymers.

Radical polymerization is a type of polymerization in which a growing polymer chain is initiated by a radical species, which is a highly reactive atom or molecule with an unpaired electron [205,206]. Radical polymerization can occur through several mechanisms, including chain-growth polymerization, in which monomers are added to a growing radical chain, or step-growth polymerization, in which monomers react to form a polymer network through chemical bonds. In this introduction, we will concentrate on the MAA polymer, which is well-known in gel dosimetry and whose polymerization mechanisms are well characterized. A classical radical polymerization method involves six separate steps: chain initiation, propagation, disproportionation, combination, chain transfer to monomer, and chain transfer to solvent [207].

During the polymerization of methacrylic acid, the double bond between the first and second carbon atoms in the methacrylic acid molecule opens up, allowing the monomers to link together. This process can occur through different mechanisms, including free radical polymerization, in which a free radical initiator participates [208]. This initiator generates free radicals, which are highly reactive species with unpaired electrons. These free radicals attack the double bond of the methacrylic acid monomer, breaking the bond and creating a new radical on the growing chain. This

process repeats, with monomers continuously adding to the growing chain until the desired polymer length is achieved. The polymerization mechanism in under irradiation is similar to that of traditional free radical polymerization. The generated free radicals react with methacrylic acid monomers by abstracting a hydrogen atom from the double bond.

The bond dissociation energies relevant for the (poly)MAA material [209]:

- C-C (single carbon–carbon bond): ~3.6 eV.
- C-O (carbon atoms singly bound to oxygen): ~3.7 eV.
- C=O (carbon atoms with double bonds to oxygen atoms): ~7.7 eV.
- C-H (carbon-hydrogen bond): ~4.3 eV.

Low energy photons engage with the material mainly via the photoelectric effect and Compton scattering which results in the generation of ions and electrons. The interactions between electrons and monomers transpire in less than a nanosecond [210]. The degree of polymerization can be influenced by regulating the radiation dose rate, thus controlling the kinetic chain length of the propagation process. The radiation-induced polymerization can cause various reactions among the generated free radicals on polymer chains, which induce modifications in the polymer's structure or functionality.

The simplified mechanism of the polymerization [210] consists of the following parts: initiation, propagation, termination, chain transfer, cross-linking, chain scission, and secondary reactions.

Initiation. Chain initiation is the first step of the polymerization process, in which a radical species is generated through the action of a radical initiator. The radical initiator can be a chemical compound that generates radicals through a thermal or photochemical reaction, or it can be an external source of radiation, such as UV light or X-rays. When the monomer solution, composed of water and methacrylic acid, is irradiated, high-energy photons can cleave water molecules to generate hydroxyl radicals (•OH) and hydrogen atoms (•H). The transfer of energy in the form of Coulombic interactions happens within a timescale of approximately 10^{-18} to 10^{-12} seconds [210]. This brief timeframe is characterized by the formation of ionized and excited molecules localized along the paths of the interacting particles. These molecules, localized along the trajectories of the interacting particles, can interact with the methacrylic acid monomers within the solution. The interactions create C-centered radicals—carbon atoms with unpaired electrons—which initiate the polymerization process by readily removing hydrogen atoms from the polymer's backbone or attaching to unsaturated bonds. For example, for an initiator molecule *I*, the initiation step can be represented as:

$$I \rightarrow 2R^{*}, \tag{11}$$

where:

- *I*: The initiator, a compound that decomposes to start the polymerization process.
- $R*$: The radical generated from the initiator, which is reactive and initiates the polymerization by reacting with monomers.

Here, *I* denotes the initiator, and *R** represents the generated radicals, which subsequently react with monomer units *M* to initiate a polymer chain:

$$R^* + M \rightarrow RM^*, \quad (12)$$

where:

- *R∗:* The radical generated from the initiator,
- *M*: A monomer unit,
- *RM∗*: The initial radical polymer unit, representing the first step in forming the polymer chain.

The efficiency of initiation is characterized by the quantum yield Φ, which is the number of initiation events per photon absorbed. It also should be noted that Eq.12 could also be seen as part of the propagation step already.

The rate coefficient of this step is significantly influenced by the density of ionizing radiation acting on the sample but is also influenced to a lesser extent by other parameters, the kind of initiator radical playing the most significant role. For MAA monomer, the most significant rate coefficients are achieved by peroxy or carbon-centered radicals [211], where the first type of radicals are directly generated by radiolysis of water and the second type of radicals are generated by the interaction of the peroxy radicals with the gel matrix. Peroxy radicals are highly reactive chemical species that are characterized by the presence of an unpaired electron and a carbonyl group (-O-O-), and they are highly reactive due to the presence of the unpaired electron. Peroxy radicals are formed through various mechanisms, including the radiolysis of water [212]. They can initiate the polymerization process by reacting with monomers, or they can transfer their unpaired electron to other species through a process called radical transfer. The rate coefficient, which is the speed at which a chemical reaction occurs, of the step of radical polymerization started by ionizing radiation is significantly impacted by the intensity of the radiation acting on the sample. However, other factors can also have an effect, with the type of initiator radical being the most influential. For the monomer acrylic acid, the highest rate coefficients are achieved through the use of peroxy or carbon-centered radicals. Peroxy radicals are produced directly through the radiolysis of water, while carbon-centered radicals are generated through the interaction of peroxy radicals with the gel matrix. Overall, the choice of initiator radical plays a crucial role in determining the rate coefficient of radical polymerization for MAA monomer.

Propagation. It is the second step of the polymerization process, in which the radical species generated in the initiation step reacts with a monomer to form a growing polymer chain. The radical species is converted to a stable species and a new radical species is generated, which can then react with another monomer to continue the polymerization process. The reactive radical *RM** can further react with other monomer units in a process termed propagation, which can be represented as:

$$RM^* + M \rightarrow RMM^*, \quad (13)$$

where:

- *RM∗*: The initial radical polymer unit;
- *M*: A monomer unit;
- *RMM∗*: A longer radical polymer chain, formed by adding another monomer unit to the initial radical polymer unit.

The radical site, denoted by *, remains at the end of the growing polymer chain, and it continues to react with more monomer units.

Size exclusion chromatography (SEC) in conjunction with pulse laser polymerization (PLP) has been used extensively to study the rate coefficient of the polymerization process [213,214]. PLP involves the use of short bursts of laser energy to initiate and drive the polymerization process, allowing for the observation of the kinetics of polymerization and the elucidation of the mechanisms underlying the process. SEC is a separation technique that separates molecules based on their size and shape. It uses a stationary phase made up of beads or particles with pores of a specific size. Smaller molecules pass through the pores of the stationary phase with greater ease than larger molecules, resulting in a separation based on size. By combining pulse laser polymerization with size exclusion chromatography (PLP-SEC), the rate of polymerization and the factors that influence it can be studied as well as the size and shape of the resulting polymers. One limitation of PLP-SEC technique is that it is unable to distinguish between diverse types of MAA polymers, such as single chained and branched polymers. This can result in a wide range of estimates for the rate coefficient depending on the specific experimental conditions. Additionally, PLP-SEC measurements do not consider the potential variability of the rate coefficient with respect to the length of the polymer chain (P_n). However, it has been shown that this rate coefficient depends on the length of the polymer chain up to a specific length, and the rate coefficient becomes constant for longer polymer chains [207].

Chain Transfer: this stage involves the transference of the free radical from the growing polymer chain to another species, halting the growth of the original polymer chain while commencing the growth of a new one. This can manifest through various mechanisms, such as transfer to a monomer *M*, solvent *S*, or another polymer *P*, depicted as:

$$RMM^* + M \rightarrow RMMH + M^*, \quad (14)$$
$$RMM^* + S \rightarrow RMMH + S^*, \quad (15)$$
$$RMM^* + P \rightarrow RMMH + P^*, \quad (16)$$

where:

- *RMM∗*: A radical polymer chain;
- *M*: A monomer unit;
- *RMMH*: A non-radical polymer chain (termination product);
- *M∗*: A radicalized monomer (new radical formed);
- *RMM∗*: A radical polymer chain;
- *S*: A solvent or another species;

- $S*$: A radicalized solvent or species (new radical formed);
- P: Another polymer chain or a different species;
- $P*$: A radicalized polymer chain or species (new radical formed).

In chain transfer to monomer unit, the radical species transfers from the growing polymer chain to a monomer molecule, resulting in the initiation of a new polymer chain. This process effectively "breaks" the original polymer chain and starts a new one. In contrast, in chain transfer to solvent, the radical species transfers from the growing polymer chain to a solvent molecule, resulting in the termination of the polymer chain. Both mechanisms can occur multiple times during the polymerization process and can affect the molecular weight distribution and other properties of the resulting polymers. The rate of these processes is typically controlled by the concentration of the monomer or solvent, the concentration of the radical species, and the nature of the radical species.

The MMA polymers form dendrimeric structures via intramolecular and intermolecular transfer mechanisms [207] (**Fig. 3**). In the polymerization of MMA under γ-irradiation, secondary reactions such as the formation of reactive groups and cross-linking are less prevalent. Instead, the intramolecular transfer mechanism is favored, which involves the transfer of carbon-centered radicals from the main chain of the MMA polymer to the MMA monomer unit. This process typically leads to the formation of short MMA side branches with lengths ranging from 1–5 MMA monomers. In contrast, the intermolecular transfer mechanism, which involves the participation of two MMA polymers, is a less probable branching mechanism. However, the size of the participating polymers can result in the formation of longer branches in dendrimeric MMA polymers. Overall, under normal conditions, the formation of short branches is the dominant mechanism for the growth of dendrimeric MMA polymers. However, under γ-irradiation, the intermolecular mechanism becomes more prominent due to the increased availability of carbon-centered radicals and the increased mobility of individual MMA polymers.

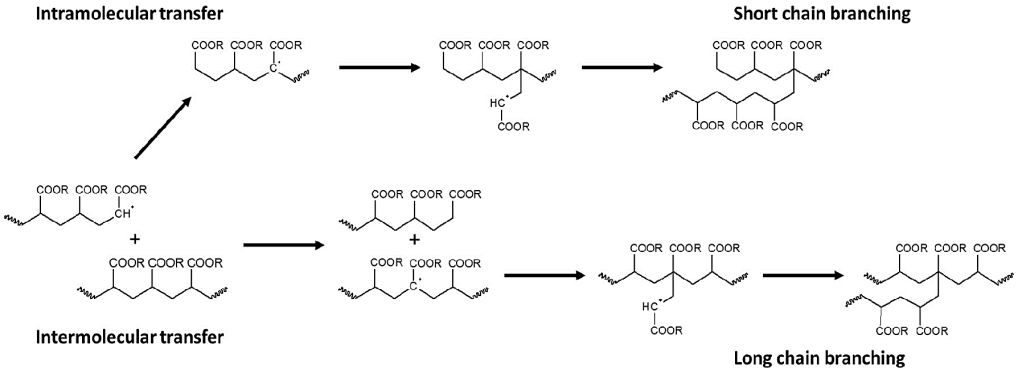

Fig. 3. Intermolecular and intramolecular branching mechanisms of COOR group containing polymers, like the MMA polymer. Figure taken from [207]

Termination: this process ends the growth of polymer chains, either by combination or disproportionation. In disproportionation process the two radical species react with each other to form a new radical species and a stable species. This step can occur if the concentration of radical species is high enough, and it serves to regulate the rate of polymerization. It competes with the combination step in which two radical species react with each other to form a stable species, terminating the polymerization process. For combination, two radicals react to form a single molecule, represented as:

$$RM* + RN* \rightarrow RMN, \quad (17)$$

where:

- $RM*$: A radical polymer chain;
- $RN*$: Another radical polymer chain;
- RMN: A combined non-radical polymer chain (termination product).

For disproportionation, a hydrogen atom from one radical is transferred to another, represented as:

$$RM* + RN* \rightarrow RMH + RN, \quad (18)$$

where:

- $RM*$: A radical polymer chain;
- $RN*$: Another radical polymer chain;
- RMH, RN: Two separate non-radical polymer chains (termination products).

Cross-linking. Cross-linking encompasses the formation of covalent bonds between two polymer chains. In intramolecular cross-linking, C-centered radicals within the same polymer chain react with neighboring sites, establishing covalent bonds within different segments of the same polymer molecule, creating a three-dimensional network within the polymer chain. Intermolecular cross-linking occurs when radicals from different polymer chains interact, forming bonds between the chains, connecting separate polymer chains and forming a three-dimensional network throughout the material. In our model, we consider only intermolecular cross-linking.

Chain Scission. This process involves the breaking of a polymer chain into smaller chains. It can occur through random chain scission or specific processes like beta-scission. Beta-scission describes the bond breakage between two adjacent sites on a polymer chain, which generates two separate free radicals, splitting the polymer chain. For beta-scission, the cleavage can be represented as:

$$RMM* \rightarrow RM* + M*, \quad (19)$$

where:

- $RMM*$: A radical polymer chain;
- $RM*$: A shorter radical polymer chain (degradation product);
- $M*$: A radicalized monomer (new radical formed).

Secondary reactions. These can include various processes like additional intramolecular and intermolecular reactions, cyclization, and rearrangement reactions, which can further modify the structure and properties of the polymer. Secondary reactions are not considered in the model.

2.4.3. Frameworks of polymer growth models

There are several frameworks that can be used to model polymers, each with its own strengths and limitations. Some of the main frameworks are described below.

MC methods are a type of statistical modeling technique that simulates the behavior of a system over time based on the generation of a random number of events. In polymer engineering, these methods are commonly used to simulate a vast array of polymer properties, including chain length, branching, monomer sequence, functionality, and crosslinking density [4,215–218]. One of the primary benefits of MC methods is their ability to provide information about the microstructure of polymers, which is not possible with other modeling techniques. It can be used to simulate monomer propagation or chain transfer events in polymerization reactions, primarily through the use of coarse-grained model assumptions that eliminate microscopic degrees of freedom and represent a polymer through a simplified structure [219,220]. MC simulations are ideally suited for simulating radical polymerization in which the polymerization is triggered by the introduction of free radicals into the system [221,222]. This strategy divides the radical-based polymerization process into three stages: radical nucleation, chain growth within a solvent of monomers, and chain termination. To simulate the radiation-induced polymerization, however, a multi-scale modeling approach is required: first, the simulation of radiation transport to the media must be performed, followed by the MC simulation of radical-like polymerization.

Kinetic MC (KMC) models simulate the polymerization process at the molecular level, taking into account the rates of different reaction steps and the availability of reactants [223–225]. KMC models simulate the growth of polymer chains by considering the rates of different reaction steps and the availability of reactants. This method can simulate the evolution of the system over time by considering the rates of different reaction steps and the availability of reactants and detailed insights into the mechanisms and kinetics of a process. However, they are computationally intense and usually limited in scale and time. KMC models are limited in their predictive power, as they do not account for all possible interactions and are based on approximate probability calculations.

Method of Moment (MOM) models are based on the statistical properties of a system [226]. It is a method of approximating the solution to a problem by expressing it as a series of orthogonal functions and determining the coefficients of these functions through the use of moments. In particular, it has been used to study the size and shape distribution of polymer molecules and to predict the properties of polymer systems based on their microstructure. The drawback of this method is that it disregards the information about each individual chain and can therefore predict only average polymer properties.

Statistical mechanics models describe the thermodynamics of polymer systems and can be used to predict the equilibrium properties of polymer systems, such as the distribution of energy among the particles and the effect of temperature, pressure, and other variables on the properties of the system [227,228]. This means that models are limited in the time scales they can study, as they do not account for dynamic processes.

Molecular dynamics (MD) simulations use computational methods to model the motion of individual atoms or molecules in a system. MD simulations can be used to study the structure and properties of polymers at the atomic or molecular level, including their mechanical behavior and response to external stimuli [229–231]. To perform an MD simulation of polymer growth, a computer program is used to simulate the movement and interactions of individual atoms or molecules within a polymer chain. The application uses the input of acting potentials to compute the forces acting on each atom or molecule and to anticipate how they will move and interact over time. Various elements of polymer growth, such as the pace and mechanism of polymerization, the effect of temperature and solvent conditions on the polymerization process, and the effect of impurities or catalysts on the polymer structure, can be investigated using MD simulations. They can also be used to predict the properties of the resulting polymer, such as its molecular weight, size, shape, and physical characteristics.

Coarse-grained (CG) model simulation simplifies the representation of polymer molecules by grouping atoms or molecules into larger "coarse-grained" units [232,233]. Coarse-grained models can be used to study the properties of polymers, including the synthesis and growth of polymers, such as hydrogels at a larger length scale and can be computationally efficient compared to more detailed models. The interactions between the beads or particles can be described using various potential functions, such as Lennard-Jones potentials [234] or harmonic potentials [235], which can be modified to mimic the desired properties of the polymer.

Continuum models describe the behavior of polymers as continuous, homogeneous materials and can be used to study the macroscopic properties of polymers such as their mechanical behavior and rheology [236]. Continuum models represent polymers as continuous, rather than discrete, entities, and they describe the behavior of the polymer using macroscopic, rather than microscopic, variables. This allows for faster and more efficient simulations, as fewer variables need to be tracked and the interactions between them can be simplified. There are several types of continuum models that can be used for polymer growth modeling and simulation, including kinetic models, thermodynamic models, and mechanistic models. Kinetic models describe the polymerization process in terms of reaction rates and equilibria, while thermodynamic models describe the polymerization process in terms of free energy and entropy. Mechanistic models describe the polymerization process in terms of the mechanisms and pathways involved. Continuum models are often used in engineering applications to design and optimize polymer-based systems.

In this research, we present the coarse-grained (CG) based MC approach of radiation induced polymerization of methacrylic acid (MAA) in aqueous solution, where CG bead is equal to a whole monomer, and external radiation is introduced to

form the random radicals. The focus of this research is to analyze the micro-structure and the growth pattern of the of the radiation-induced polymerization of MAA in the aqueous solution, which would allow to optimize the synthesis of poly(methacrylic acid) hydrogels with unique properties [237,238].

3. INSTRUMENTS AND METHODS

3.1. Radiochromic films and their dose read-out

Radiochromic films (RCFs) are radiation-sensitive dosimeters that undergo a color change upon exposure to radiation. These films consist of a polymer matrix with a radiation-sensitive monomer embedded within and sandwiched between polyester layers. The radiation-induced polymerization of diacetylene molecules leads to the formation of polydiacetylene dye polymers, resulting in the colorization of RCFs. The dose-response characteristics of a particular RCF can be influenced by various factors, such as the film model, lot number, chemical composition, layer configuration, and absorption spectra [239]. Additionally, the radiation properties, including particle type (photon, electron, and proton) and energy (MeV, keV), can play a significant role. Other factors that can affect the performance of RCFs include the type of light source and its sensitivity to specific wavelength ranges, film orientation during scanning, scanning color depth, transmission or reflection scanning type, temperature of the scanner glass, and position of the film on the scanner. The time elapsed between irradiation and readout may also have an effect.

The experiments utilized radiochromic EBT3 and RTQA2 films, which are commonly employed as dosimeters for various quality assurance (QA) purposes in radiotherapy. Radiochromic EBT3 films are widely utilized for QA checks in radiotherapy and are particularly suited for this purpose. On the other hand, radiochromic RTQA2 films are specifically designed for machine QA in processor-less environments found in modern hospitals, primarily for LINAC/accelerator machine QA. Nonetheless, these films can also be effectively employed for quality assurance assessments in X-ray therapy within the kilovoltage range.

The primary distinction between these films lies in the composition of their different layers, while the active layer possesses the same elemental composition. In practical terms, the distinction manifests in their reading methods. The EBT3 film is ideally suited for accurate scanning through transmission measurements. In contrast, the RTQA2 film possesses an opaque backing material, which allows for more precise data acquisition through reflective absorption spectrum measurements.

According to the data provided by Palmer et al. [240] and Butson et al. [241], the films were modeled using MC geometry using a layered film construction of both types of films, and the elemental compositions used in the MC simulations are listed in **Table 1**.

Table 1. Chemical composition of radiochromic film

Layer type	Density (g/cm^3)	Composition by element, atom %								
		H	Li	C	N	O	Na	Al	S	Cl
Active layer	1.20	56.5	0.6	27.4	0.3	13.3	0.1	1.6	0.1	0.1
Adhesive layer	1.27	50.0	-	33.0	-	17.0	-	-	-	-
Base Layer	1.35	36.4	-	45.5	-	18.2	-	-	-	-

A series of experiments were conducted to calibrate both RTQA2 and EBT3 films according to the hospital's quality assurance (QA) protocol for absolute dose measurements, which was developed based on the guidelines outlined in the IAEA TRS-938 protocol. To minimize uncertainty, films from the same lot and type were used in all experiments. Prior to irradiation, each set of radiochomic films was calibrated under the same conditions that were later replicated during the experimental irradiation. The films were cut into 1.5x1.5 cm^2 pieces, with clear markings to indicate their orientation.

The irradiation process involved exposing the films to doses up to 4.0 Gy using the X-ray therapy unit GULMAY D3225. To ensure independent dose traceability, a plane-parallel ionization chamber (PTW TW23342) was centrally positioned on a PMMA phantom (PTW T2962), with two film pieces from the same batch placed on both sides of the chamber, directly on the phantom surface. Before commencing the irradiation, the dose correction factor k0=1.022 for the ionization chamber was determined using atmospheric conditions measured with a thermometer-barometer device (HD 2114B.0). The dose was measured using a PTW UNIDOS web line T10002 electrometer. The differences between the absorbed dose values indicated on the X-ray therapy unit console and those measured by the ionization chamber ranged from 1.5% to 2.0%. Consequently, dose correction factors were applied to each film piece based on the ionization chamber dose values. The irradiated film pieces were allowed to settle for 48 hours before being scanned using an HP Office Jet Pro 8600 scanner. A 600-dpi color scan without color correction or compression was performed. Consistency was maintained in the physical orientation of the film samples to minimize scanning artifacts, and opaque frames were utilized to reduce light scattering effects. Multiple readings (at least 5) of the same irradiated sample were taken, and the averaged pixel information was used to calculate the dose. The resulting scanned files were saved in uncompressed TIFF format, which ensured quality and clarity during subsequent edits and saves. The red channel was utilized for film scan evaluation. To mitigate scanner limitations, the films were also scanned using an Epson v370 scanner. However, the differences in image parameters between the two scanners were minimal, ranging from 1% to 3%, and did not yield significant variations in the scanned film images.

A calibration set of film scans was utilized to establish dose-response curves, which were then employed to evaluate the dose of the irradiated films within the experiments.

3.2. Materials used for the clinical setups

Besides the radiochromic films, various phantoms have been created for in vitro dose measurement and simulation purposes: an experimental PMMA slab phantom and a personalized 3D printed anthropomorphic phantom, which was reconstructed from CT scans of an anonymized patient.

A PMMA slab phantom, mimicking tissue equivalence, was engineered to simulate the irradiation environment for treating skin cancer in the buccal region. This phantom extended over an 8 cm section of the head and neck corresponding to the C1

to C8 vertebral levels and consisted of four individual slabs, with each slab measuring 2 cm in thickness. The contour and collective architecture of the phantom were derived from CT scans of an anonymized individual.

An anthropomorphic phantom tailored to the head and neck region of a specific patient was created using a series of CT scans from an actual individual. The phantom was fabricated using Acrylonitrile Butadiene Styrene (ABS) plastic through a 3D printing process and was filled with water before irradiation. Additionally, a metal artefact has been used to imitate a tooth implant. It was roughly the size and shape of a typical dental implant and was made from titanium.

3.3. Gamma index

Harms et al. [242] introduced a software tool designed to quantitatively assess the alignment and discrepancy of dose distributions obtained using different dosimetry methods. This evaluation relies on the simultaneous utilization of two parameters: distance-to-agreement (DTA) and percent dose difference (DD). DTA is defined as the minimum distance between a reference dose point and the corresponding dose point on the compared distribution. It provides an indication of the alignment quality between the two distributions. On the other hand, DD represents the percentage difference in dose assuming perfect alignment of the two distributions. Setting acceptance criteria for DD and DTA allows for a general assessment of the overlap between the two compared dose distributions. Low et al. [243] presented the gamma evaluation method (gamma index analysis), which allowed the collapse of two variables, DD and DTA, into one parameter. Both parameters were evaluated simultaneously by dividing them by specific common criteria. The gamma (index) is defined as the square root of a linear quadratic addition of the two discussed parameters, while they are given in relative magnitude to their acceptance criteria, as shown in equation (17):

$$\Gamma(\overrightarrow{r_e}, \overrightarrow{r_r}) = \sqrt{\frac{|\overrightarrow{r_e} - \overrightarrow{r_r}|^2}{\Delta d^2} + \frac{[D_e(\overrightarrow{r_e}) - D_r(\overrightarrow{r_r})]^2}{\Delta D^2}} \quad (20$$

where $\overrightarrow{r_e}$ and $\overrightarrow{r_r}$ are the vector positions of the evaluated and reference points, respectively; $D_e(\overrightarrow{r_e})$ and $D_r(\overrightarrow{r_r})$ are the calculated and reference doses, respectively; Δd and ΔD are the DTA and DD criteria, respectively. The generalized Γ function can be computed for any pair $\overrightarrow{r_e}$ and $\overrightarrow{r_r}$. Therefore, for each reference point, there are as many values of Γ as there are evaluated points. The minimum value of Γ is the value of γ:

$$\gamma(\overrightarrow{r_r}) = min\{\Gamma(\overrightarrow{r_e}, \overrightarrow{r_r})\} \forall \{\overrightarrow{r_e}\} \quad (21$$

The gamma (Γ) function serves as a comprehensive measure that combines both distance and dose information between two dose distributions. By incorporating both the dose difference (DD) and distance-to-agreement (DTA) criteria, the Gamma function offers a balanced approach to comparing the distributions. It eliminates the need to separately analyze DD and DTA, enabling a holistic assessment of the

comparison results. However, when interpreting these results, it is essential to consider additional analysis techniques.

In conjunction with gamma analysis, the superposition of dose profiles along specific lines passing through regions exhibiting high gamma values can provide further insights. This approach allows for a more detailed examination of the dose distributions, particularly in areas of concern. By complementing gamma analysis with dose profile superposition, a comprehensive set of tools for dose comparison can be employed.

Within the domain of megavoltage radiation therapy, the gamma index evaluation has gained widespread acceptance as the preferred method for comparing dose distributions in patient-specific pretreatment quality assurance. Its utilization ensures a standardized and reliable approach to assess the agreement between planned and delivered doses. By employing the gamma index and incorporating additional analysis techniques, clinicians and researchers can obtain a comprehensive understanding of dose distribution discrepancies and make informed decisions regarding treatment plans [243–248].

In-house created software tool based on the gamma-index were developed for the needs of the work of this thesis and is presented in the Result section.

3.4. MC radiation transport package FLUKA

The FLUKA (FLUktuierende KAskade) MC code is a comprehensive particle physics simulation package that encompasses a wide range of applications, including radiation and medical physics [249,250].

FLUKA is capable of accurately simulating the interaction and propagation of approximately 60 different particles, such as photons and electrons, spanning from 1 keV to thousands of TeV. It can also handle neutrinos, muons of any energy, hadrons up to energies of 10 PeV, their corresponding antiparticles, neutrons down to thermal energies, and heavy ions. Furthermore, FLUKA can transport polarized photons (e.g., synchrotron radiation) and optical photons. Although FLUKA offers extensive capabilities, for the purpose of our analysis focused on photon-electron transport, we will primarily emphasize the mechanics of simulating these particles in the code. The specific information provided below is gathered from FLUKA manual [251].

FLUKA can manage very complex geometries with advanced Combinatorial Geometry (CG) package. It includes support for voxel geometries. The current random number generator used in FLUKA is RM64, based on an algorithm by Marsaglia and Tsang [252]. FLUKA employs a proprietary transport algorithm for charged particles, which includes a comprehensive treatment of multiple Coulomb scattering. This ensures accurate lateral displacement, even in proximity to boundaries. The code considers the precise energy-dependent variations of discrete event cross sections and continuous energy loss during each transport step. It considers the distinctions between positrons and electrons, accounting for differences in stopping power and bremsstrahlung. It incorporates positron annihilation both in flight and at rest. Additionally, delta-ray production via Bhabha and Moller scattering is implemented in the simulation. In FLUKA, the transport of charged particles is

implemented using condensed history tracking, but there is an option for single scattering. The minimum transport threshold for photons is set to 1 keV, with a recommended minimum energy for primary photons ranging from 5 to 10 keV. For electrons, the minimal transport threshold is also 1 keV, with a recommended minimum energy for primary electrons ranging from 70 to 150 keV. It should be noted that in high-Z materials, the Molière multiple scattering model becomes less reliable below 20–30 keV. However, FLUKA offers a single-scattering option, which allows for satisfactory results in any material even in this low energy range.

FLUKA incorporates a variety of advanced simulation techniques for different interactions. Photon pair production is simulated using the actual angular distribution of electrons and positrons. The Compton effect includes Doppler broadening and utilizes a fit of the Compton profiles. Atomic bonds are taken into account through the use of inelastic Hartree-Fock form factors.

The photoelectric effect is generated using the actual photoelectron angular distribution based on the fully relativistic theory of Sauter. Interactions are sampled separately for each component element and for each edge, with consideration for edge fine structure. Parameterizations for photoelectric cross sections are included, covering all known edges up to Z=100 and down to a few eV. Optional emission of fluorescence photons is accounted for, along with an approximate treatment of Auger electrons for all K and most L lines. The simulation also considers the Rayleigh effect and photon polarization for Compton, Rayleigh, and Photoelectric effects. The source for pair production, photoelectric, and total coherent cross-section tabulations is derived from the EPDL97 photon data library.

It is worth noting that fluorescence emission may be underestimated for energies lower than the K-edge in high-Z materials due to the lack of the Coster-Kronig effect in the current implementation. The transport of charged particles in FLUKA offers several options, each with different considerations for delta ray production and ionization fluctuations. These options include:

- Continuous Slowing Down Approximation (CSDA): This approach neglects delta ray production and ionization fluctuations.
- With Ionization Fluctuations: This option accounts for ionization fluctuations but excludes delta ray production.
- With Delta Ray Production: Above a chosen energy threshold, delta ray production is included, but ionization fluctuations are not considered below the threshold.
- With Both Delta Rays and Ionization Fluctuations: This option includes delta ray production above the selected energy threshold and accounts for ionization fluctuations below the threshold.

FLUKA utilizes an original statistical approach to simulate these fluctuations, distinct from the Landau or Vavilov theories. The fluctuations can be requested separately for electrons and positrons, as well as for muons and charged hadrons.

The concept of multiple scattering is a useful approximation to capture the behavior of charged particles undergoing numerous single collisions with atomic electrons, which would be impractical to simulate in detail except for specific cases,

such as handling material boundaries and magnetic fields. However, FLUKA employs an original approach based on Moliere's theory, which yields excellent results for all charged particles in various scenarios, including backscattering problems. This approach preserves angular and spatial correlations and relieves the user from the need to explicitly control the particle step length. Another significant aspect of FLUKA is its capability to incorporate single scattering. This feature can be selectively enabled at boundary crossings when the limits of Moliere's theory are not met. It can also be activated for the entire simulation duration, although this option should be used judiciously, particularly for low-energy problems, due to its high computational demands.

The main assumptions and limitations of the code:

- Materials are static, homogeneous, and isotropic.
- Material properties remain constant through the simulation.
- Radiation transport is considered as a Markovian process: the particle depends only on its actual state, and not on its history.

Code structure

In general, for any simulation the following data must be initialized:

- Mandatory simulation parameters on how the calculation shall be performed;
- The geometry;
- The radiation sources;
- The materials;
- The requested results.

FLUKA reads user input from an ASCII "standard input" file which contains a variable number of settings ("options"), each consisting of one or more lines ("cards").

A typical FLUKA input file follows a structured format, including the following components:

- Titles and Comments: Provides a place for documentation purposes, where titles and comments can be added to describe the simulation setup.
- Geometry: FLUKA utilizes constructive solid geometry (CSG) to define geometry. It allows the creation of complex surfaces or objects by combining simpler objects using Boolean operators.
- Material Definitions: In this section, the materials used in the simulation are defined, including their composition and properties.
- Material Assignments: Here, materials are assigned to specific regions or volumes in the geometry.
- Detectors: Detectors define specific regions in space, along with particle direction and energy, where physical quantities like fluence are calculated.
- Biasing: Biasing techniques can be implemented in this section to modify the sampling of particles, allowing for more efficient simulations in certain regions of interest.

- Additional settings: Includes settings such as energy cut-offs, step size, specification of physical effects not simulated by default, particles to exclude from transport, and other specific requirements.
- Special commands: Enable the inclusion of features like magnetic fields, time-dependent calculations, writing history files, transport of optical photons, event-by-event scoring, user-written routines, and more.
- Initialization: A random number sequence is initialized to ensure reproducibility and provide an estimation of statistical error.
- Starting Signal and Number of Histories: Specifies the starting signal for the simulation and the number of requested histories (i.e., the number of particle tracks to simulate).

This typical structure of a FLUKA input file allows users to define the simulation setup, specify the desired calculations, and customize various aspects of the simulation.

As an example, we will start with DEFAULTS card, which must be issued at the very beginning of input.

```
*...+....1....+....2....+....3....+....4....+....5....+....6....+....7....+....8
DEFAULTS                                          PRECISIO
```

Every card has a name, in this case DEFAULTS, the six possible numerical parameters and the last character parameter. Depending on the cards, the various settings can be chosen. In the case above, we set DEFAULTS to PRECISIO parameter, which automatically select the specific calculation parameters. In this case, it activates the transport of electrons, positrons, and photons, including detailed photoelectric edge treatment and fluorescence photons activated. It also activates Rayleigh scattering, inelastic form factor corrections to Compton scattering, and activation of Compton profiles. These features are crucial for achieving high precision in the simulation of heavy particles. By incorporating these parameters, FLUKA ensures that the simulation accurately represents the behavior of particles in various scattering processes, allowing for more precise and realistic results.

The other two mandatory cards are START and STOP. The START command initiates execution. It defines the termination conditions, gets a primary from a beam or from a source and starts the transport.

In the figure below the provided command requests a run of 10,000 primary particles.

```
*...+....1....+....2....+....3....+....4....+....5....+....6....+....7....+....8
START     10000.
```

The STOP command stops the execution of the program and normally is placed at the end of the code.

```
*...+....1....+....2....+....3....+....4....+....5....+....6....+....7....+....8
STOP
```

In FLUKA, the simplest form of particle source is a “particle beam” characterized by being point-like, monoenergetic, and monodirectional. The option “BEAM” is used to define the particle type and momentum (or energy). Additionally, this option can be used to specify an energy spread, beam profile shape, and angular divergence, if desired. The energy declared with the “BEAM” command is utilized by the program to initialize cross-section tables and other energy-dependent arrays. Therefore, this command must always be included, even when a more complex source is described using a user routine.

The starting point and direction of the particles are defined using the “BEAMPOS” option. If the “BEAMPOS” option is not present, it is assumed that the beam particles originate from the coordinate origin (0., 0., 0.) and are directed along the z-axis. It is important to ensure that the starting point is not located on a boundary and does not fall within a region defined as a blackhole. In many cases, initiating the particle beam in a vacuum region upstream of the actual target can be advantageous. Both the “BEAM” and “BEAMPOS” commands in FLUKA can be placed anywhere in the input file, as long as they are positioned before the “START” command. The specific placement within the input file does not affect their functionality. This flexibility allows users to define the particle source characteristics and starting position/direction at a convenient location within the input file while ensuring they are set before initiating the simulation with the “START” command. For example, the two cards below illustrate 200 keV pencil-like electron beam parallel to the x-axis starting at a point of coordinates: -0.1 cm at X axis, 5.0 cm at Y axis, 5.0 cm at Z axis.

```
*...+....1....+....2....+....3....+....4....+....5....+....6....+....7....+....8
 BEAM         -2.E-4       0.0       0.0       0.0       0.0      1.0 ELECTRON
```

```
*...+....1....+....2....+....3....+....4....+....5....+....6....+....7....+....8
 BEAMPOS        -0.1       5.0       5.0       1.0       0.0       0.0
```

In FLUKA, the geometry data must be provided in a specific order and format within a designated section delimited by the “GEOBEGIN” and “GEOEND” statements. This ensures that the geometry information is correctly interpreted by the program. The geometry definition should follow the prescribed structure within this section to accurately define the spatial arrangement of volumes, materials, and boundaries in the simulation. “GEOBEGIN” starts the geometry description, with “COMBINAT” allowing to use combinatorial geometry.

```
*...+....1....+....2....+....3....+....4....+....5....+....6....+....7....+....8
GEOBEGIN         0.       0.       0.       0.       0.       0.COMBINAT
```

When constructing a geometrical setup using combinatorial geometry laws in FLUKA, two fundamental concepts to consider are bodies and regions. Bodies in FLUKA refer to convex solid bodies, which are finite portions of space completely delimited by surfaces of either first or second degree. These bodies define the basic building blocks of the geometry. Regions, on the other hand, are combinations of bodies obtained through Boolean operations such as Union (combining multiple bodies), Subtraction (subtracting one body from another), and Intersection (overlapping regions). Each region can consist of two or more noncontiguous parts but must have a homogeneous material composition. It is important to ensure that each point in space belongs to one and only one region.

To ensure accurate ray tracing, all the regions must be contained within a surrounding "blackhole," which is an infinitely absorbing material. This outermost boundary helps confine the geometry and ensures that the ray tracing routines do not extend beyond it. Following these guidelines and principles allows for the proper construction of a geometrical setup using combinatorial geometry laws in FLUKA. First, we define the certain geometrical bodies we want to use in our model. Two cards below create two spheres, 001 and 002, both centered at point x=0, y=0, z=0, with a radius of 001 equal to 1,000 cm and radius of 002 equal to 100 cm:

```
*...+....1....+....2....+....3....+....4....+....5....+....6....+....7....+....8
  SPH  001       0.0     0.0     0.0     1000.0
```

```
*...+....1....+....2....+....3....+....4....+....5....+....6....+....7....+....8
  SPH  002       0.0     0.0     0.0     100.0
```

This card creates a circular cylinder 10 cm long and of 5 cm radius, with base centered at point x=0, y=0, z=0, its axis making equal angles to the coordinate axes:

```
*...+....1....+....2....+....3....+....4....+....5....+....6....+....7....+....8
RCC   003       0.0     0.0         0.0   0.0   0.0    10.    5.
```

Having three bodies, we may start to define the regions according to combinatorial geometry rules and finish the geometry setup with a "GEOEND" card.

```
*...+....1....+....2....+....3....+....4....+....5....+....6....+....7....+....8
  BLKBODY      +001  -002
```

```
*...+....1....+....2....+....3....+....4....+....5....+....6....+....7....+....8
  VOID      +002  -003
```

```
*...+....1....+....2....+....3....+....4....+....5....+....6....+....7....+....8
  TARGET   +003
```

```
*...+....1....+....2....+....3....+....4....+....5....+....6....+....7....+....8
GEOEND        0.      0.      0.      0.      0.      0.
```

In the given scenario, three regions have been defined: BLKBODY, VOID, and TARGET. The BLKBODY region contains solid sphere 001 minus the solid sphere 002. VOID region contains the solid sphere 002 minus the solid cylinder 003. The TARGET region consists of the solid cylinder 003. Each of these geometry regions should be filled with a homogeneous material, vacuum, or a "blackhole" material. The "blackhole" material is a fictitious material that terminates particle trajectories upon reaching its boundary.

In FLUKA, materials can be simple elements or compounds. An element is defined using a MATERIAL card, which specifies the atomic number, atomic weight, density, name, and a material identification number. A compound, on the other hand, is defined using a MATERIAL card along with one or more COMPOUND cards to describe its composition. The MATERIAL card for a compound includes the compound name and density. It is necessary to associate a specific material with each of the defined geometry regions to accurately describe the material composition within the simulation.

```
*...+....1....+....2....+....3....+....4....+....5....+....6....+....7....+....8
  ASSIGNMA    BLCKHOLE    BLKBODY
```

```
*...+....1....+....2....+....3....+....4....+....5....+....6....+....7....+....8
  ASSIGNMA     VACUUM     VOID
```

```
*...+....1....+....2....+....3....+....4....+....5....+....6....+....7....+....8
  ASSIGNMA      COPPER    TARGET
```

In FLUKA, production thresholds for electrons, positrons, and photons, as well as the transportation threshold, can be set using the EMFCUT command. It is necessary to explicitly define these thresholds for all materials involved in the problem. For the specific case mentioned, where very low thresholds are desired, a common practice is to set a threshold of 5 keV for both the production and transportation of all photons, electrons, and positrons in all materials and regions.

By specifying these low thresholds, the simulation will consider interactions and transport of particles with energies above the defined threshold, while disregarding those below it. This allows for more detailed modeling of the interactions and behavior of particles within the chosen energy range, which can be advantageous in certain applications and scenarios.

```
*...+....1....+....2....+....3....+....4....+....5....+....6....+....7....+....8
 EMFCUT      -1E-5   1E-5      1.0  BLCKHOLE   @LASTMAST                PROD-
CUT
```

```
*...+....1....+....2....+....3....+....4....+....5....+....6....+....7....+....8
 EMFCUT      -1E-5   1E-5      1.0  BLCKBODY   @LASTREG
```

In the condensed history approximation, charged particle transport is performed in discrete steps. Each step represents a finite fraction of the particle's energy that is lost and deposited in the surrounding material. This approximation accounts for the cumulative effect of numerous small energy losses through elastic and inelastic collisions.

FLUKA utilizes a multiple scattering algorithm that ensures the results are robust and independent of the step size. However, in cases where specific accuracy is required or when magnetic fields are present, users have the option to override the default step length. This can be done using the EMFFIX card for electrons and positrons, which sets the step size corresponding to a fixed fraction of the particle's total energy in the material.

It is generally recommended not to exceed 5–10% of the total energy in dosimetry applications and in thin-slab geometries. Adhering to this guideline helps maintain accuracy and ensures reliable results in these scenarios:

```
*...+....1....+....2....+....3....+....4....+....5....+....6....+....7....+....8
 EMFFIX      COPPER   0.05     0.   0.   0.  0.
```

To obtain specific results in MC calculation, contributions to the "score" or "tally" of a detector need to be added up. In MC simulations, a detector serves as the equivalent of a measurement instrument. Different detector types, known as estimators, are designed to estimate various radiometric quantities. The final score represents a statistical estimation of the average value of the corresponding population.

Here are several commonly used detectors in FLUKA:

- USRBDX: This command defines a detector for the boundary-crossing estimator. It calculates fluence or current, either mono- or bi-directional, differential in energy and angle, on any boundary between two selected regions.
- USRTRACK: This estimator calculates volume-averaged fluence (differential in energy) for any type of particle or family of particles in a selected region. It provides information on the track length fluence.
- USRCOLL: Similar to USRTRACK, this estimator also provides volume-averaged fluence (differential in energy) for particles or particle families in a selected region. It focuses on the collision estimator.
- USRBIN: This option enables the calculation of detailed space distributions of energy deposition or integrated fluence. The output from USRBIN can

be visualized using a suitable graphics package, often presented as color maps.

- USRYIELD: With this option, it is possible to calculate angular yields of particles exiting a specific surface around a fixed direction. The results are double-differential distributions, typically with respect to variables such as kinetic energy, momentum, polar angle, rapidity, Feynman-x, etc.

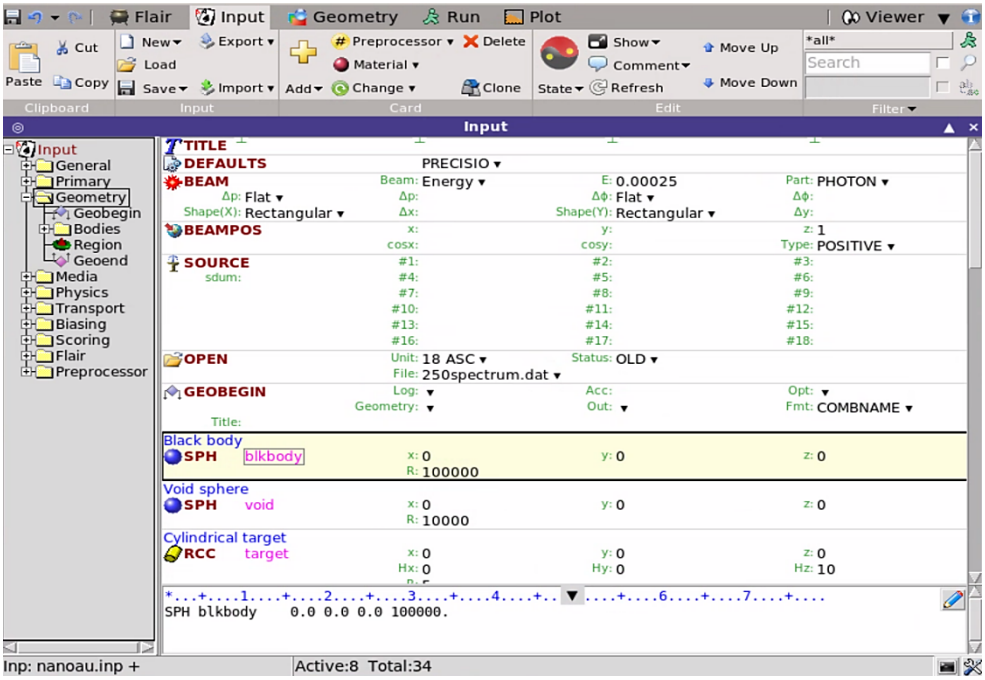

Fig. 4. FLAIR, GUI interface of FLUKA

In the given example, if the focus is on track-length fluence inside the target and an integrated fluence color map around the target, the USRTRACK and USRBIN cards would be utilized. These cards would be configured with specific parameters to capture the desired results.

```
*...+....1....+....2....+....3....+....4....+....5....+....6....+....7....+....8
USRTRACK      1.   PHOTON      -21.    TARGET    1.      1000.   Spectrum
USRTRACK     0.06    0.0001
```

It is important to note that the results obtained from the USRTRACK estimator will be provided as differential distributions of fluence in energy. The units for these distributions are given as cm-2 GeV-1 per incident primary unit weight. This means that the values represent the fluence per unit energy, normalized by the weight of the incident primary particles. To obtain integral binned results (fluence in cm^{-2}) the values of each energy bin must be multiplied by the width of the bin:

```
*...+....1....+....2....+....3....+....4....+....5....+....6....+....7....+....8
 USRBIN      10.   PHOTON      -22.    5.    5.     20.   Fluence
 USRBIN     -5.     -5.         -10.    100.  100.   150.
```

This USRBIN scores photon track length density in a regular spatial X-Y-Z structure independent from the geometry. Mesh is 100 bins between x = -5 and x = 5, y = -5 and y = 5, and 150 bins between z = -10 and 20.

The above-described cards are just a part of FLUKA code, yet they are the main cards used for the problems described in this work. FLUKA has an auxiliary program called Flair which is a user-friendly interface to aid the editing of FLUKA input files, execution of the code and visualization of the output files [253]. The main screen of GUI interface is shown in **Fig. 4**.

Generating polychromatic beam

Default options in FLUKA allow to generate only monochromatic beams of photon. However, the sources used in the medical physics field are polychromatic X-ray sources which cannot be recreated with default BEAM card.

One approach to solving this problem is to create a model of the X-ray machine itself and simulate the generated X-ray beam. By accurately modeling the X-ray machine, including its components and parameters, you can generate a realistic X-ray beam for further analysis. To achieve this, you would need to consider the geometry, energy spectrum, intensity, and other relevant characteristics of the X-ray machine. This information can be obtained from technical specifications or measurements of the specific X-ray machine being studied.

Using a simulation tool such as FLUKA, you can input the parameters of the X-ray machine and generate a simulated X-ray beam that closely resembles the actual beam produced by the machine. This simulated beam can then be used for various analyses and studies, such as evaluating its interactions with different materials or assessing its dose distribution in a specific target region.

By modeling the X-ray machine and utilizing the generated beam, you can gain insights into its behavior, optimize its performance, and assess its impact on various applications or scenarios. However, the accurate model of such machines can be especially complex, requiring accurate data for model geometry from the manufacturers and very demanding in simulation time. Hereby we are investigating the possibility to create a simplified model of orthovoltage and megavoltage machines and check them against experimental data. Such models could be very useful due to their simplicity and simulation speed while maintaining good accuracy with experimental data.

The FLUKA simulation package offers the capability to generate a beam by utilizing a customized routine that enables direct sampling from a given spectrum of a particular X-ray device. This feature allows for the accurate recreation of the beam characteristics specific to the chosen equipment. The package provides the flexibility to define particle sources with more complex features using a user-written subroutine called SOURCE.

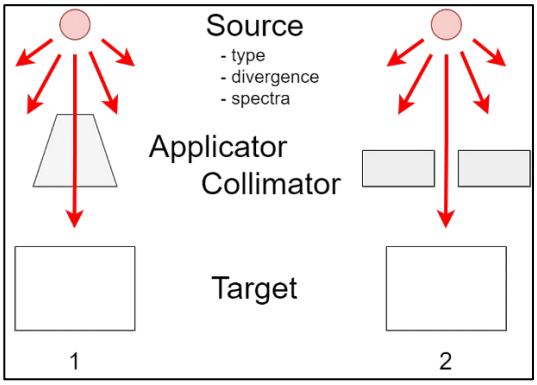

Fig. 5. Schematics of simplified orthovoltage (1) and megavoltage (2) machines for beam shaping in the simulation

This allows for arbitrary distributions in energy, space, angle, time, and even multiple particle types. To utilize the SOURCE subroutine, the SOURCE command must be included in the input file. To implement a custom particle source, a specific code must be compiled and integrated into the main FLUKA program. This code, often referred to as source.f, is typically written in the FORTRAN programming language. It contains the necessary logic and calculations to recreate the desired particle source behavior.

For example, if you want to recreate a circular beam with a specified divergence based on supplied spectrum data, you can modify the source.f routine accordingly. The spectrum data can be obtained from databases, research publications, or generated using dedicated software, especially in the case of orthovoltage beams.

Patient-specific dose estimations are currently a focal point, and it is hoped that MC simulations can enhance the existing method utilizing TG-43-style table-based source-superposition algorithms [19]. Incorporating the effect of interseed attenuation (ISA) and tissue heterogeneities for low-energy seed and applicator shielding and boundary scattering effects for higher-energy brachytherapy procedures would be possible if MC simulations were utilized effectively in clinical practice.

FLUKA is used often in the various researches that seek to improve the dose calculations in the brachytherapy [254–257] (**Fig. 6**).

By incorporating the modified source.f routine and appropriately configuring the SOURCE command in the FLUKA input file, you can accurately define the particle source with the desired characteristics, including energy, spatial distribution, angular distribution, and timing. This flexibility allows for the customization of particle sources in FLUKA, enabling the simulation of a wide range of realistic scenarios and experimental conditions. Generally, the model and simulation consist of these stages: beam recreation, beam exit, and target.

Beam recreation can be designed from the provided spectra. In this stage, the data of known spectra is supplied, and the simulation beam is created. The biggest challenge in this stage is the unknown factor of required beam divergence size. This

parameter should be derived through iterations of the simulations while checking against the experimental data.

Beam exit is modelled via simplified applicators in the case of orthovoltage machines and collimators to recreate the field size for megavoltage machines used for experiment. Lead can used as a material to create applicators and collimators (**Fig. 5**).

Brachytherapy simulations

Current clinical techniques calculate the brachytherapy dose by assuming the medium to be homogeneous water. Due to the generated oscillations in dosage absorption of genuine heterogeneous tissues with variable densities and compositions, such as bone, air in the oral cavity and sinuses, or artificial implants, the accuracy of dose rate and distribution may suffer. In extreme circumstances where the source is positioned or travels near medium with vastly varying densities, it may result in differing doses relative to the water phantom-based (standard) doses and a greater overall uncertainty than is recommended.

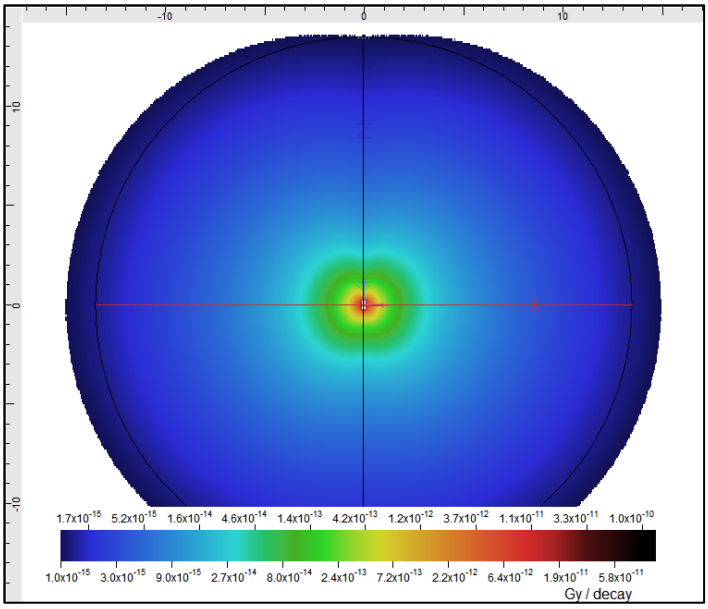

Fig. 6. Dose distribution in the water of standard brachytherapy source Ir-192

Simulations in voxel geometry. Human phantoms

When dealing with complex geometries like the human body, FLUKA offers the capability to represent them using a voxelized approach. Voxelization involves dividing the geometry into small, identical parallelepipeds called voxels, forming a three-dimensional grid.

In FLUKA, voxelized geometries are created using the Voxelized Geometries (VOXEL) package. This package allows the user to define the geometry of the target object or region by specifying the properties of each voxel in the grid, such as material

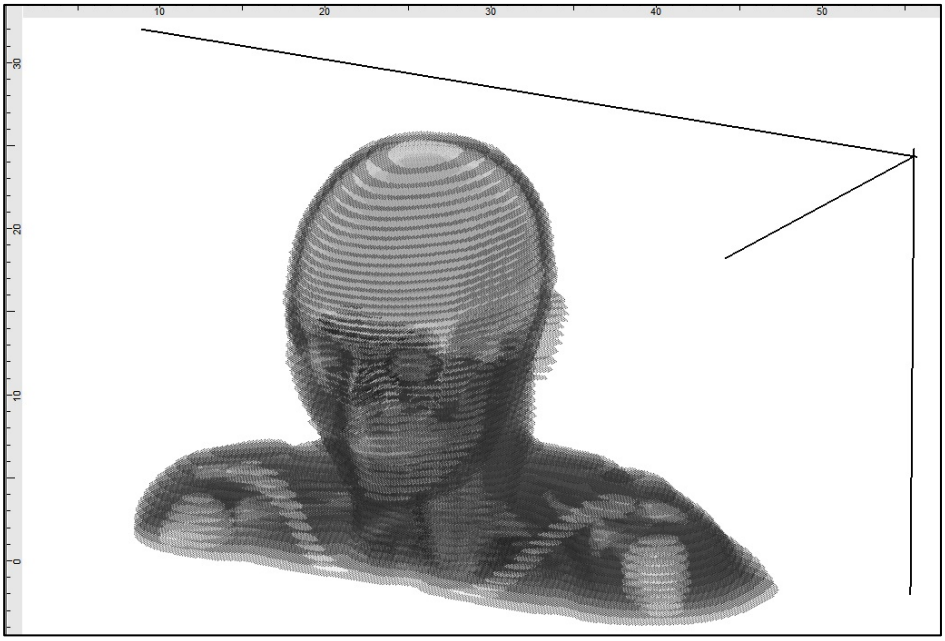

Fig. 7. The upper part of Adult Female Reference Computational Phantom [258] usable for the simulation converted to the voxels and viewed with SimpleGeo auxiliary software [B2]

composition, density, and other relevant parameters. These voxel properties can be assigned based on medical imaging data, such as computed tomography (CT) or magnetic resonance imaging (MRI) scans of the human body. Voxel phantoms can be used as virtual human representation for which absorbed dose to organs and tissues from exposure to ionizing radiation can be calculated. By representing complex geometries using voxels, FLUKA can accurately simulate the transport of particles through the intricate structure of the human body or other complex objects. This voxel-based approach provides a high level of detail and allows for realistic calculations of radiation interactions and dose deposition within different tissues and organs.

The upper part of The International Commission on Radiological Protection (ICRP) reference female adult phantoms, described in Publication 110 [258], has been used to model the voxel phantom suitable for dosimetry simulations. Phantoms are built on medical image data of actual persons and are consistent with the information given in ICRP Publication 89 on the reference anatomical and physiological parameters for a human body.

The construction of reference voxel models involved modifying the voxel models of two individuals who closely matched the reference data in terms of body height and mass. The goal was to create models that closely resemble the anatomy of the adult Reference Male and Reference Female as provided by the International Commission on Radiological Protection (ICRP). During the modification process, the organ masses of the voxel models were adjusted to align with the organ masses

specified in the ICRP data. This adjustment was made to ensure that the reference voxel models maintain a realistic anatomy while adhering to the organ mass values defined by the ICRP for the Reference Male and Reference Female. The resulting reference voxel models provide a reliable representation of the human body for various applications in radiation dosimetry, medical imaging, and radiation therapy planning.

As part of this work, the Female phantom data was converted to Fluka vxl format which serves as an input for the simulation of the radiation transport using the voxel geometry (**Fig. 7**). The SimpleGeo[259] auxiliary software also can be used to visualize it. The voxel regions were modeled with the anatomically equivalent media described in the ICRP 110 publication.

Such capabilities allow complex simulations to be carried out, with theoretical applications in clinical practice, e.g., in the case of complex head and neck cancers, where irradiation is required, but the patient's jawbone is reinforced with metal plates.

Uncertainties in the MC simulations

MC simulations can eliminate experimental uncertainties, such as caused by detector positioning and response artifacts, or any other related. However, the effects of geometric uncertainty, internal component movement, tolerances in source fabrication, and minor manufacturing changes on the uncertainty of calculated dose-rate distributions limit the accuracy of MC. The accuracy of MC simulations can be affected by factors such as inaccuracies in the geometric configuration of the source, uncertainties in cross-section data, and the modeling of physical processes within the MC code. Various factors, including physics models, transport assumptions, algorithms, input data accuracy, material composition, and geometrical uncertainties, among others, contribute to the type B systematic uncertainty in MC simulations of radiation transport. Additionally, errors can arise from code implementation or user mistakes, such as input errors or incorrect normalization.

On the other hand, type A uncertainties are estimated based on the standard deviations of repeated measurement results. In the case of the FLUKA code, statistical errors for batches of multiple histories are computed. The standard deviation of an estimator calculated from either batches or single histories provides an estimate of the standard deviation of the actual distribution, often referred to as the "error of the mean" or "statistical error."

Table 2. Estimation of relative error

Relative error	**Quality of tally**
50–100%	Garbage
20–50%	Factor of a few
10–20%	Questionable
<10%	Generally reliable
<5%	Reliable

It is suggested that at least 5–10 batches of comparable size should be run. The MCNP guideline [260] provides insight into estimating statistical error (**Table 2**), which has been confirmed to work with other codes. It should be noted, however, that it is based on empirical evidence rather than mathematical proof.

3.5. Programming language C++

C++ is a versatile and strong programming language that is ideal for scientific simulations, data analysis, and numerical computations [237]. It was created in 1983 as an extension of the C computer language by Bjarne Stroustrup. It is recognized for its low-level memory manipulation capabilities and its capacity to manage complex data structures and algorithms. C++ also offers object-oriented programming, which enables the encapsulation of data and functions within objects that can be reused.

It is widely utilized in a wide range of scientific and technical sectors, and it is a superb choice for developing complex mathematical models and modeling large-scale physical systems. C++ is used in physics to simulate the behavior of subatomic particles and their interactions, such as GEANT4, which is used in high energy physics and medical physics to simulate particle passage through matter. C++ is also used in astronomy to simulate the dynamics of galaxies and star evolution. The programming language is used to simulate materials and structures, such as fluid dynamics, heat transfer, and stress analysis. LAMMPS, for example, is a widely used code in materials science for simulating the behavior of solid and liquid materials under various situations. GROMACS and GROMOS, for example, are two codes used to simulate the behavior of proteins, nucleic acids, and other biomolecules under various situations.

C++ is well-suited for MC simulations in particular because it enables for the use of random number generators, which are required for producing random samples from a probability distribution [237]. It provides a built-in random number generator (RNG) called the “Mersenne Twister” (mt19937) that can be used to generate high-quality pseudorandom numbers. This RNG is suitable for many types of MC simulations, and it is also the base of other more complex generators like the “Mersenne Twister” with Improved Jump Functions (mt19937_64) and the “Mersenne Twister” with dynamic creator (mt19937_smith_32). C++ can also handle enormous volumes of data and execute sophisticated calculations, which are frequently required in MC simulations. The capability for object-oriented programming enables the development of clear and modular code, making it simple to add or update simulation features. Different sampling techniques, for example, can be implemented as classes and simply swapped out, or new models can be added by establishing new classes.

Furthermore, C++ includes a surplus of libraries and tools that can be utilized to increase the software capabilities. These libraries contain capability for dealing with big arrays, linear algebra, and parallel processing, which can be leveraged to improve simulation speed. Some of the libraries are tuned for parallel architectures like as MPI, OpenMP, and CUDA, allowing simulations to be executed on high-performance computing clusters. C++ is an excellent programming language for

scientific simulations, data analysis, and numerical computations, and it is especially well-suited for MC simulations. Its robust capabilities and extensive library and tool set make it an invaluable tool for scientists and engineers doing sophisticated simulations and modeling scientific challenges. C++17 is the most recent standard version of the language, which was officially released in 2017 and was used in this work to create the polymer-growth model used for MC simulations.

3.6. Computational resources

The MC simulation of complex geometries require a lot of computational power as a large number of the events should be run to achieve the reasonable relative error.

For this FLUKA simulation, the computational resources of Kaunas University of Technology computational resources have been used. The computational cluster site has been assigned for the needs. The cluster consists of 30 calculation cores. Each core has Intel Xeon Gold 6138 @ 2.00 GHz CPU and 64 GB RAM.

The developed polymer-growth code was run on Tetralith HPC provided by the Swedish National Infrastructure for Computing (SNIC). Tetralith is comprised of 1908 computing nodes running CentOS 7, each of which contains two Intel Xeon Gold 6130@ 2.10GHz processors with 96GiB of memory with 16 cores each, for a total of 61056 CPU cores. All servers are interconnected with a 100 Gbit/s Intel Omni-Path network which is also used to connect the existing storage. The overall performance of the system is approximately 3 Pflop/s and is included in the top 200 list of most powerful HPC in the world (2022 y.) [261].

4. RESULTS AND DISCUSSION

4.1. MC radiation transport simulations. Roadmap

The main aim for the successful simulation of radiation energy transport is to fine-tune our MC simulation to match the conditions of real experiments as closely as possible. This allows us to compare the results of the simulation with actual data. Given the complex and variable nature of the MC simulation package, it is essential to construct a setup that is tailored to address the specific problem under investigation.

Initially basic geometrical models are exposed to a monochromatic photon beam within the simulation. We then check how well our simulation results match the known reference data from the National Institute of Standards and Technology (NIST).

Subsequently, we transition to modeling a polychromatic photon beam that accurately mirrors the specifications of an orthovoltage X-ray machine. We then proceed to test this model by implementing a homogenous water cube as the experimental geometry and comparing the outcome to empirical measurements of Percentage Depth Dose in a comparable water cube for the actual machine.

Next, we incorporate radiochromic films into moderately complex geometries, such as high-density heterogeneous bodies, in order to replicate the properties of metal implants. The experimental setup and simulation are carefully matched, and the results analyzed with the use of a purpose-developed 2D gamma index measurement tool.

The final phase involves the creation of an intricate, clinically relevant setup employing a 3D-printed anthropomorphic human head model, radiochromic films, and a metal tool implant. The simulation aspect of this stage necessitates a voxel geometry that reproduces the International Commission on Radiological Protection (ICRP) human voxel phantom, with certain modifications, such as the approximation of a “metal tooth implant”. This setup lets us compare our simulation with the real experiment very closely and our results are similar to those achieved by other researchers.

In the first part of the results, the FLUKA simulations performed in the calibration and clinical setups will be presented, based on the works of Ševčik et al. [A1, A2].

4.2. FLUKA simulation: validation

The attenuation coefficient, indicative of a material’s capacity to absorb and scatter electromagnetic radiation, undergoes significant changes during the polymerization process, making it a crucial parameter to consider. For the preliminary validation setup, we plan to carry out a simulation where the polymer material is exposed to a monochromatic photon beam. The resulting data will then be cross-referenced with existing databases for validation. Following this, we will generate a polychromatic photon beam and present the subsequent attenuation results, offering a more accurate representation of real-world conditions. Orthovoltage X-ray spectra generated by SpekCalc was utilized as sampling distribution within the FLUKA simulation environment to replicate the same spectra.

In the simulation setup, a pencil beam representing the selected spectrum was directed through 10 layers of 1 cm-thick water medium in the positive direction along the Z-axis. The resulting polychromatic photon beam was generated using a pencil beam source with no divergence. In the simulation, the primary focus was on measuring the photon fluence of the primary beam and monitoring any changes in its intensity. To determine the mass attenuation coefficient, the total attenuation including coherent scattering was calculated. The basis for media was modeled identical to the composition of normoxic Methacrylic acid (**Table 3**).

Table 3. Composition by relative weight of modelled gels [B1]

Element	Materials, mass % of elemental composition		
	nMAG	nPAG	Water
	$\rho = 1.05$ g/cm^3	$\rho = 1.04$ g/cm^3	$\rho = 1.00$ g/cm^3
H	10.56	10.58	0.182
O	80.90	80.52	0.818
C	6.94	6.18	-
N	1.43	2.03	-
P	0.08	0.33	-
Cl	0.09	0.37	-

During the initial phase of the simulation, monochromatic beams were simulated, and the attenuation in a water medium was analyzed. The obtained results were then compared with reference values from the NIST database. The level of discrepancy between the simulation results and the reference values was found to be within 1%, suggesting that the selected model parameters were appropriate for accurately predicting the attenuation behavior in the water medium (**Table 4**).

Table 4. Comparison of derived mass attenuation coefficient with NIST reference values in water medium [B1]

Monochromatic Beam Energy, MeV	**Simulated μ/ρ. cm^2/g**	**NIST reference value**	**Percent error**
0.01	5.327E+00	5.329E+00	0.04%
0.02	8.063E-01	8.096E-01	0.41%
0.03	3.761E-01	3.756E-01	-0.13%
0.04	2.663E-01	2.683E-01	0.75%
0.05	2.292E-01	2.269E-01	-0.99%
0.06	2.058E-01	2.059E-01	0.05%
0.08	1.824E-01	1.837E-01	0.71%
0.10	1.716E-01	1.707E-01	-0.52%
0.20	1.369E-01	1.370E-01	0.11%
0.30	1.193E-01	1.186E-01	-0.62%
0.40	1.062E-01	1.061E-01	-0.10%
0.50	9.649E-02	9.687E-02	0.39%

The simulations with monochromatic beams were further extended to include gel media in the model. The obtained results were then compared with values obtained using the XCOM tool as a reference. Similar to the previous findings, the discrepancies between the simulated results and the reference values did not exceed 1%. This reinforces the validation of the selected simulation parameters and the suitability of the modelled media.

Following the successful validation with monochromatic beams, the simulations were then extended to include polychromatic beams. These simulations were conducted using the same modelling setup as before, allowing for a comprehensive analysis of the effects of polychromatic radiation in the simulated environment. The resulting mass attenuations coefficients are listed in the figures below as a function of penetration depth, starting with water medium (**Fig. 8**, **Fig. 9**, **Fig. 10**).

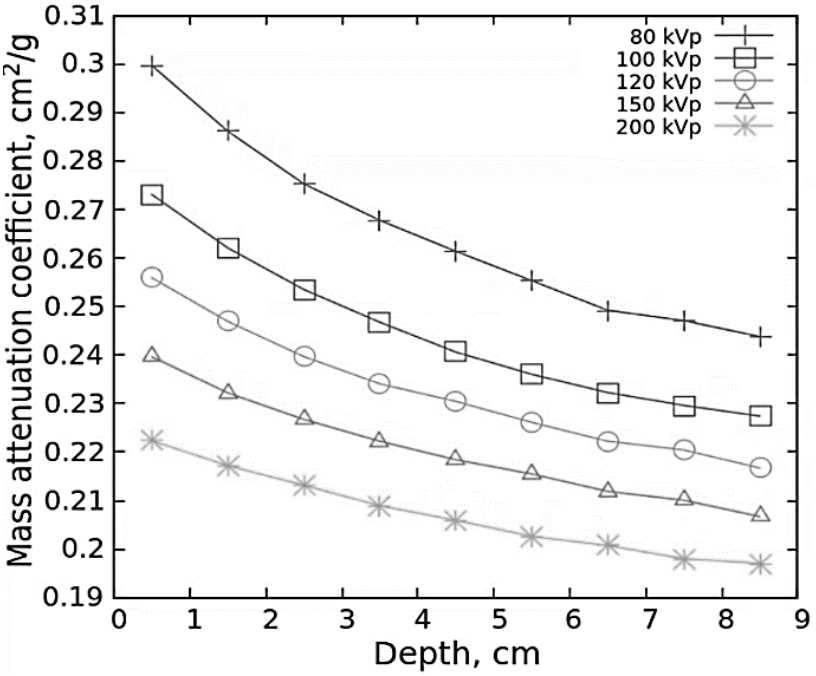

Fig. 8. Mass attenuation coefficient of water medium in the polychromatic orthovoltage photon field [B1]

The simplified orthovoltage machine simulation with a 3 cm annular applicator for 80 kVp, 100 kVp, 120 kVp was modeled and the percentage depth dose (PDD) curves was compared against experimentally obtained ones. In addition, 5 cm and 10 cm annular applicators were modeled for 80 kVp energy spectrum and the simulated PDD curves were compared against experimentally obtained ones.

To generate orthovoltage X-ray spectra replicating the GULMAY D3225 unit with a tungsten anode X-ray tube, the researchers utilized a computational toolkit called SpekCalc [262–264] (**Fig. 11**).

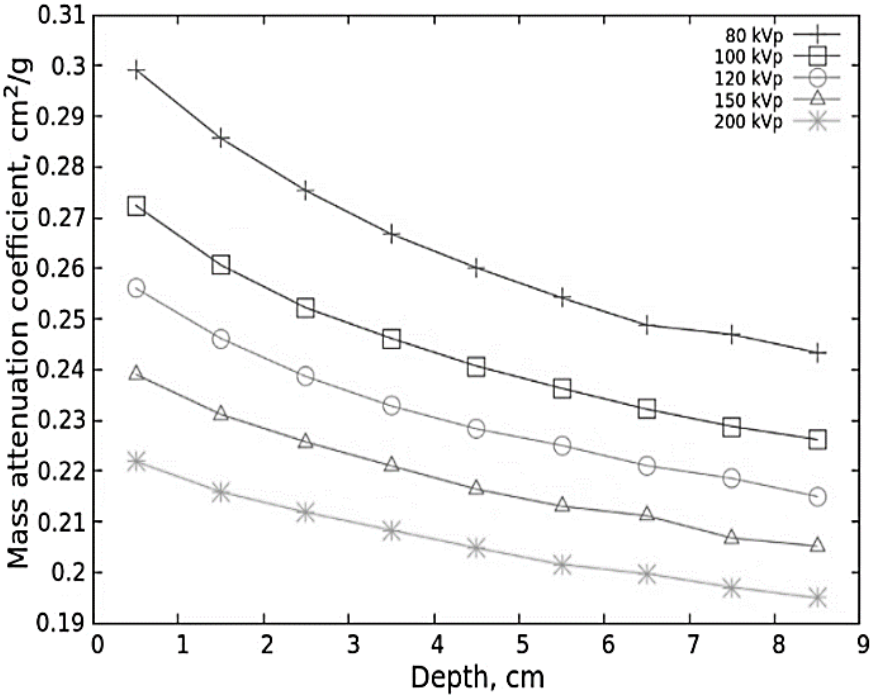

Fig. 9. Mass attenuation coefficient of nPAG medium in the polychromatic orthovoltage photon field [B1]

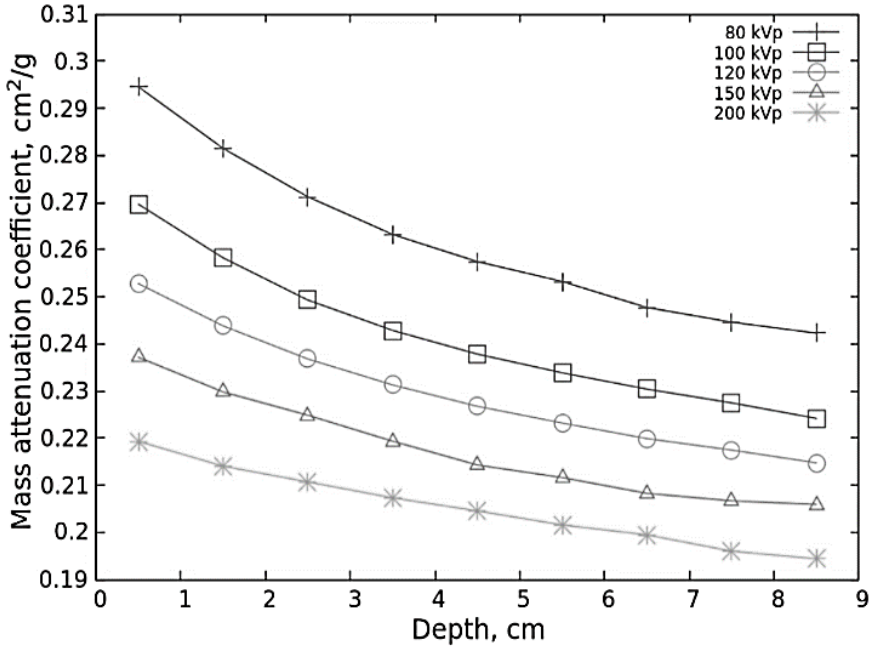

Fig. 10. Mass attenuation coefficient of nMAG polymer medium in the orthovoltage polychromatic photon field [B1]

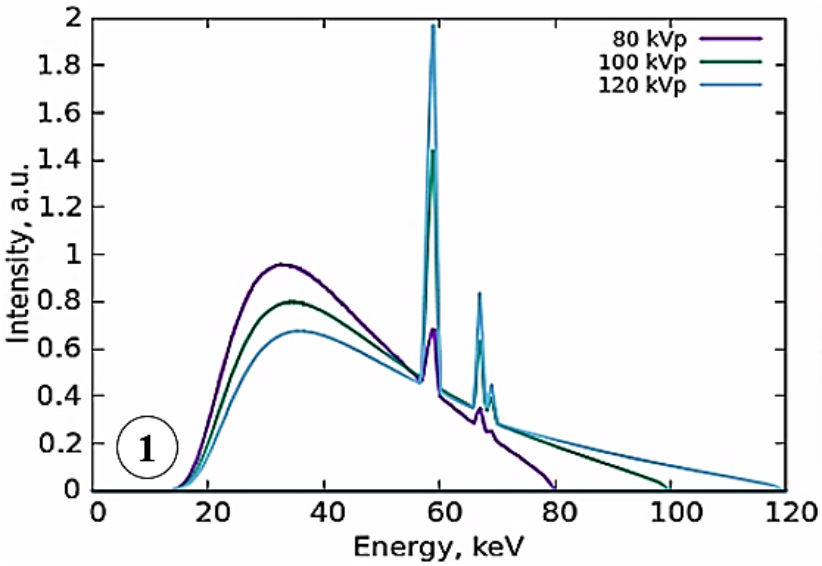

Fig. 11. The polychromatic spectra sampled in MC simulation for orthovoltage machine [B1]

To replicate the unit spectrum, the simulation considered several important parameters. The tungsten target was modeled at an angle of 20º relative to the beam axis, and additional filtration was incorporated to match the real system. This included an inherent beryllium filtration of 0.8 mm and an added filtration of 2.44 mm aluminum. By carefully reproducing these specifications and utilizing the SpekCalc toolkit, the researchers were able to generate orthovoltage X-ray spectra that closely resembled the X-ray emission characteristics of the GULMAY D3225 unit with a tungsten anode X-ray tube.

The modeled geometry was built with a 3 cm annular application for orthovoltage machine and the simplified lead collimator for megavoltage machine. The target for both simulations was a water cube in which the dose values were scored. The result data collected by USRBIN is matched against the experimental data. The results of the verification simulations are shown in **Fig. 12**. The data match is excellent and deviates less than 2% therefore it can be stated that the simulation environment was set up correctly and can be used for the actual simulations and replications of the experiments.

The following irradiation geometries mimicking the experimental setups in which radiochromic films are used were modelled for the initial test and validation purposes:

- The first geometry involved irradiation of a 60x60 mm film placed between two 2-cm thick PMMA slabs, with the X-ray beam directed in the transverse plane.
- In the second geometry, the film measuring 60x100 mm was subjected to side irradiation, positioned between two 2-cm thick PMMA slabs.

- For the third geometry, the film measuring 60x60 mm was placed on a PMMA slab, and an additional pure titanium cube measuring 1x1x1 cm was introduced. This specific arrangement aimed to simulate the irradiation pattern in scenarios where high-density objects are present within the irradiation field.

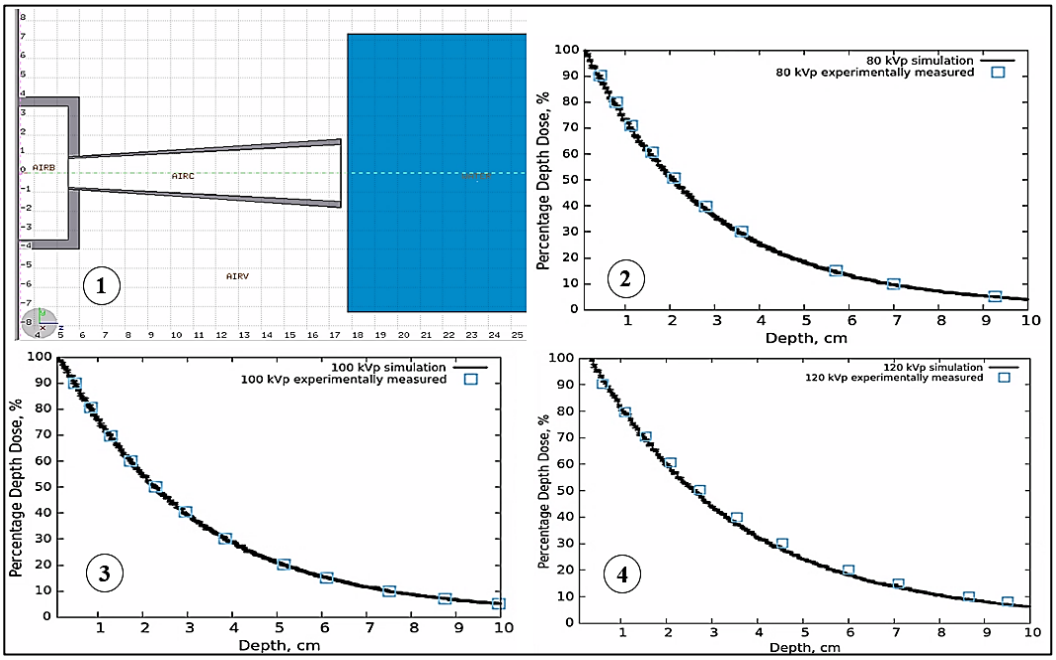

Fig. 12. Comparison of experimentally measured and simulated PDD in the water media polychromatic X-ray beam: 1 - Modelled geometry with 3 cm annular applicator; 2 - f or 80 kVp X-ray; 3 - for 100 kVp; 4 -for 120 kVp [B1]

Geometries were chosen to demonstrate various possible discrepancies. The FLUKA simulation package employed specified input files that outlined the irradiation geometry and parameters, including the characteristics of the radiation source, beam properties, and media specifications. The surrounding medium in the simulations was air. The irradiation setup consisted of a cone composed of pure lead, a slab of polymethyl methacrylate (PMMA), and an additional cube made of pure titanium (Ti). Notably, in the third geometry, a 2 cm thick water layer was substituted for the PMMA slab. The simulations took this into account. The chemical composition listed in **Table 1** was used to model the film material (**Fig. 13**).

The X-ray spectrum of the GULMAY D3225 unit using a peak voltage of 120 kVp and aluminum filtration of 2.44 mm was modeled using SpekCalc [262]. The default normalization factors of 0.68 and 0.33 were utilized for the output and characteristic radiation, respectively, relative to the bremsstrahlung component. The estimated effective energy of the X-ray beam was 53.5 keV, with the first half-value layer (HVL) being 3.74 mm Al. The polychromatic X-ray spectrum generated served

as the input data for subsequent MC simulations. Furthermore, the MC-simulated percentage depth dose (PDD) curve in water was experimentally verified through ionization chamber measurements, following the method described in section 3.4. The FLUKA simulation with the verification results is presented in **Fig. 14**. Only small (<2%) discrepancies were observed between the two curves.

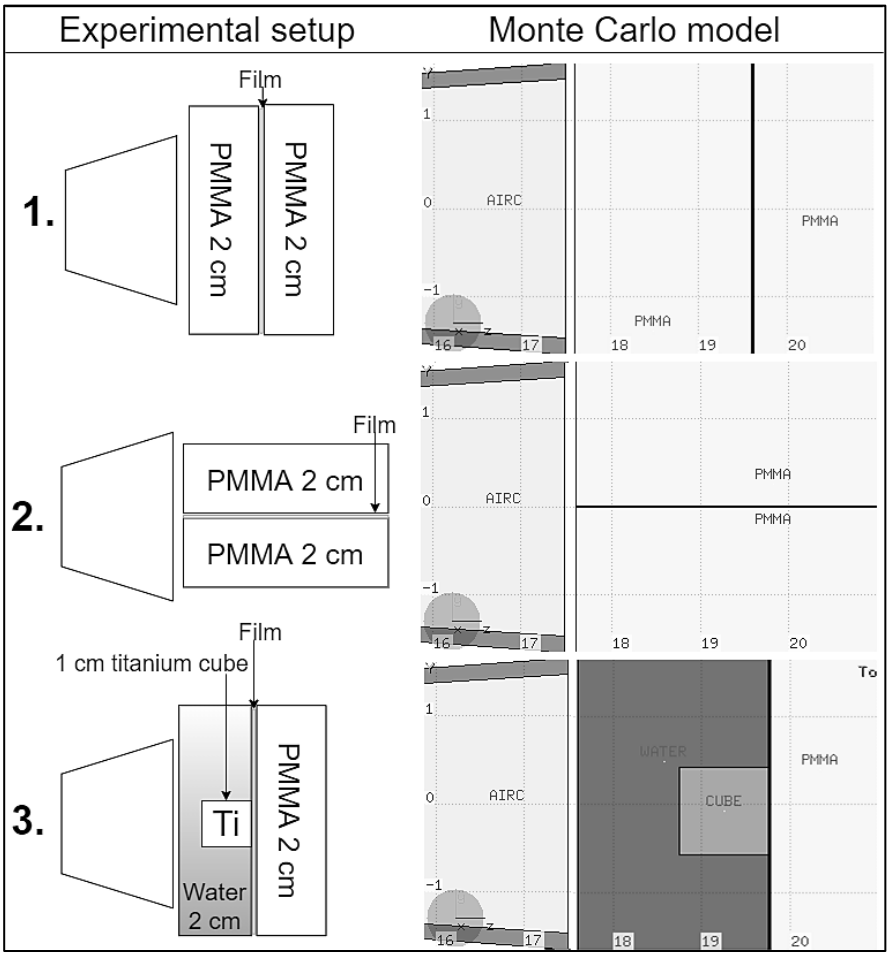

Fig. 13. Different irradiation geometries employed in the experiments: 1) the film was irradiated in the transverse plane; 2) the film was subjected to side irradiation; 3) the film was irradiated in the transverse plane with a titanium cube placed on top (note that the experimental geometries are not depicted to scale) [A2]

The successful validation of the simulation parameters provides a foundation for utilizing MC simulations to generate percentage depth dose (PDD) curves in subsequent experiments involving radiochromic films. The comparison between simulated dose maps and dose profiles for various irradiation configurations, namely, transverse plane, side, and transverse plane with a titanium cube, is presented in **Fig. 15** and **Fig. 16**. The dose profiles were obtained by averaging the dose values along

the middle line (-2 mm to 2 mm) between two 2 mm thick layers. The primary focus of the comparison was the percentage depth dose. Notably, significant discrepancies were observed between the experimentally determined and MC-simulated dose values in regions characterized by high dose distribution gradients, suggesting the influence of metal artifacts (such as the titanium cube) on the final dose distribution observed on the irradiated film.

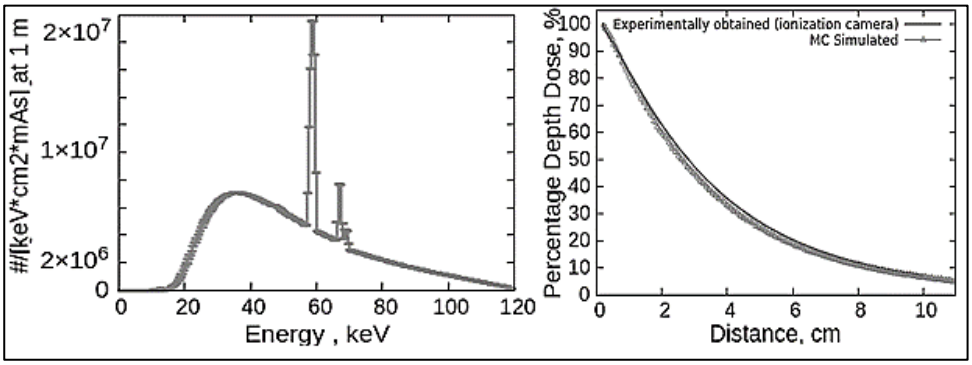

Fig. 14. PDD and energy spectrum parameters simulated using the GULMAY D3225 unit. On the left side, an energy spectrum was generated for a 120 kVp beam. On the right side, a comparison was made between the experimentally obtained PDD curve in water and the PDD curve simulated using MC methods [B1]

The investigation involved an assessment of the uncertainty budget to analyze the factors contributing to the lack of precision and accuracy in dose delivery using radiochromic films in keV therapy. The proposed gamma index evaluation software was utilized to quantify the extent of uncertainty. Type A uncertainty estimates were obtained by determining the standard deviations of repeated measurements, while the FLUKA code calculated the statistical error from batches of multiple histories. It was ensured that the combined statistical error for the MC simulations remained below 2% across all regions of interest.

In this work, type B uncertainty was present in both MC simulations and experimental investigations. Uncertainties in simulations include assumptions about transport processes, limitations of the algorithms used, uncertainty in input data, variations in the actual composition of materials, geometric uncertainties, and discrepancies in film positioning between the model and experimental setup. There is also experimental B-type uncertainty, which includes irradiation and calibration uncertainties, as well as the uncertainty in precisely measuring the dose-response characteristics of a specific radiochromic film.

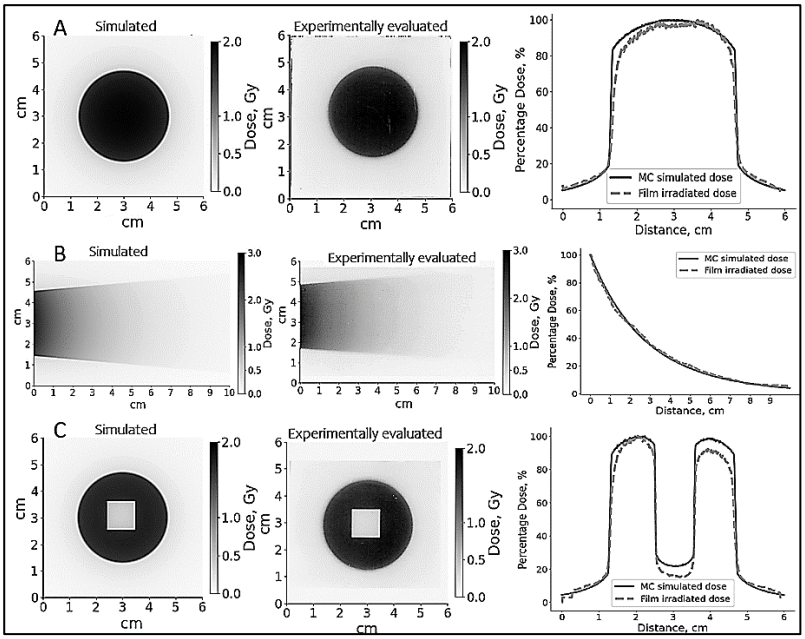

Fig. 15. Comparison of MC-simulated and irradiated dose maps and profiles for EBT3 radiochromic films: A – transverse plane irradiation, B –side irradiation, C – transverse plane irradiation, film with Ti cube on the top [A2]

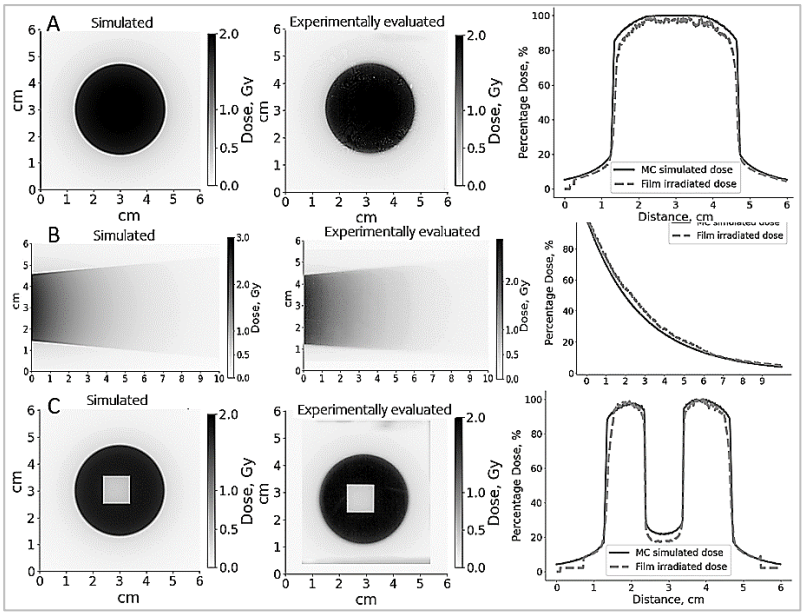

Fig. 16. Comparison of MC simulated and irradiated dose maps and profiles for RTQA2 radiochromic films: A – transverse plane irradiation, B – side irradiation, C – transverse plane irradiation, film with Ti cube on the top [A2]

The significant uncertainties of type B in this work were introduced by technical limitations of the scanners used, which did not meet all of the recommendations in AAPM Report TG-55 and its update [265] have highlighted substantial dose discrepancies and notable differences in the gamma index when comparing MC simulation data with radiochromic film evaluation, particularly in regions with high-dose gradients. This disparity becomes more pronounced in irradiation setups involving metal artifacts. The dissimilarity in geometries between the experimental and MC simulation setups is another significant source of uncertainty. Achieving positioning accuracy greater than 1 mm in the experimental setup, equivalent to the precision employed in the MC simulation, posed a considerable challenge.

Additionally, it is important to acknowledge that the radiochromic film pieces were not perfectly flat, introducing substantial uncertainty when comparing the dose distribution in the irradiated film with the MC results, specifically in certain geometries. Furthermore, it is crucial to recognize that the MC simulation solely captures the delivered dose to the media point and does not account for any radiation-induced chemical reactions occurring within the irradiated active layer of the radiochromic film, which may contribute to changes in the dose-response curve. These considerations emphasize the complexity and potential sources of uncertainty when comparing MC simulation data and radiochromic film evaluation, highlighting the need for cautious interpretation and further investigation.

All of these elements can have an impact on the accuracy and results of MC simulations. These factors have been thoroughly researched in the literature, resulting in uncertainties ranging from 3% to 8%. As a result, a conservative value of 8% was chosen for evaluating the uncertainty in this work.

4.3. FLUKA simulation: clinical setup

FLUKA was employed to assess the deposition patterns and dose distributions of low energy X-rays in a 3D printed anthropomorphic head and neck phantom that incorporated a metal artifact (a metal tooth in the lower jaw) (**Fig. 17).** It should be noted that the simulations encompassed comprehensive 3D data regarding the dose distribution. However, to facilitate a comparison with the dose distributions obtained from irradiated EBT2 films, the simulation results were presented as 2D images on transverse and vertical planes.

The presence of a metal artifact, specifically a metal tooth in the lower jaw, in the construction of an anthropomorphic phantom introduces more complex and intricate 2D dose distribution patterns compared to the standard case without any implants obstructing the dose pathway. This complexity arises due to the higher photon absorption in metal compared to biological tissue, leading to the generation of secondary electrons that contribute to the final dose pattern.

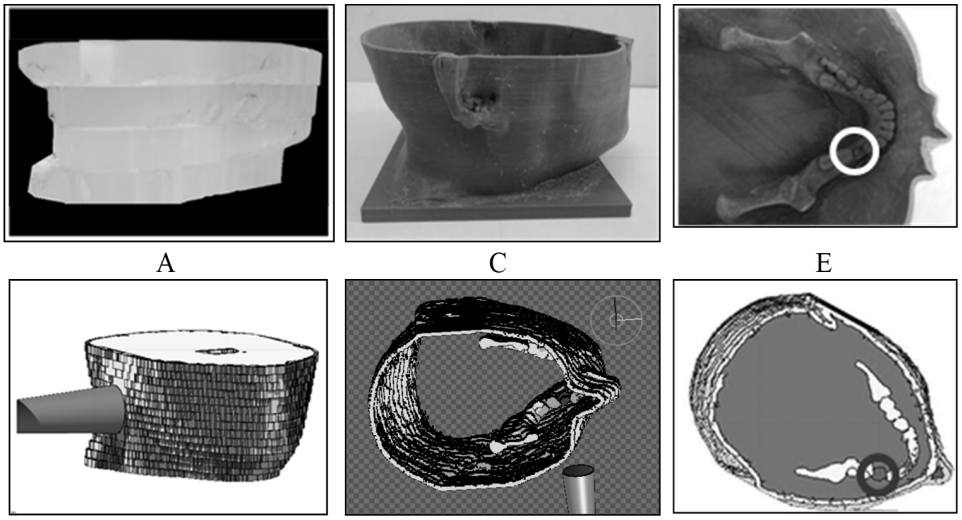

Fig. 17. Phantoms for dose distribution evaluation: A – PMMA slab phantom; B – simulated slab phantom; C – 3D printed anthropomorphic phantom rebuilt from CT images of actual patient; D – modeled anthropomorphic phantom model; E – transversal view of 3D printed phantom presenting location of the lower jaw with teeth and metal tooth inside; F – transversal view of the simulated water-filled phantom with metal tooth in it [A1]

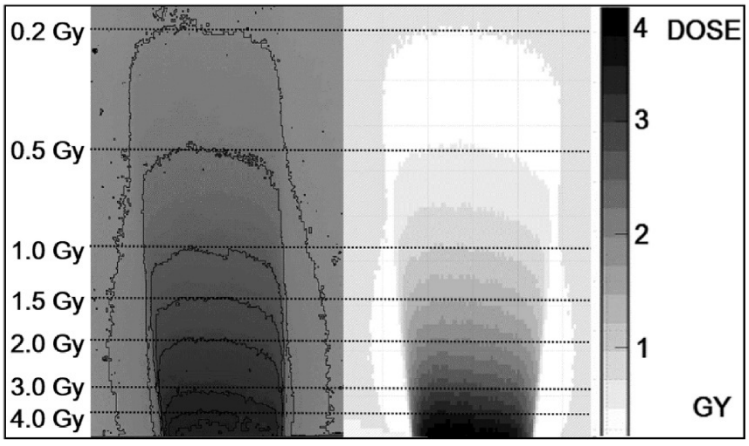

Fig. 18. Transverse plane 2D dose distribution of the irradiated PMMA slab phantom. Left – EBT2 film; right – FLUKA simulation [A1]

MCS were conducted to evaluate the energy distribution patterns using FLUKA. The simulated results were then compared with experimental data obtained from irradiated EBT2 films. The comparison revealed that the experimental and modeled dose distribution patterns were similar for both the irradiated PMMA slab phantom and the water-filled 3D-printed humanoid phantom with the incorporated metal

artifact. This demonstrates the ability of FLUKA MC code to collect and present additional data on the 3D dose distributions.

The findings for the irradiated EBT2 film are presented in **Fig. 18**, which align with the results of percentage depth dose (PDD) measurements typically performed as part of a quality assurance (QA) program. For the 4 Gy dose delivered with an X-ray generator operating at 80 kVp, the maximum depth of dose penetration was estimated to be 6 mm. In our experiments, the penetration depth was estimated to be between 6 and 7 mm, indicating a minor level of inaccuracy and showcasing the feasibility of FLUKA simulations in capturing planar dose distribution.

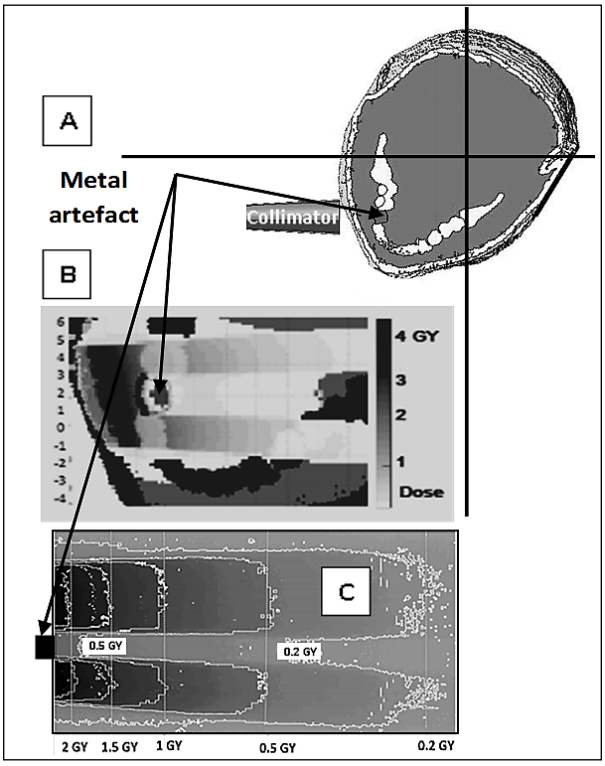

Fig. 19. 2D dose distributions on the transverse plane within the irradiated phantom containing integrated metal artifacts: A – in FLUKA simulated phantom, B – FLUKA simulated dose distribution; C – dose distribution on the EBT2 film observed just behind the metal artefact in the water filled irradiated anthropomorphic phantom [A1]

The accuracy of the dose evaluation method in radiochromic films had the most significant influence on the observed inaccuracies. To assess the reliability of FLUKA simulations for precise dose plan verification, experimental and simulation studies were conducted using a patient-specific anthropomorphic phantom incorporating a metal artifact (metal tooth in the lower jaw). **Fig. 19** demonstrates that there were no significant discrepancies between the measurements obtained from experimental EBT2 films and the results from the FLUKA model. The measured dose deviated by

a maximum of 5.4% between the experimental and simulated outcomes. The observed discrepancies were primarily attributed to the simulation geometry, with the simplified tooth model inadequately estimating the incident angle of the X-ray beam at the location where the film sheet was vertically stacked within the phantom space. These results compare well against similar works of other researchers [62, 266].

It should be noted that the absorbed dose simulations were carried out in water, which differed from the experimental measurements carried out using radiochromic films. Potential errors associated with film positioning in the phantom and geometrical uncertainties related to the approximate voxelized tooth modeling must also be acknowledged. The overall uncertainty in the evaluation process is influenced by the uncertainties in both the MC simulations, as mentioned earlier, and the dose determination using radiochromic films. This uncertainty can potentially reach up to 8%.

4.4. Gama comparison tool

The developed in-house code provides a precise evaluation of the 2D-dose/distance index (2DDI), enabling the analysis of dose distribution data obtained from various sources. By comparing MC simulation data with experimental data acquired from irradiated radiochromic films, the code was employed to generate 2DDI distribution maps. To assess the quality control of high-energy radiation treatment procedures, accuracy criteria of 3% / 3 mm were established, as commonly used in clinical practice. **Fig. 20** and **Fig. 21** present the 2D-dose/distance index distribution maps based on the selected criteria of 3% / 3 mm for all three geometries depicted in **Fig. 13**. Additionally, gamma histograms and passing rates based on the criteria are provided for the radiochromic films. However, none of the scans met the standard criteria for high-energy clinical practice, which requires a passing rate of over 95% for 3% / 3 mm. The EBT3 film demonstrated slightly better performance compared to the RTQA2 film. Among the irradiation geometries, the films irradiated from the side with the X-ray beam axis parallel to the PMMA slab surface exhibited the closest similarity between experimental and simulated dose values. The calculated passing rates for the RTQA2 film were 87% and 90% for the EBT3 film, respectively, which fell below the minimum threshold of 95% for high-energy radiotherapy, aimed at ensuring treatment precision and accuracy. Consequently, the evaluation results indicated that the chosen criteria of 3% / 3 mm were excessively stringent for kilovoltage radiotherapy due to notable differences between experimental and simulation outcomes. Thus, the criteria values were increased to 6% / 6 mm to assess the limitations of the evaluation criteria in kilovoltage therapy. **Fig. 22** ir **Fig. 23** display the results of 2DDI computations for both films using the revised accuracy requirement of 6% / 6 mm. The overall passing rate calculations for both films are provided in **Table 5**.

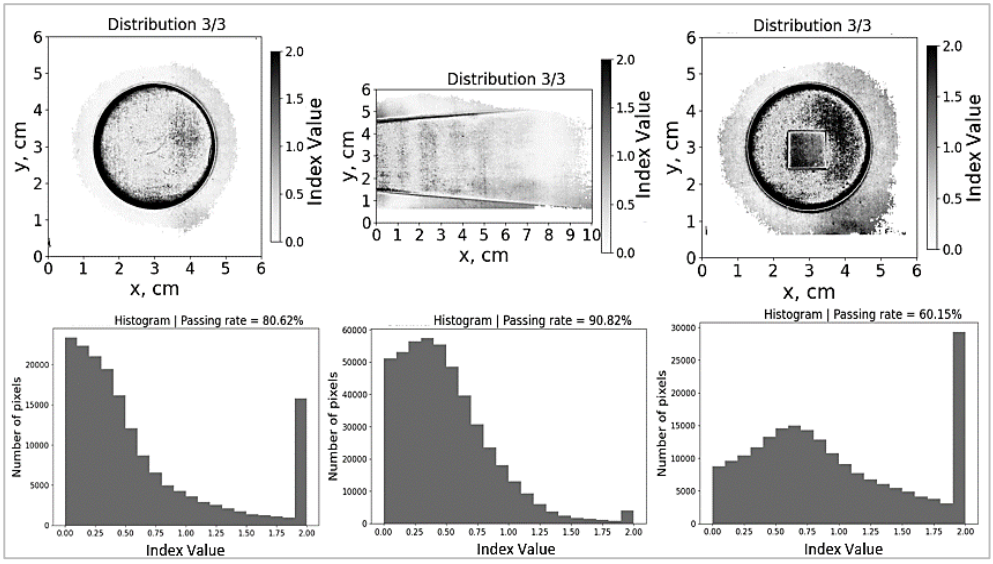

Fig. 20. Comparison between 2D dose/distance index distribution maps and passing rates of EBT3 film and MC simulation conducted for specific criteria of 3% dose difference and 3 mm distance agreement [A2]

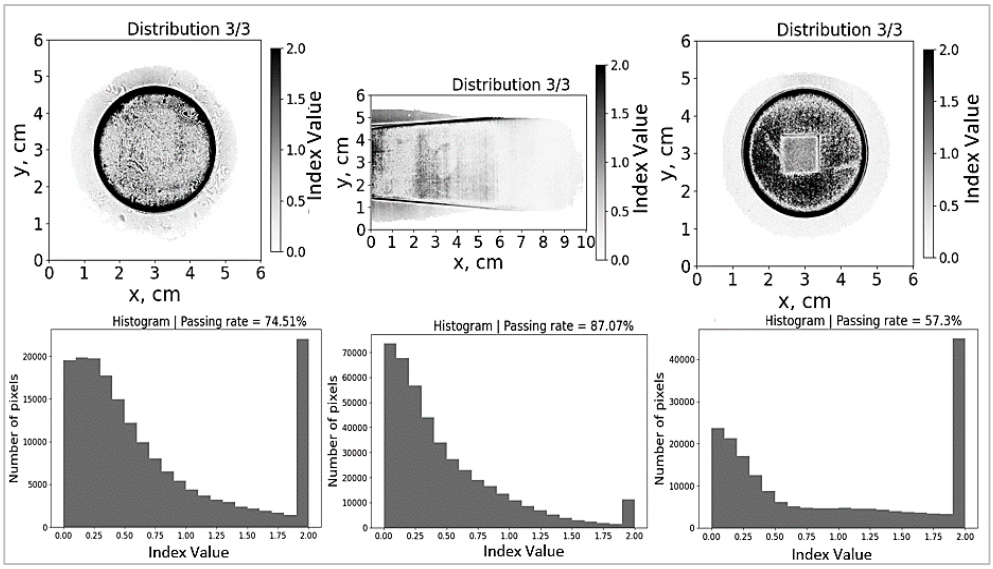

Fig. 21. Comparison between 2D dose/distance index distribution maps and passing rates of RTQA2 film and MC simulation conducted for specific criteria of 3% dose difference and 3 mm distance agreement [A2]

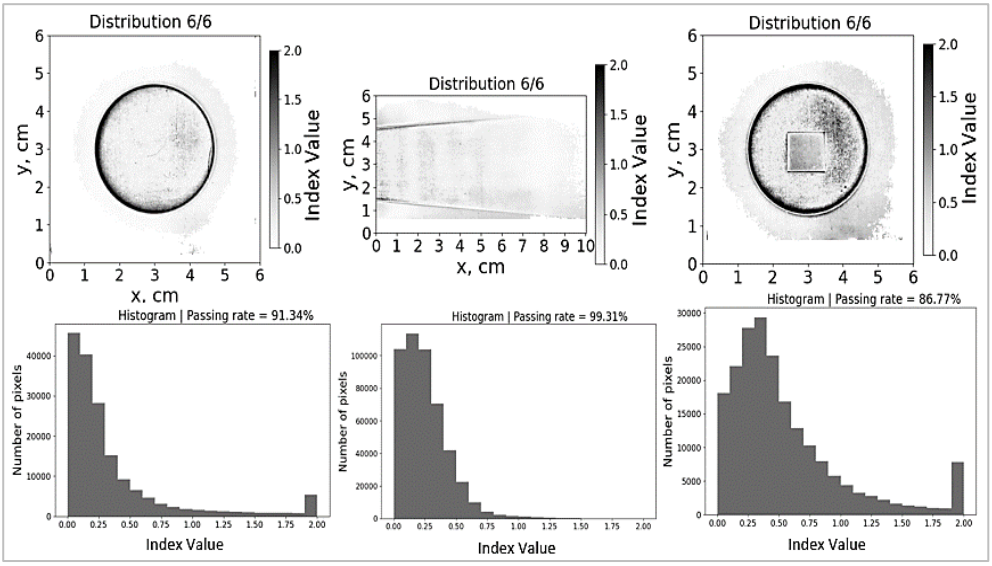

Fig. 22. Comparison between 2D dose/distance index distribution maps and passing rates of EBT3 film and MC simulation conducted for specific criteria of 6% dose difference and 6 mm distance agreement [A2]

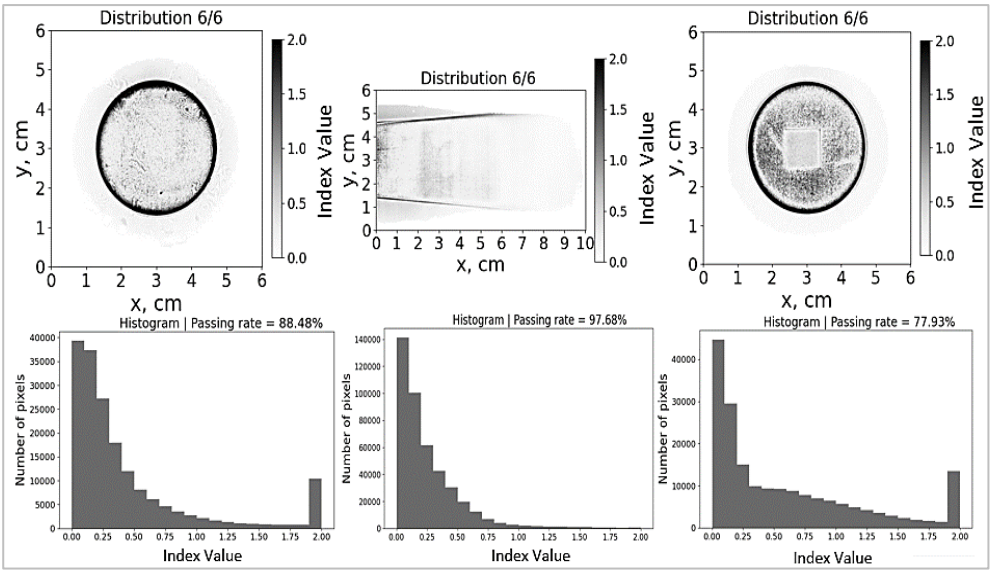

Fig. 23. Comparison between 2D dose/distance index distribution maps and passing rates of RTQA2 film and MC simulation conducted for specific criteria of 6% dose difference and 6 mm distance agreement [A2]

Table 5. Summary of passing rates for films exposed to different irradiation geometries [A2]

Film type	Criteria	Gamma passing rate		
		Geometry Nr.1: perpendicular irradiation	**Geometry Nr.2:** side irradiation parallel to PMMA slab surface	**Geometry Nr.3:** perpendicular irradiation with a Ti cube placed on the film
EBT3	3 % / 3 mm	80.62 %	90.82 %	60.15 %
RTQA2	3 % / 3 mm	74.51 %	87.07 %	57.30 %
EBT3	6 % / 6 mm	91.34 %	99.31 %	86.77 %
RTQA2	6 % / 6 mm	88.48 %	97.68 %	77.93 %

When employing the revised criteria of 6% / 6 mm, the films irradiated from the side (2nd experimental geometry) exhibited the closest agreement between experimental and simulation results. The calculated passing rates for EBT3 films were 99.31% and 97.68% for RTQA2 films, respectively. However, for the remaining two irradiation geometries, the 2DDI passing rates for both films were below the threshold of 95.00%. Notably, the irradiation geometry involving metal artifacts yielded the poorest results. A more extensive uncertainty analysis is warranted for irradiation geometries with metal artifacts. Nevertheless, in orthovoltage therapy with complex configurations, such comparisons can still be valuable for identifying problematic areas of dose delivery. Particularly in cases involving metal implants within the irradiation field, such comparisons can help prevent errors and instill confidence in the effective treatment of patients.

4.5. MC model of polymer chain growth and branching and the simulation results

This part presents the description and results of the in-house developed polymer growth model and describes its structure and principles. The developed model is presented in this part as it is treated as a result of this study, thus incorporating the description and implementation of the model in the results part. The present study utilizes Monte Carlo simulations to represent the initial phases of methacryl acid (MAA) polymerization with radical initiation, while deliberately excluding the later stages involving the conversion of initially formed MAA polymers into larger structures by secondary chemical processes. The results of this part have been published [A3].

4.5.1. Introduction

We present a novel technique for simulating radiation-induced polymerization of methacrylic acid (MAA) in aqueous solution using a coarse-grained (CG) MC (MC) approach in this research. Because of their failure to capture the complexity of the entire growth mechanisms, conventional kinetic methods are limited in their

ability to accurately characterize the formation of MAA polymers beyond a statistical average. We overcame this restriction by modeling MAA polymerization at both the individual and collective levels using the MC method (Fig. 24).

The program is based on the MC method that rely on repeated random sampling to obtain numerical results as polymer growth upon irradiation can be described by a probabilistic interpretation. Our method entails creating a simulation box numerous times, with each CG bead representing an entire monomer. The simulation box can be created of the desired size and chemical composition: the type of material of interest and its concentration, i.e. number of the material molecules per volume of the box as well as their initial configuration. Several different types of material can be added.

The chemical behavior of the interacting substances defines the growth function, which is found by repeated random sampling. Our main aim is to study the microstructure and growth pattern of radiation-induced polymerization of MAA in aqueous solution, with the ultimate goal of optimizing the synthesis of poly(methacrylic acid) hydrogels suitable for gel dosimeters and other applications.

The experimental validation is in progress and employs Nuclear Magnetic Resonance (NMR) spectroscopy so are not presented in this thesis. This method has many challenges including dealing with the solvent, fine-tuning the experiment parameters, and getting a clear signal. Therefore, the results of polymer growth simulations have been compared with the experimental work of other researchers that have used NMR spectroscopy.

4.5.2. Model data, assumptions and boundaries

Initial data and geometry optimization. The initial parameters are derived from Density Functional Theory (DFT) simulations. Quantum mechanical methods, specifically the hybrid B3LYP / def2-SVPD approach, are used to optimize the geometry of each molecular system ((MAA)n, where n ranges from 1 to 30). B3LYP is a hybrid functional that combines Hartree-Fock exchange with DFT, resulting in improved accuracy. The def2-SVPD component refers to a specific type of basis set utilized in quantum chemistry. A basis set comprises a set of functions that are used to construct the molecular orbitals, which represent the wave functions of the electrons within the molecule. The “def2” notation is indicative of the Karlsruhe (Germany) def2 series of basis sets, while “SVPD” is an acronym for Split Valence with Polarization and Diffuse functions. This particular basis set is designed to strike a balance between computational efficiency and accuracy, making it a suitable choice for complex calculations and is used to construct molecular orbitals representing electron wave functions.

The process of geometry optimization is central in this model, aimed at identifying the most stable configuration of the molecule by minimizing the total energy. This involves a series of iterative adjustments to atomic positions until the configuration with the lowest energy is found. The resulting optimized geometry is vital, providing a foundational basis for all subsequent calculations, allowing for the exploration of the molecular system’s stability and reactivity.

Energy calculation and reaction rate estimation. Once the geometries have been optimized, the objective is to determine the energies associated with bond dissociation and radical formation in the MAA molecules. This is achieved using a quantum mechanical method (B3LYP / def2-TZVPP) which includes triple-zeta valence polarization functions, which account for electron correlation effects, as well as diffuse functions to capture electron density in regions away from the molecule's core.

For the set of molecules (MAA)*n*, where *n* ranges from 1 to 30, a total of 1,826 possible bond dissociation and radical formation reactions are considered. In each reaction, the energy change is deduced by contrasting the total energy of the reactants (original MAA molecules) to that of the products (molecules manifested post bond dissociation or radical formation).

The activation energy has been estimated using the transition state theory, which is a theory used to understand the behavior of molecules undergoing a chemical reaction by focusing on the highest potential energy point along the reaction path — the transition state. The transition state is a high-energy configuration of atoms that represents a sort of "barrier" that reactants must overcome to become products. It is not a stable molecule and exists at the point of the highest energy along the reaction coordinate. In this context, the activation energy was computed as the total energy difference between reactants and the transition state (state on the potential energy surface connecting reactants and products of a chemical reaction).

The transition state geometry has been determined using the functional thrust radius Newton-Raphson algorithm, following along the collective chemical reaction coordinate. The obtained transition state geometries have been verified by computing the geometrical Hessian of these geometries and verifying the correctness of the curvature of Potential Energy Surface (PES) at the transition state geometry. A correct transition state geometry will have a curvature indicating it is a saddle point on the PES, meaning it is a maximum along the reaction coordinate and a minimum in all other coordinates. This procedure has been applied to all considered chemical reactions and activation energies determined.

Once the activation energies were obtained, they were incorporated into the Arrhenius equation:

$$k = A * exp(-E_a / (R * T)), \quad (22)$$

where

- k is the rate constant;
- A is the pre-exponential factor;
- E_a is the activation energy;
- R is the gas constant (8.314 J/(mol·K));
- T is the temperature in Kelvin.

This allows the estimation of the speed at which the reactions occur under given conditions, which serves as input data into MC simulation.

Input into MC Simulation. The rates of individual reactions, obtained from DFT calculations, can be converted into probabilities for a Monte Carlo model. These probabilities essentially represent the likelihood of each reaction occurring in a given

simulation step. The estimated reaction rates are then incorporated into probability calculation formulas that best fit the obtained data set. In the Monte Carlo simulation, reactions are randomly selected based on their rates and "run" to simulate the polymer growth. This process is repeated many times to generate a distribution of outcomes, providing a probabilistic understanding of the polymer growth under irradiation in a water solution.

Each simulation step begins with a randomly created radical and its proximity to a monomer is evaluated. Depending on the calculated probabilities, a growth or decomposition reaction occurs. The monomer or oligomer undergoes random rotations and translations following set criteria. A collision check ensures the physical feasibility of the molecular alterations. If a collision occurs, the step is rejected, and the system reverts to its previous state. Otherwise, the simulation progresses. This process is iterated multiple times until an equilibrium representing the polymerization process is reached.

Choosing a simplified model for polymer growth, primarily focusing on combination and break-down reactions, hinges on computational efficiency and theoretical clarity. Polymerization involves numerous particles and diverse reactions, necessitating a trade-off between detailed representation and computational feasibility. The simplified model permits meaningful insights without overtaxing computational resources. It offers an introductory understanding of polymer growth, concentrating on fundamental mechanisms crucial to the final properties of the polymer. Simplification also enhances result interpretability, enabling more straightforward inference from the data, particularly beneficial in early research stages. Additionally, the complexity of the model can be incrementally increased for deeper understanding, following an initial grasp of basic behavior.

The comprehensive list of assumptions and boundaries of this model:

- **Initial conditions:** the simulation starts with only monomers in the box, i.e., there are no pre-existing polymers or radicals. It is assumed that the monomers are randomly distributed throughout the box. In real systems, there will be already some percentage of oligomers formed. Additionally, the model maintains a closed system, restricting the entry or exit of monomers during the simulation. The solvent itself is not modeled and treated only as an effective source of radical creation.

- **Geometry boundary constraints**: the simulation operates within a fixed boundary, specifically, a box measuring 50 x 50 x 50 nm. The monomers are confined within this spatial parameter and are restricted from escaping. Upon contacting the edge of the box, monomers are conceptualized to "rebound" back into the constrained space. Additionally, the methacrylic acid molecule ($C_4H_6O_2$) is geometrically simplified, represented as a hexahedron with dimensions 5 x 5 x 2 Å.

- **Growth boundary constraints:** the simulation aims to observe polymer growth until it stabilizes, marking the completion point of the simulation. It is emphasized that polymers, in this context, refer to oligomers.

- **Quantum mechanical accuracy**: the rates of bond dissociation and radical formation are meticulously calculated using the hybrid B3LYP / def2-TZVPP model, ensuring substantial accuracy in quantum chemical simulations. The precision of our

model fitting from these simulations is reliable to within 3–4 kcal/mol. This level of accuracy is critical in ascertaining the reliability and the scientific validity of the simulation results in representing the actual chemical behaviors and reactions.

- **Reaction rates**: the reaction rates used are derived from DFT and treated as constants. However, in a real dynamic system, these rates could vary depending on local conditions like pH, temperature, and local concentration, which are not accounted for in the current model.
- **Energy**: we assume that the temperature of the system is constant and does not fluctuate during the simulation. The irradiation energy is constant at 20cGY/min. We assume that the irradiation source is constant and does not fluctuate during the simulation.
- **Physical feasibility check**: The collision check in this model is a simplification of the physical reality. It does not take into account other forms of molecular interaction like Van der Waals forces, steric effects, or electrostatic interactions, which could affect the feasibility of a reaction.
- **Reactions simplification**: we consider only the initial stage polymerization under constant radiation flux, including only certain combination, breakdown, and translation/rotation events. The following effects and reactions are excluded:
  - The model accounts only implicitly for termination reactions in free-radical polymerizations. This could potentially lead to an overestimation of the degree of polymerization and the number of active radicals. The model does not take into account disproportionation termination events.
  - Secondary reactions, like backbiting and intramolecular reactions, are not considered in the model. These can impact the structure and properties of the resulting polymer.
  - Intramolecular Crosslinking Reactions (only intermolecular crosslinking is considered).
  - Secondary Radical Reactions.
  - Solvent and Oxygen Effects.
  - Diffusion-Limited Reactions. The model does not consider diffusion limitations, so it may not accurately capture the influence of slow diffusion on reaction rates in the system.
  - Spatial effects in real polymerizations, such as local temperature or monomer concentration variations and areas of radical or polymer entrapment, may not be accurately represented in this homogeneous MC model.
  - Proton Transfer Reactions: MAA can donate a proton to water, forming a methacrylate ion and a hydronium ion. This acid-base reaction can affect the pH of the solution and influence the reaction rates.

Each of these elements adds complexity to the simulation but can influence the final structure and properties of the polymer. However, incorporating all these factors would significantly increase the model's complexity and computational requirements, necessitating a balance between accuracy and feasibility. Despite these potential drawbacks, this modeling approach still offers a robust and powerful tool for

understanding polymerization processes, though one must be mindful of its limitations and assumptions.

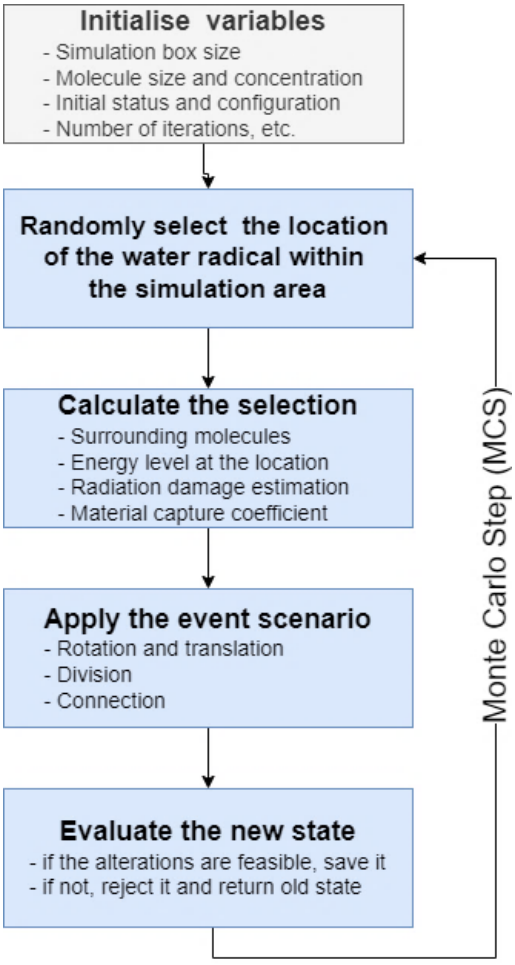

Fig. 24. MC implementation for polymer growth model

4.5.3. Implementation details

The growth of polymers in response to irradiation can be described by a probabilistic interpretation. To simulate this process, a simulation box of the desired size is initialized and filled with the material of interest at a specified concentration, along with its initial configuration (**Fig. 24**). The MC cycle is then started as per the defined algorithm (**Fig. 25**). During each iteration of the MC cycle, a random location is selected within the boundaries of the model box to simulate the possibility of a random radical appearance. Next, it is checked whether there is a molecule of interest within a certain distance that would be affected by the radical creation. If such a molecule exists, the energy calculation for radiation damage and material capture is

performed, which sets the possible combination or break-down event sequence based on these energy calculations.
There are three possible cases at this stage: (1) the molecular structure changes after a successful combination event, (2) the molecular structure changes after a successful break-down event, or (3) the structure remains unchanged if none of these events are successful. In all cases, the next step involves the calculation of rotation and translation, followed by a final feasibility check that verifies that the changes made are physically possible, i.e., there is no unacceptable intersection of the simulated bodies. Depending on the result of the feasibility check, the changes made are either retained, and the simulation box is updated, or reversed. The pseudocode of this part is shown in **Fig. 26**.

Require:
Generate box with initial conditions

while $N_{iterations} \neq 0$ **do**
  $Location_{XYZ} \leftarrow x, y, z$
  if $E_{Location} \geq E_{radical}$ **then**
    if $MonomerExists(Location_{XYZ}) \leftarrow true$ **then**
      $Activation \leftarrow true$
      calculate $P_{capture}$
      calculate P_{damage}
      procedure EVENT HANDLING($P_{capture}, P_{damage}$)
        return *EventStatus*
      end procedure
      if $EventStatus \leftarrow true$ **then**
        save new system state
      else
        return old system state
      end if
    end if
  end if
end while

Fig. 25. Pseudo-code implemented for MC cycle of polymer growth model

MC simulations rely heavily on pseudo-random number generators. In general, the output of a simulation may be affected by the quality of the Random Number generators (RNGs). RNGs are algorithms that are used to generate an unpredictable sequence of numbers. Intel Math Kernel Collection (Intel MKL)[267] is a library of extensively threaded and performance-optimized math kernel subroutines. This project employs the vector type Mersenne Twister pseudorandom number generator (MT19937) from MKL to produce a uniform discrete sample distribution. The period of the generator is 219937^{-1}, and it has excellent multidimensional uniformity and statistical features. Since the generator is also relatively fast compared to other techniques of comparable quality, it is extensively employed in simulations that require large quantities of high-quality random numbers.

```
Require: P_capture, P_damage
Ensure: Activation ← true

if P_capture ≥ P_damage then
    applyConnection(R_c)
    applyTranslationRotation(R_rt)
    if R_rt ← true then
        checkFeasibility(R_f)
        if R_f ← true then
            Continue
        end if
    end if
else
    applyBreakdown(R_b)
    applyTranslationRotation(R_rt)
    if R_rt ← true then
        checkFeasibility(R_f)
        if R_f ← true then
            Continue
        end if
    end if
end if
```

Fig. 26. Pseudo-code for event handling

The molecule of methacrylic acid was geometrically approximated as a hexahedron with dimensions 5˚A x 5˚A x 2˚A. Initial simulation box geometrically bounds the simulation volume and generates mono-, di-, and trimers of the roughly same amount at the default concentration. The bond angle is equal to 109.5°, which corresponds to the bond angles of carbon atoms. The Rotation-Translation event calculates the moment of inertia of the specified structure and creates random rotations and translations based on this value. The object is then rotated and translated along the X, Y, and Z axes by a random amount. The maximum permissible distance is 600 percent of the molecule's longest edge.

The break-down event forces the structure of interest to be segmented off into new distinct objects at the event point. Combination event implements the possible scenarios of connection of the structures when the activated molecule is within a certain distance from the other surrounding bodies. The selection of the exact Combination scenario depends on the configurations, locations, and lengths of the structures of interest. The objects may merge by interconnecting within the new entity, hence expanding its size. When both or one of the objects are small, or when the activation point is close to the end, the shorter object joins to the longer object, and the chain grows. In the case of larger complicated, branched structures the combination via the activation point may produce the new interconnected structure. In other scenarios, an object may become a branch of another object and create a branched structure. Depending on its size and activation point, the object may either produce a single branch or split into two branches at the activation point. Other

combination scenarios include the complicated swaps where the activated structures may break down at specific spots and join the split portion of another structure, thus creating new structures with new connections and relationships.

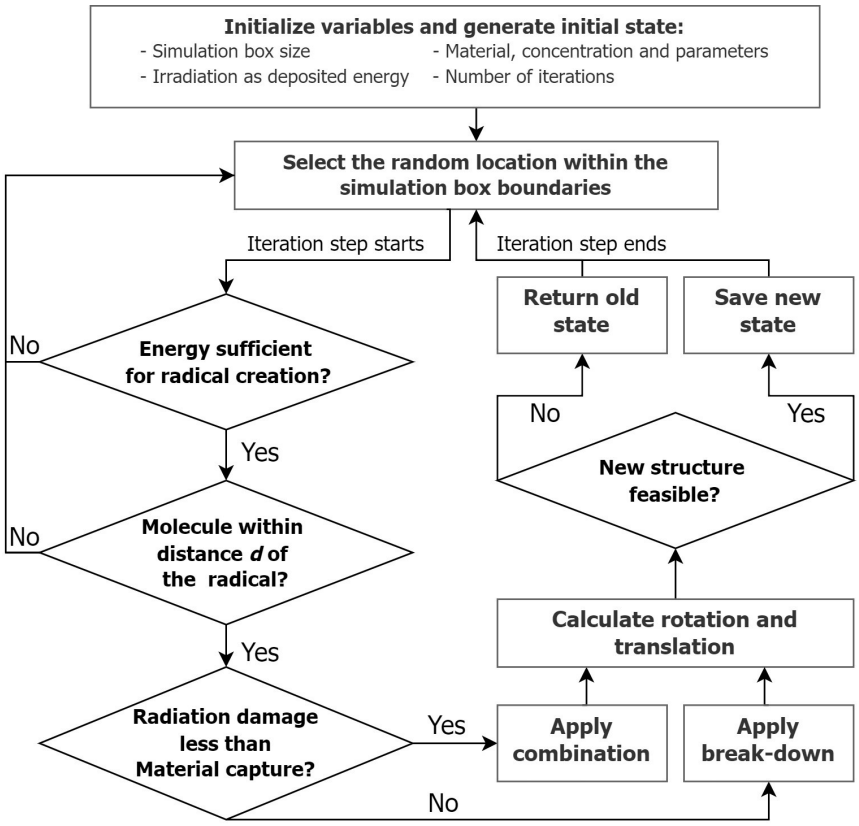

Fig. 27. Code flowchart of an MC cycle

The feasibility check consists of the identification of collisions and is required for the control and rejection of physically implausible outputs generated by a random engine. Collision detection is the computational issue of detecting the intersection of two or more objects, and it is a complicated area that offers a variety of ways for efficiently tackling the problem. In contrast to the detection of sphere collisions, the detection of cuboids necessitates a more complex method, which must be as efficient as feasible owing to the high number of cuboids and the needed number of iterations. The Gilbert–Johnson–Keerthi (GJK) distance method is a technique for calculating the shortest distance between two convex sets. The class itself was adapted from OpenGJK library [268], which presents the fastest and most accurate version of the GJK algorithm available to date.

The complete detail flowchart for an MC cycle is shown in **Fig. 27**. In the simulation, a box of material and its concentration is initiated. A random location in the box is selected, energy is checked to see if it can create a radical. If a molecule is

within range, energy calculations are made for radiation damage and material capture. Three outcomes are possible: changed molecular structure, unchanged structure, or no event. For the first two cases, the new coordinates are calculated, and a feasibility check is performed. If the changes are physically possible, the simulation box is updated.

4.5.4. Code structure description

The code is written in the general-purpose computer language C++ version 17. The structure of the code is categorized as follows:

- Geometry group that describes the interacting physical bodies in simulations. It consists of the following major classes:
    - Class Cuboid that implements the geometric cuboid shape representing molecules.
    - Class Monomer that implements the monomer unit.
    - Class Polymer that implements the polymer unit, that is, the chain of monomer units.
    - Class Branched that implements the structure of polymers/monomers that are interconnected.
    - Class Box that implements the geometry and functionality of the simulation box.
- Functional group that acts as a support system for the activities of the interactions between the geometrical bodies that represent molecules and is comprised of the following major classes:
    - Class OpenGJK, which implements the Gilbert-Johnson-Keerthi (GJK) algorithm for calculating the shortest distance between two convex sets. It is utilized in the model for collision detection.
    - Class ExponentialMap describing the rotation of interacting geometrical components.
    - Class MathOperations, which implements the numerous general mathematical functions, including the matrix operations necessary for calculating the location of interacting geometrical bodies.
    - Class Visualisation implements the graphical view of the generated geometrical bodies within the boundaries of the simulation box.
- Event group describes the actions of the geometrical bodies representing molecules and their interactions utilizing these major classes:
    - Class Rotation-Translation implements the rotation and translation of the given geometrical structure inside the bounds of the simulation box.
    - Class Division implements the event of division i.e. the breakdown of a specific geometrical structure.
    - Class Connections implements the connection event, which consists of the assembly of geometric bodies coupled at particular angles and distances.
- MC group is responsible for running the MC algorithm and contains the following major classes:

- Class Random Generator that implements Intel MKL VSL based Mersenne Twister pseudo-random number generator MT19937 with uniform random number distribution.
- Class Structure Generator is responsible for creating the initial set-up of the simulation box, i.e. the number and initial position, rotation and configuration of the geometrical bodies representing molecules of the monomers and polymers.
- Class MCDriver collects the various values and other factors required for the simulation and iterates the algorithm the specified number of times.

Geometry group. The Cuboid class denotes the geometrical approximation of the molecule as a hexahedron, a six-sided solid whose length, breadth, and height are freely selected. The units of measurement are angstroms (10^{-10} m). The class's primary functions are as follows:

- Calculate the relative center of the cuboid.
- Calculate the relative center of the bottom face of the cuboid.

For instance, the molecule of methacrylic acid (C4H6O2) was geometrically approximated as a cuboid with dimensions of 5 angstroms in length, 5 angstroms in width, and 2 angstroms in height (**Fig. 28**).

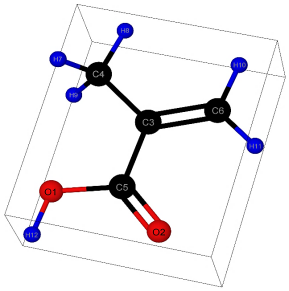

Fig. 28. Molecular model of methacrylic acid monomer within its bounding box approximated as 5x5x2 Å cuboid

Cuboid class is encapsulated by the Monomer class to form the monomer molecule's geometry. Absolute coordinates are added to each vertex of the cuboid to complete the implementation of the monomer molecule. It includes utilities to set and receive the true coordinates of the monomer within the simulation box in addition to the geometrical properties that are associated with the geometry of the monomer.

The Polymer class is responsible of generating the polymer object, which is a simulation of the ability of monomer molecules to combine to form polymers. The attributes of the object include the following:

- the collection of Monomers [units] that comprise the Polymer
- the set of rotations for each Monomer in the Polymer
- unique ID of the structure
- type of the polymer
- polymer origin coordinates

Visually, it displays as a chain of randomly connected structures of varying lengths with a bond angle of 109.5°, which corresponds to the bond angles of carbon atoms (**Fig. 28**). Note that the Polymer object produces only linear polymer objects with no branches or complex structures. The Polymer object is a key code structure and has numerous crucial functionalities, all of which will be discussed in greater depth in the succeeding sections.

The starting location of each consecutive monomer in the construction of a polymer object is determined by using the center of the top face of the previous monomer as the starting point for that monomer's bottom face. In addition, each Monomer has its own set of rotation data, which is controlled by the ExponentialMap class and is represented in terms of the axis-angle notion. In the end, the absolute coordinates of each Monomer object's vertices are calculated and added to the object.

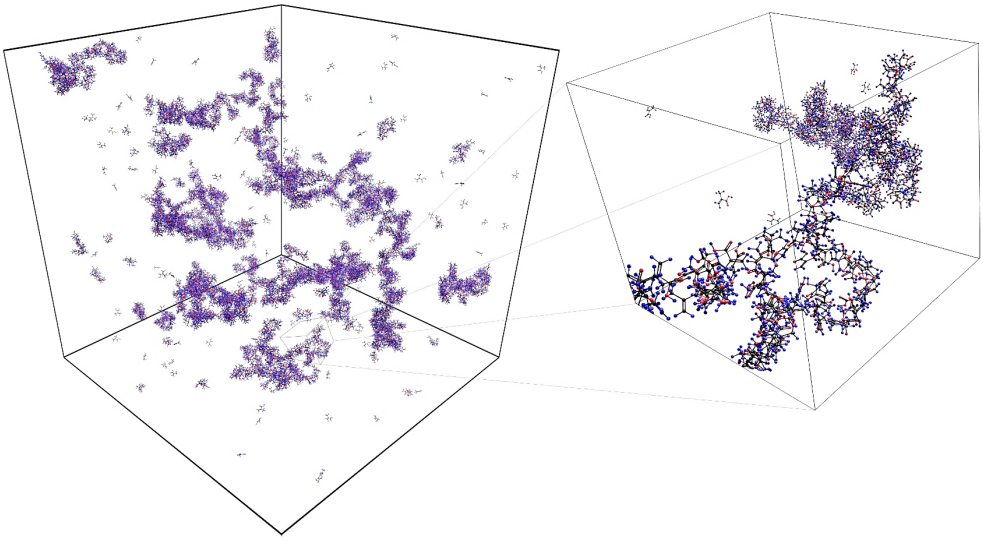

Fig. 29. The geometry of simulated polymers in 50 nm x 50 nm x 50 nm simulation box

The newly projected Monomer is randomly produced by the StructureGenerator class with the selected bond angle. Then the method for adding up the Monomers takes the proposed input of a newly generated Monomer object and its rotation and executes the collision check operation to determine whether or not the proposed new Monomer intersects the chain that is being constructed, i.e. is physically feasible. The Gilbert–Johnson–Keerthi distance algorithm is used, which is implemented by the OpenGJK class. The specifics of it are discussed in the part dedicated to the OpenGJK class. If the proposed Monomer can be realized physically and does not induce unwanted intersections, it is added to the chain, and the Polymer object is updated.

Other methods used in Polymer include but are not limited to:

- Function for dividing the chain into two distinct Polymer objects
- Rotation function for rotating the entire chain
- Calculation of the chain's mass center
- Operation that reverses the chain

- Additional checks to verify the polymer's position, coordinates, ID, kind, and configuration, among others

Objects made of polymer are intended to connect with one another under certain conditions. Once a Polymer object joins to another, it comes under the control of the Branched Polymer class, which enables the management of structures formed by interconnected chains. Each such structure - Branched Polymer - has its unique identifier, which allows for the identification of all the chain members of the structure, as well as the identification of the parent polymer, which is the longest chain in the structure.

Branch Polymer class describes the branched polymers. In branched polymers, monomers are bonded together to produce long chains that have side chains (branches) of varying lengths that originate at random places from a single linear chain. These side chains can range anywhere from a few to hundreds of monomer units in length. Branch Polymer has functions for removing, adding, and modifying Polymer objects as required. It also computes the structure's configuration:

- Branch level
- Branch size
- Point of branch junction

Additionally, the structure division function is provided, allowing even the most complex structures to be divided at the desired location. The outcome of such a division might be two new structures, a structure and the Polymer(s), or merely Polymers if the structure is divided into distinct unbranched chains. In addition to the division and merge operations, Branched Polymers can be swapped, i.e. the structure of two Branched Polymer objects can be exchanged. All of these functions imitate the actual polymer dynamics and permit the creation of diverse scenarios for connections and divisions based on the values of specific variables (**Fig. 29**).

Class Unit Box maintains the confined space in which created objects may be translated, rotated, and undergo different structural modifications. It comprises arrays of Polymer and Branched Polymer objects and has a length, width, and height that match to the box's simulation dimensions. It also contains an array of irradiation **Event group.** The Polymer item can take part in three significant occurrences:

- Polymer structure moves and rotates in a confined space (Rotation – Translation).
- Polymer structure breaks (Division)
- Polymer structure join other bodies (Connection)

The related classes are responsible for managing these events. The structure may be subjected to Division and Rotation-Translation, Connection and Rotation-Translation, or Rotation-Translation solely based on the computations (**Fig. 30**).

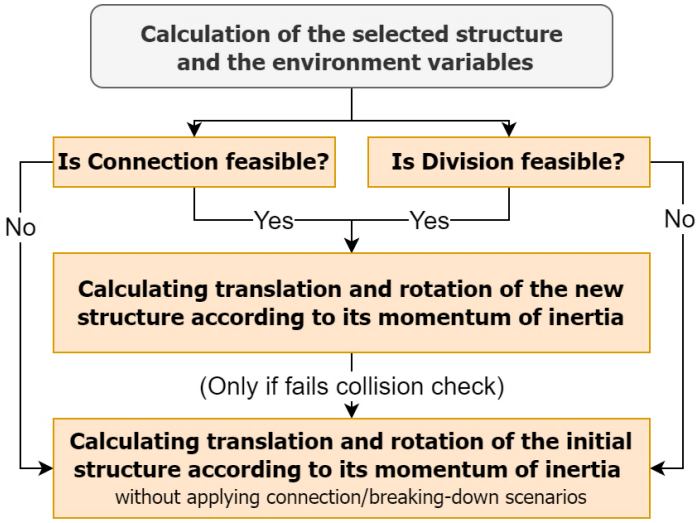

Fig. 30. Event handling flowchart

The Rotation Translation class calculates the moment of inertia of the specified structure and creates random rotations based on this value. The object is then rotated relative to its mass center and translated along the X, Y, and Z axes by a random amount. The maximum permissible distance is 600 percent of the molecule's longest edge. In the example of methacrylic acid material, where the longest edge of the molecule is around 5 angstroms, the translated distance can be chosen at random between 5 and 30 angstroms.

The Division class provides the functionality that allows the Polymer and Branched Polymer objects to be segmented off into their own distinct new objects at any point that the user specifies. The outcome will be determined by the sort of new item that was created; for example, a branched polymer may break down into two polymers or two more branched polymers, depending on the size it was when it started and where it broke down. It also has a function to check if the new objects do not intersect between each other, i.e. if the result is physically feasible.

The Connections class is responsible for analyzing and implementing the possible scenarios of connection of Polymer and Branched Polymer objects. If the calculated capture value is suitable for the connection event, the analysis for the type of connection is performed. The main selection criteria depend on the actual properties of the activated Polymer and the reacted Polymer objects:

- Configuration and complexity of the objects (branched or non-branched, parent or branch, etc.)
- The location of activation points within the objects
- The length of objects

Depending on the criteria above, the three main connection scenarios are implemented: merge, branch, and swap (**Fig. 31**).

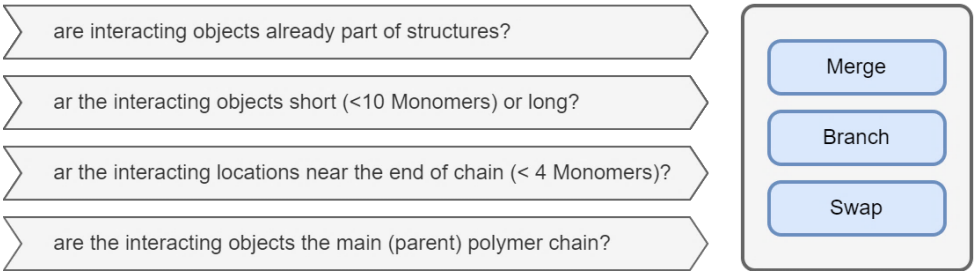

Fig. 31. Selection chart of polymer connection scenarios

In the first group of scenarios, objects may merge by interconnecting within the new entity, hence expanding its size. When both or one of the objects are small in size, or when the activation point is close to the end, simple merge possibilities arise. In this situation, the shorter object joins to the longer object, and the chain grows. In the event that both items are complicated, branched structures, they connect via the activation point to produce a larger, interconnected structure. The second scenario group forms branches. A Polymer object becomes a branch of another Polymer object, resulting in the creation of a Branched Polymer object. If the triggered item is already a Branched Polymer object, the newly generated branches will be added to it. Depending on its size and activation point, the Polymer object may either produce a single branch or split into two branches at the activation point. In the third group, activated Branched structures may break down at specific spots and join the split portion of another structure, so creating new structures with new connections and relationships.

MC group. MCS part of code is responsible for implementation the actual MC simulation. The main classes are Random Generator, Structure Generator and MC Driver.

In order to implement any of the MC methods in a computer program, random numbers must be generated. Random Number Generators (RNGs) are algorithms or methods that can be used to generate an unpredictable sequence of numbers. Intel Math Kernel Collection (Intel MKL) is a library of extensively threaded and performance-optimized math kernel subroutines. This project employs the vector type Mersenne Twister pseudorandom number generator (MT19937) from Intel's Math Kernel Library (MKL) to produce a uniform discrete sample distribution. The generator's period is 219937^{-1}, and it has excellent multidimensional uniformity and statistical features. Since the generator is also relatively fast compared to other techniques of comparable quality, it is extensively employed in simulations that require large quantities of high-quality random numbers. The class constructs and initializes a stream, invokes MT19937 RNG, and generates an integer or float random number within the specified interval. A time point indicating the current time that is created by the *std::chrono* library is commonly used as a seed in methods that must call RNG.

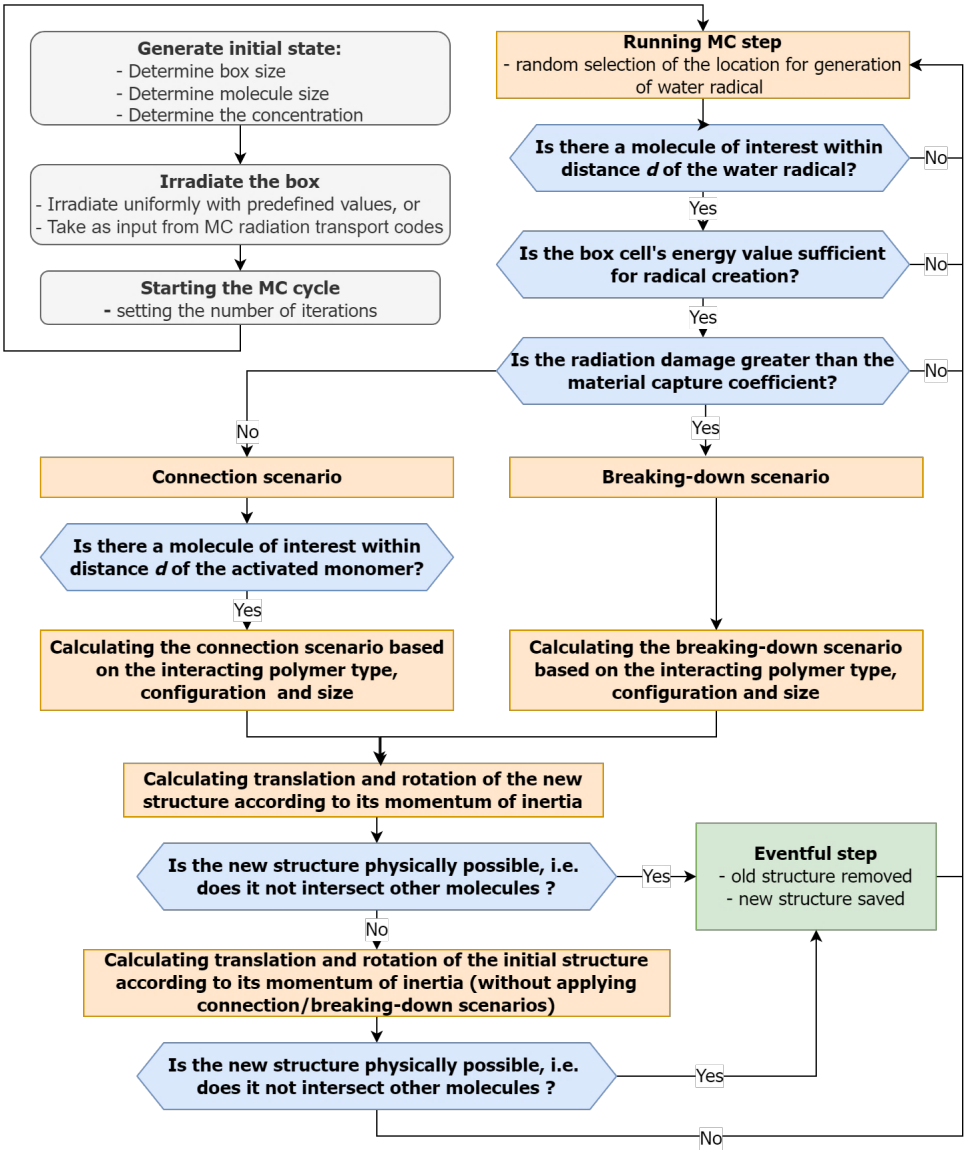

Fig. 32. Detail MC flowchart for polymer-growth simulation step

Class Structure Generator implements the random initial state of Unit Box with the specified length, width, and height. The determined default concentration of Monomers representing Methacrylic Acid molecules is 47 per 1,000 nm^3. The default setup generates monomers, dimers, and trimers with equal probability, so the initial Unit Box will contain roughly equal quantities of polymers of varying sizes. With the specified settings, the size of the box, the type of molecules, their concentration, and their configuration may be easily modified.

Class MC Driver implements the MC cycle in the following way:

- Generating the Unit Box filled with Polymer of initial status
- Irradiating the Box by placing a 3D grid on it and assigning an energy value to each cell
- Starting the cycle. In each step:
- Selecting random cell in the Unit Box, simulating the formation of a water radical, and choosing the nearest molecule next to it
- Computing radiation induced event probability (material capture coefficient + current radiation field)
- Checking if the reaction is chemically feasible:
- Computing of chemical activation probability (Connection scenario)
- Computing of chemical breakage probability (Division scenario)
- Checking if the results are physically feasible:
- Checking if new structures do not intersect with other molecules (Collision Detection)
- If collision not detected, the new structure is saved, and the box is updated
- If collision is detected, the new structure is destroyed, and the old state of the box is returned.

The simulation process is schematically shown in **Fig. 32**.

4.5.5. Simulation details and hardware performance

The default input variables with their default values are listed in **Table 6**.

Table 6. Default variables in the polymer-growth MC simulation code

Input variable	Description	Default value
MOLECULE_SIZE	Sets the size of cuboid that approximates the molecule. The default value is set for methacrylic acid monomer.	L = 2 Å W = 5 Å H = 5 Å
BOX_SIZE	Sets the bounding space for simulation volume.	L = 500 Å W = 500 Å H = 500 Å
DENSITY_FACT	Sets the number of molecules per volume. The factor of 1.0 corresponds to 47 molecules / 1000 nm^3.	1.0
DOSE_GRID	Sets the size of cell which is assigned the energy value from irradiation	5 Å
DOSE_VALUE	Sets the absorbed dose value for homogenous irradiation or takes the value from input file in case of heterogenous irradiation. Typically, the input file would be generated from particle physics MC simulation packages such as FLUKA, GEANT4, etc.	-

DOSE_REDUCTION	Sets the coefficient for change in energy values in case of successful MC step.	-
DOSE_THRESHOLD	Sets the limit in which the energy value is too low to proceed with further event step.	-
CONNECTING_DIST	Sets the radius within the activated molecule engages other monomers if chemically feasible. Default value is set for methacrylic acid monomer.	15 Å
TRANSLATING_DIST	Sets the radius within the activated molecule randomly moves if chemically feasible. Default value is set for methacrylic acid monomer.	30 Å
ITERATIONS	Sets the numbers of iterations in the simulation.	50 000 000

The probability of chemical activation (connection) $Pact(U)$ for methacrylic acid monomer is calculated in Eq. 29:

$$Pact(U) = X\big((1 - F) + F * \mathrm{erf}(G * U)\big) \quad (23)$$

The probability of chemical break-down (division) $Pbrk(U)$ for methacrylic acid monomer is calculated in Eq. 30:

$$Pbrk(U) = X\big((1 - F) + F * \mathrm{erf}(G * U^2)\big) \quad (24)$$

The fitting parameters *X, F, G* for both functions were acquired by carrying out calculations of formation and breakdown chemical reactions energies for MAA polymers. The fitting procedure assumes samples are under continuous irradiation of γ-rays (20 cGY/min), and $P_{act(U)}$ and $P_{brk(U)}$ functions are selected according to kinetic MMA polymers growth model. The data for calculations of probabilities of chemical activation and break-down is taken from the quantum chemical computational model which predicts the electronic structure of molecules using the hybrid B3LYP exchange-correlation functional and the def2-SVPD basis set (**Table 7**).

Table 7. Probability data from quantum chemical calculations in water

Size of polymer	X	F	G
1 monomer	1.00	0.00	0.00
2 monomers	0.83	0.80	1.00
3 monomers	0.72	0.80	5.20
4 monomers	0.59	0.40	3.71
5 monomers	0.51	0.60	1.28
6–10 monomers	0.23	0.75	0.42
11–15 monomers	0.20	0.67	0.36
>15 monomers	0.18	0.60	0.33

The speed of iterations varies depending on the complexity of the structures that are being formed and starts from 1.3 hr per million iterations in the beginning and ending up to 1.9 hr per million iterations for a 50 nm x 50 nm x 50 nm box of default concentration. Various box sizes up to 70 nm x 70 nm x 70 nm were also simulated; however, the assessed statistics did not change much after the box size above 40 nm x 40 nm x 40 nm x 40 nm. Simulated boxes of 30 nm x 30 nm x 30 nm in size give chemically infeasible outcomes; hence, the effect of box size on the properties of this scale is regarded to be negligible once it reaches the minimum allowable size of 40 nm x 40 nm x 40 nm.

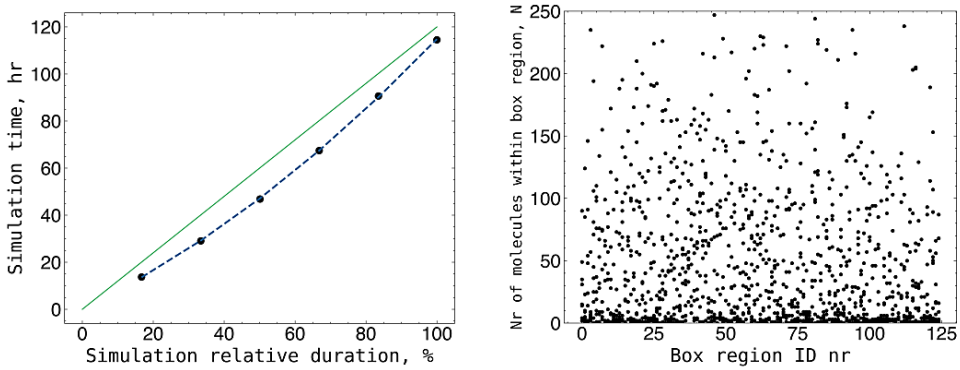

Fig. 33. Left – speed of the simulation for 50 nm x 50 nm x 50 nm box of default concentration (5,875 molecules). Right – an evaluation of the randomness of box structures based on the number of monomers in smaller box areas.

To evaluate the randomness of the created structures, the default size Box was divided into 125 smaller cubes measuring 10 nm x 10 nm x 10 nm x 10 nm, and the quantity of monomers in each cube was determined. The number of monomers determined for each cube was then compared to the number of monomers calculated for the equivalent cube in the other boxes. In total, 10 default-sized boxes were examined for structural similarities in this manner. The determined average deviation of 51.9 indicates that the produced structures in the various boxes have no correlation (**Fig. 33**).

4.5.6. Simulation results

In each Monte Carlo simulation, 60 million random walk steps on the chemical events space have been carried out to mimic the growth of MAA polymers under the homogeneous flux of constant gamma-radiation. We observed the formation of complex branched MAA polymers with a distinct grouping of smaller branched polymers into an agglomeration of MAA polymers. A typical MAA polymers growth pattern in our Monte Carlo simulations with the corresponding results of evolution of averaged MAA polymer backbone and overall polymer length during simulation is displayed in **Fig. 34** to **Fig. 38**, where the initial formation of MAA polymer agglomeration centers is already observed after 10 million Monte Carlo steps.

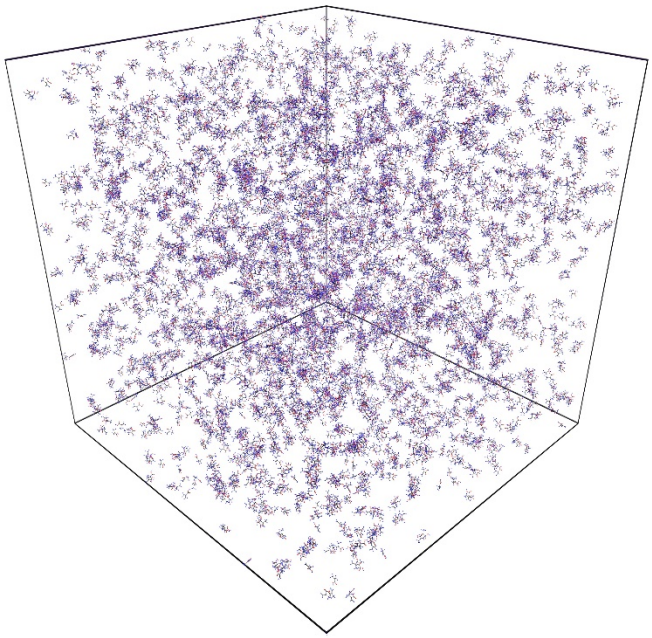

Fig. 34. Initial status of the simulation box: iteration number zero

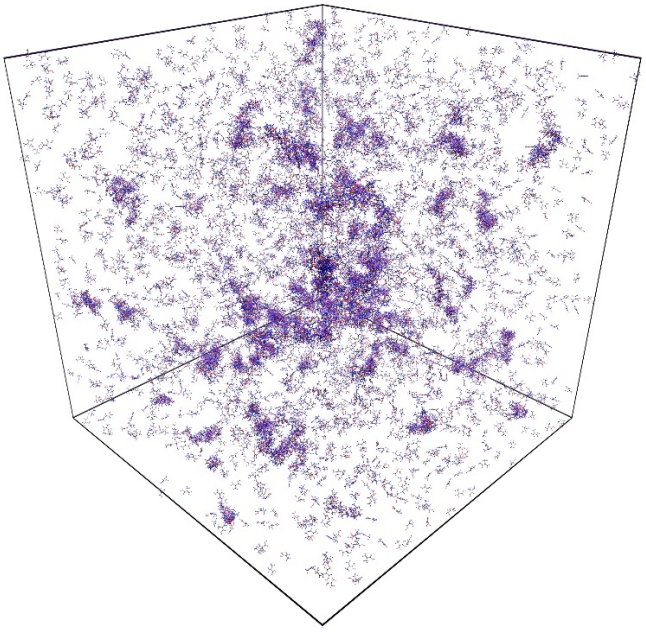

Fig. 35. The status of simulation box at the iteration step 10 million

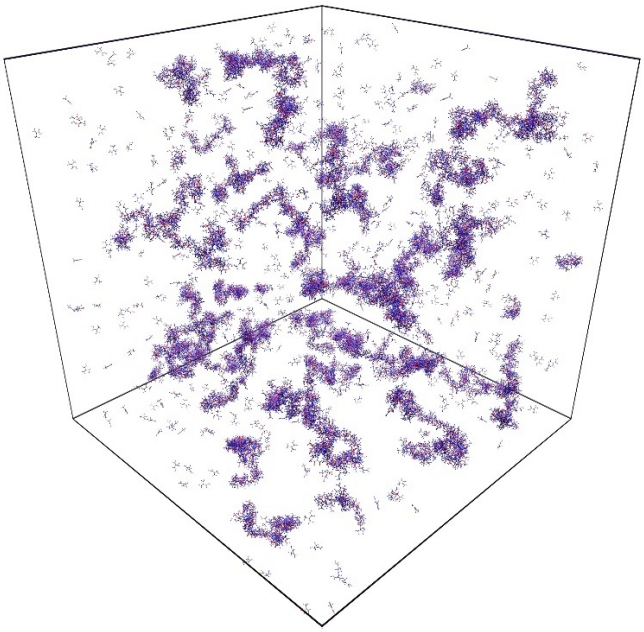

Fig. 36. The status of simulation box at the iteration step 30 million

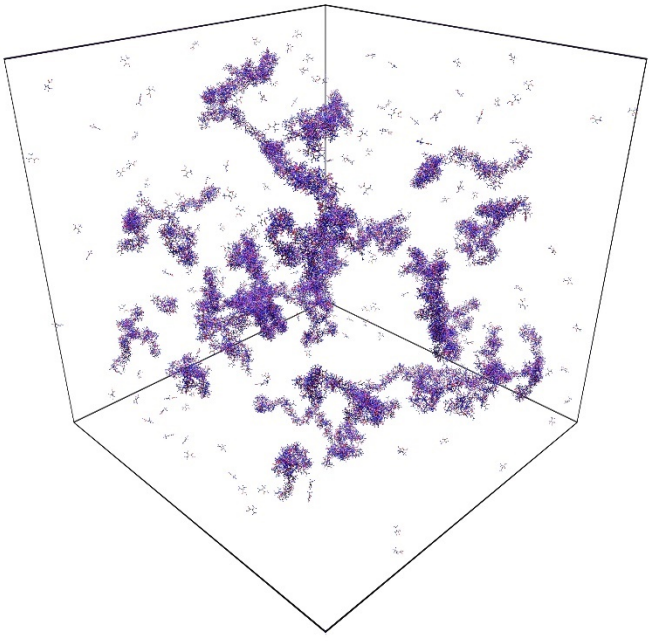

Fig. 37. The status of simulation box at the iteration step 50 million

The culmination of the initial branched polymer consolidation process occurs after 50 million Monte Carlo iterations, leading to the attainment of relatively stable amalgamations of MAA polymers. During this phase, the backbone of the MAA polymer exhibits an average length of 35 monomers, while the average degree of polymerization reaches 50 in the box, with a maximum average degree reaching up to 75 in the simulation box.

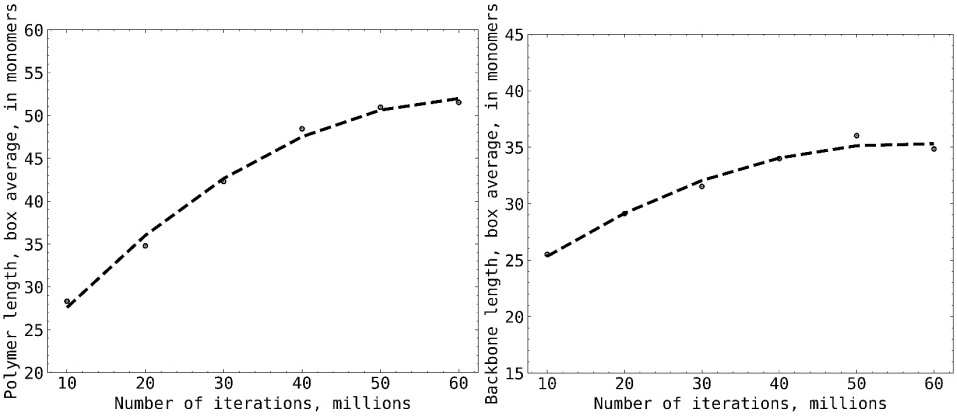

Fig. 38. Left – plot depicts evolution of averaged MAA polymer backbone length (in MAA monomers) during simulation. Right – plot depicts evolution of averaged MAA polymer length (in MAA monomers) during simulation

Statistical analysis of MAA polymers growth from our Monte Carlo simulations is presented in **Fig. 39.** The combined results of the 70 box simulation statistics: (a) and (c) subplots.

Results show that MAA polymer growth continues up to 50 million Monte Carlo steps, and MAA polymer growth becomes equilibrated with branched MAA polymers degradation process. The equilibrium between these two processes leads to a stable MAA polymers structure at the simulation box scale.

However, on a finer scale, the polymer's structure remains rapidly evolving and directly depends on the instantaneous balance between MAA polymer creation and disintegration processes. The evolution of the MAA degree of polymerization indicates the stabilization of these polymer parameters at 50 million Monte Carlo steps. The statistical convergence of the growth trends in MAA polymers is evident, as increasing the number of simulation boxes from 70 to 420 does not alter the outcomes.

In this study, the MC simulations conducted aim to simulate the initial phases of polymerization of MAA. As a result, the MC model employed in this research excludes the later stages of chemical transformation where "relatively small" MAA polymers transition into larger structures. The focus of our MC simulations is on the growth of MAA polymers, with an average degree of polymerization ranging from 40 to 75 monomers.

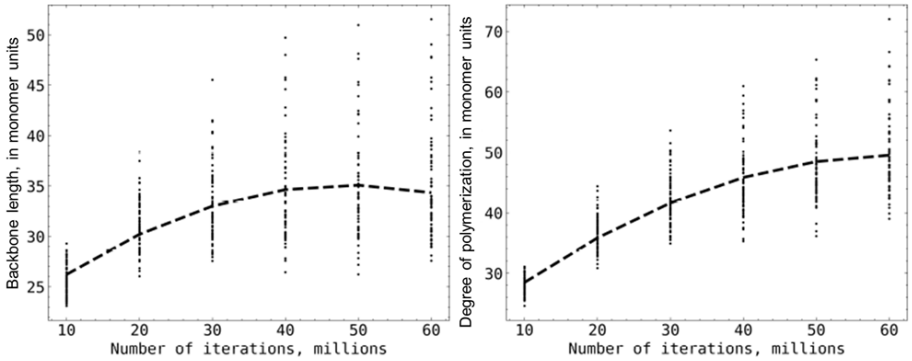

(a) Evolution of the average backbone length (b) Evolution of the average degree of polymerization

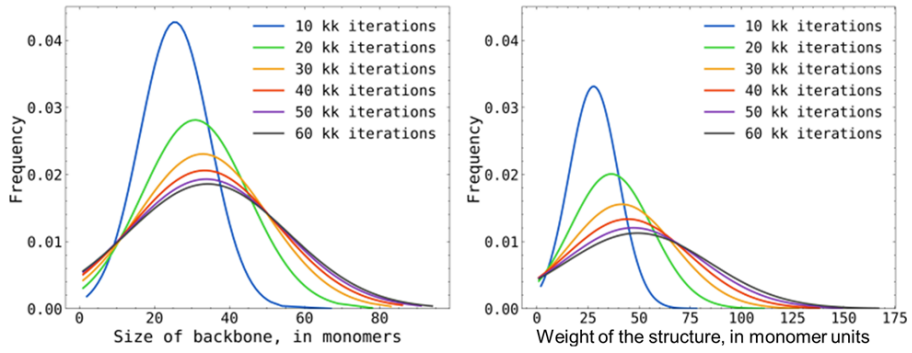

(c) Distribution of backbone lengths (d) Distribution of molecular weight

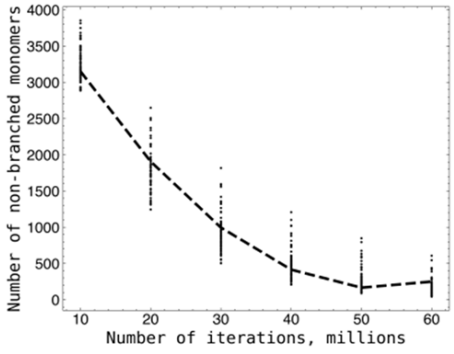

(e) Evolution of the proportion of unbranched monomer units

Fig. 39. The combined results of the 70 box simulation statistics: (a) and (c) subplots shows the evolution and distribution of the average backbone length in monomer units; (b) and (d) subplot shows the evolution and distribution of the average degree of polymerization; (e) subplot shows the fraction of monomers remaining in linear, non-branched configurations

Although this study doesn't include hands-on experiments, it shows a kind of similarity with certain situations found in PLP studies, especially those dealing with

MAA polymerization[269,270]. It's important to remember that these similarities aren't solid proof, but more like hints of a connection under specific conditions. This comparison, though not a perfect match, suggests that the sizes of the formed chains we estimated in our model seem reasonable, adding experimental support to the reliability of our theoretical approach.

4.5.7. Uncertainty analysis

These MC simulations possess the capability to generate distinct growth patterns of MAA polymers in each simulation box, enabling us to examine the variability in the process of MAA polymer growth, including rare instances of growth events. However, it is crucial to assess the resemblance between the MAA polymer growth patterns across different simulation boxes to comprehend the primary trends in polymer growth and identify the predominant chemical processes that contribute to the formation of polymers under γ-irradiation. With this in mind, we conducted a similarity analysis of the acquired MAA polymer structures at various stages of the MC simulation.

The Jaccard index is a similarity statistic that compares the size of the intersection of the two sets to the size of their union to determine their similarity. It was used to quantify uncertainty in MC simulations by comparing the sets of outputs obtained by different simulation runs and quantify the level of unpredictability in the simulation results by providing a measure of consistency or resemblance between the sets. A higher Jaccard index value implies that the sets are more comparable and so have a lower level of uncertainty, whereas a lower Jaccard index value suggests that the sets are less similar. Each of 420 boxes has been compared against each other and the Jaccard index has been calculated.

Fig. 40 shows that the Jaccard index and maps of the simulation outcome confirm consistent results while capturing the expected degree of variability in polymer growth through randomness in the MC method. After 20 million iterations, the similarity between boxes remains high enough, indicating that the parameters and conditions used in the simulation are such that the results are consistent across multiple runs, regardless of the random sampling used in the MC method. However, as the simulation continues, the similarity decreases as expected, as more complex structures are formed through the occurrence of increasingly complex combination events with lower probabilities, ultimately leading to a higher variability in the final state of the box.

Within the context of MC simulations, a Jaccard similarity index approximating 0.5 is indeed indicative of a well-functioning model. A high Jaccard index would suggest a deficiency in the intrinsic randomness expected of MC simulations, pointing to a possible malfunction in the stochastic engine. Conversely, an excessively low index might signify overly dissimilar data sets, implying an absence of any significant, non-random patterns. Consequently, maintaining a moderate Jaccard similarity index testifies to the model's robust ability to balance exploratory and exploitative search within the solution space. Expanding the Jaccard similarity analysis from 70 to 420 simulation boxes shows minimal alterations in the similarity indexes between the

simulation boxes. Therefore, these findings suggest that our MC simulation is statistically convergent and accurately captures the primary growth pattern of MAA polymers in our model.

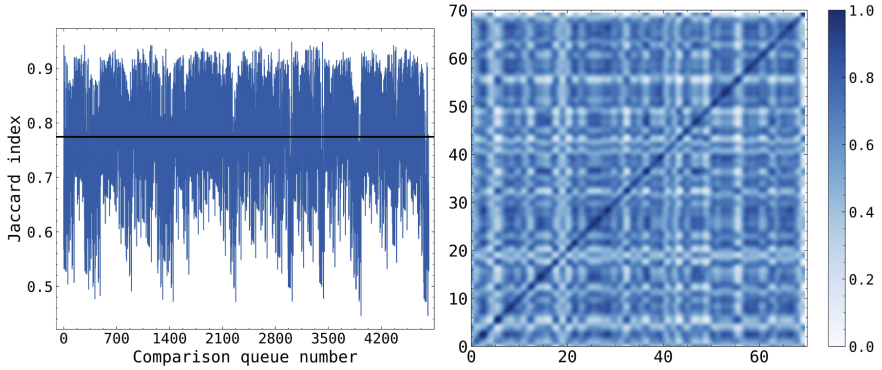

(**a**) Jaccard index at 20 million iterations (**b**) Jaccard map at 20 million iterations

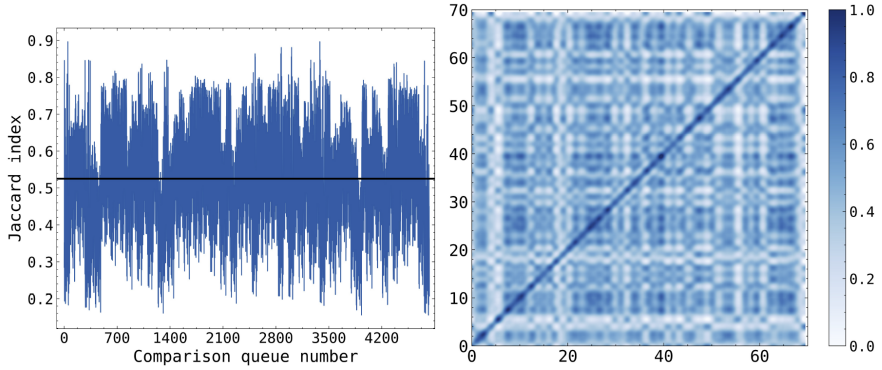

(**c**) Jaccard index at 40 million iterations (**d**) Jaccard map at 40 million iterations

Fig. 40. Jaccard similarity index distributions and maps at different simulation phases

5. CONCLUSIONS

1. The close similarity between the results obtained from the simulation setup and the experimental setup demonstrates a high level of resemblance, affirming the applicability of simulations for analyzing dose patterns in complex cases. A comparison between experimental measurements and FLUKA model results showed minor discrepancies of up to 5.4%, attributable to simulation geometry and uncertainties in implant modeling and radiochromic film positioning.

2. A software tool developed in-house, employing gamma index evaluation, facilitates a quantitative comparison of various dosimetry methods in orthovoltage X-ray therapy. In the experimental setup, the calculated passing rates, referred to as the 2D dose difference index, for RTQA2 radiochromic film were determined to be 87% and 90% for EBT3 radiochromic film, respectively. These findings suggest that the chosen standard criteria of 3% / 3 mm were excessively stringent for kilovoltage radiotherapy, resulting in notable disparities between experimental and simulation outcomes. However, upon adjusting the criteria values to 6% / 6 mm, the closest resemblance between experimental and simulation results was observed for films irradiated from the side. Specifically, the estimated passing rates for EBT3 films were 99.31%, while for RTQA2 films it was 97.68%. Conversely, for the other two irradiation geometries, both film types exhibited passing rates below the threshold of 95.00%. Notably, irradiation geometries involving metal artifacts yielded the least favorable results.

3. The development of a novel Monte Carlo model aimed at investigating the dynamics of radiation-induced polymer growth. Each Monte Carlo simulation involved 60 million random walk steps within the chemical events space, replicating the growth methacrylic acid polymers under a constant gamma radiation flux. Across all 420 simulations, we observed the formation of intricate branched polymers, with smaller branched polymers aggregating to form larger clusters of methacrylic acid polymers. The average length of the polymer backbone reached approximately 35 monomers, exhibiting fluctuations between 25 and 50. The average degree of polymerization reached around 50, with fluctuations ranging from 38 to 72. The results correlate well with the experimental works of other researchers. The fraction of monomers remaining in linear, non-branched configurations was found to be less than 10% after the converge of the simulation box. The Jaccard similarity index demonstrated high consistency, with a value of 0.9 in the early stages of the simulation, gradually decreasing to 0.4 towards the final stages. This indicates the effectiveness and controllable uncertainty of the model in capturing the polymer growth dynamics.

6. SANTRAUKA

6.1. Įvadas

6.1.1. Aktualumas

Mažos energijos rentgeno terapija, kuriai naudojama 100–400 kiloelektronvoltų spinduliuotė, plačiai taikoma spindulinės onkologijos srityje. Dėl ribotos skvarbos ši terapija dažniausiai skirta gydyti paviršiniams navikams ir galvos bei kaklo vėžiniams dariniams, siekiant apsaugoti sveikuosius audinius ir kritinius organus nuo nepageidaujamos apšvitos [1].

Vienas iš pagrindinių iššūkių mažos energijos rentgeno terapijoje yra patikimų dozės planavimo sistemų trūkumas. Tikslus dozės suplanavimas yra svarbus siekiant optimizuoti gydymą, tinkamai apšvitinti naviką ir sumažinti žalą sveikiems audiniams. Tai ypač aktualu sudėtingais, komplikuotais atvejais, pacientui turint didelio tankio implantų netoli planuojamo gydyti ligos židinio. Didelio tankio svetimkūniai trikdo spinduliuotės sklidimą ir sukelia iškraipymus, susidaro apšvitos nehomogeniškumas ir neapibrėžtumas.

Monte Karlo spinduliuotės pernašos simuliacijos yra vienas iš pagrindinių dozės planavimo įrankių spindulinėje terapijoje, kuris įgalina tiksliai modeliuoti ir prognozuoti apšvitos sukeltos dozės pasiskirstymą. Šiuo modeliavimo metodu galima įvertinti medžiagų savybes, geometriją ir spinduliuotės pernašos procesus, todėl suteikiama vertingų įžvalgų apie didelio tankio implantų įtaką dozės iškraipymams, ir šis metodas gali būti pritaikomas individualiai paciento anatomijai.

Monte Karlo modeliavimo lyginimas su eksperimentiniais duomenimis suteikia galimybę dar labiau mažinti dozės planavimo neapibrėžtį. Eksperimentinis patikrinimas padeda verifikuoti ir tobulinti modeliavimo modelius, padidina jų tikslumą ir patikimumą. Vienas iš dažniausiai taikomų eksperimentinio tikrinimo metodų yra saviryškių (radiochrominių) plėvelių naudojimas. Šias plėveles sudaro radiochrominė medžiaga, kurios optinis tankis keičiasi proporcingai pagal sugertą spinduliuotės dozę. Įdėjus tokias plėveles į individualizuotą, paciento anatomiją atkartojantį modelį, galima išmatuoti dozės pasiskirstymą ir palyginti jį su modeliavimo rezultatais. Toks eksperimentinis būdas leidžia turėti nepriklausomą nuo modeliavimo dozės pasiskirstymo planą ir įvertinti Monte Karlo simuliacijos rezultatų tikslumą.

Polimerinių gelių dozimetrai leidžia atlikti dozės vertinimą trimatėje erdvėje. Šie dozimetrai pagaminti iš spinduliuotei jautrių polimerinių medžiagų, kurių fizikinės savybės, tokios kaip spalva ar optinis tankis, keičiasi veikiant apšvitai. Gelių dozimetrus galima suformuoti taip, kad jie atkartotų sudėtingas anatomines struktūras ir suteiktų trimatę informaciją apie dozės pasiskirstymą jose. Eksperimentinė patikra naudojant tokius dozimetrus užtikrina papildomą nepriklausomą dozės pasiskirstymo verifikaciją ir leidžia palyginti gautus rezultatus su Monte Karlo simuliacijų rezultatais.

Apdorojant skirtingais metodais gautus rezultatus, svarbu turėti tinkamą metodologiją šių rezultatų tinkamam kiekybiniam palyginimui. Vienas iš plačiai taikomų dozės pasiskirstymo palyginimo metodų yra gama indekso skaičiavimai. Šis

rodiklis parodo kiekybiškai išmatuotų ar simuliuotų dozės pasiskirstymų atitikimus, įtraukdamas ir dozių dydžių skirtumą, ir dozių geometrinių taškų atitikimo kriterijus. Gama indekso skaičiavimai leidžia kiekybiškai įvertinti modeliuojamų ir eksperimentinių dozių pasiskirstymų atitikimą. Praktiniam jo panaudojimui turi būti sukurtas specializuotas programinis įrankis, pritaikytas skaičiuoti specifiniams palyginimo metodams, šiuo atveju – tarp skaitmeninių simuliacijos rezultatų ir fizinės saviryškės plėvelės bei dozimetrinių gelių.

Polimerinių gelių dozimetrai yra vienintelis eksperimentinis metodas, leidžiantis užfiksuoti spinduliuotės lauką trimatėje erdvėje. Kitaip nei tradiciniai dozimetrai, kurie matuoja dozę taške arba plokštumoje, polimeriniai gelių dozimetrai suteikia išsamią erdvinę informaciją apie sugertąją dozę dominančiame tūryje ir leidžia tiksliai verifikuoti sudėtingus gydymo planus. Vienas iš pagrindinių iššūkių gaminant tinkamos sudėties polimerinius gelio dozimetrus yra sudėtingi radikalų inicijuotos polimerizacijos procesai. Sugertoji dozė apšvitos metu sukelia momentinę monomerų polimerizaciją, todėl gelio fizikinės savybės kinta. Tikslus šių mechanizmų suvokimas yra būtinas norint tiksliai interpretuoti apšvitinto polimerinio gelio rezultatus.

Radikalų inicijuotos polimerizacijos mechanizmams analizuoti taikomi įvairūs modeliai. Polimerizacijos, vykstančios apšvitos poveikio sąlygomis, tyrimų bei kurtų modelių yra sąlygiškai nedaug, ir jie daugiausia apsiriboja kinetiniais modeliais [2]. Didžiausi iššūkiai kyla dėl sudėtingo radikalų inicijuotos polimerizacijos mechanizmo ir kinetikos, susidedančios iš sudėtingų daugiapakopių cheminių reakcijų [3]. Polimerų inžinerijoje Monte Karlo modeliavimas leidžia modeliuoti įvairias polimerų charakteristikas, pavyzdžiui, grandinės ilgį, šakojimąsi [4].

Šiame darbe pateikiamas novatoriškas Monte Karlo metodu grįstas modelis, kuriame simuliuojama kelių tūkstančių metakrilo rūgšties monomerų polimerizacija veikiant spinduliuotei, o pradiniai parametrai gaunami iš kvantinės chemijos skaičiavimų. Toliau pristatomas Monte Karlo modelis tinka simuliuoti įvairiems radikalų inicijuotos polimerizacijos scenarijams.

6.1.2. Darbo tikslas

Šio darbo tikslas – ištirti mažos energijos rentgeno terapijos dozės pasiskirstymą sudėtingos geometrijos heterogeninėse terpėse naudojant polimerinius dozimetrus ir taikant Monte Karlo modeliavimą. Daugiausia dėmesio skiriama Monte Karlo skaičiavimo modelio, skirto apšvitos sukeltos polimerizacijos dinamikai įvertinti, kūrimui.

6.1.3. Darbo uždaviniai

1. Išnagrinėti mažos energijos rentgeno spinduliuotės dozės pasiskirstymą esant sudėtingam švitinimo scenarijui ir palyginti modeliavimo rezultatus su eksperimentiniais rezultatais, gautais naudojant polimerines medžiagas.

2. Sukurti ir eksperimentiškai verifikuoti programinį įrankį, skirtą dvimačiams gama indekso skaičiavimams mažos energijos rentgeno spindulių terapijoje, esant sudėtingiems dozės pasiskirstymams dėl didelio tankio artefaktų buvimo švitinimo lauke.

3. Sukurti ir ištirti Monte Karlo metodu pagrįstą kompiuterinį modelį, skirtą spinduliuotės inicijuotai dozimetrinių gelių polimerizacijai simuliuoti ir tirti juose vykstančiams struktūriniams pokyčiams.

6.1.4. Ginamieji teiginiai

1. Monte Karlo spinduliuotės pernašos modeliavimas, taikant sukurtą trimatį fantomą, leidžia sumažinti dozės neapibrėžtį heterogeninėje terpėje, esant didelio tankio artefaktams, mažos energijos rentgeno spinduliuotės terapijos metu.

2. Gama indekso apskaičiavimo principu pagrįstas programinis įrankis leidžia kiekybiškai palyginti skirtingus dozimetrijos metodus mažos energijos rentgeno terapijoje.

3. Pasiūlytas novatoriškas Monte Karlo modelis, skirtas spinduliuotės inicijuotos polimerizacijos dinamikai vertinti, leidžia kiekybiškai įvertinti radikalų inicijuotos polimerizacijos procesus.

6.1.5. Mokslinis naujumas

Pirmojoje šio darbo dalyje dėmesys skiriamas Monte Karlo spinduliuotės pernašos modeliavimo galimybėms sprendžiant problemas, su kuriomis susiduriama mažos energijos rentgeno spinduliuotės terapijos srityje. Nors metalinių implantų poveikis didelės energijos spindulių terapijai tiriamas jau kurį laiką, šiame tyrime pirmą kartą, naudojant FLUKA Monte Karlo modeliavimo paketą ir trimačius (3D) išspausdintus modelius, analizuojami dantų implantų sukeliami dozės neatitikimai mažos energijos rentgeno spindulių terapijos metu [A1]. Siūlomas metodas gali padidinti gydymo veiksmingumą ir pacientų saugumą geriau įvertinant didelio tankio implantų poveikį dozės iškraipymams.

Pristatoma specializuota programinė priemonė, skirta kiekybiškai palyginti skirtingus dozimetrijos metodus mažos energijos rentgeno spindulių terapijoje. Ji leidžia simuliuojamus modelius palyginti su eksperimentiniais metodais gautais rezultatais [A2]. Ši papildoma verifikavimo priemonė yra reikalinga sudėtingose situacijose, esant didelio tankio artefaktams terapijos srityse, ir gali padėti geriau įvertinti metalinių implantų sąlygojamą dozės pasiskirstymo neapibrėžtį mažos energijos rentgeno spindulių terapijoje.

Sukurtas naujo tipo Monte Karlo modelis, naudojantis kvantinės chemijos modelių rezultatus, ir leidžiantis simuliuoti supaprastintą dozimetriniams geliams naudojamų medžiagų polimerizacijos procesą veikiant išorinei spinduliuotei [A3]. Modelis buvo įgyvendintas vartojant C++ programavimo kalbą ir pritaikytas didelio našumo skaičiavimo klasteriams. Jis leidžia vizualizuoti tikėtinas polimerų struktūras trimatėje erdvėje, nagrinėja susidarančių polimerų grandinių kiekybinį vertinimą ir

geba vizualiai pateikti prognozuojamas polimerines struktūras. Modelis gali būti vertinga priemonė siekiant kurti naujus dozimetrinius gelius, pasižyminčius pageidaujamomis savybėmis.

6.1.6. Metodika

Fotonų ir elektronų pernašai modeliuoti buvo naudojama populiari Monte Karlo modeliavimo programa FLUKA. Dėl savo universalumo FLUKA yra pagrindinis CERN naudojamas Monte Karlo programinis paketas.

Eksperimentiniuose tyrimuose naudotos saviryškės radiochrominės EBT3 ir RTQA2 plėvelės.

Naudotą PMMA fantomą pagamino Severina Paukštytė Kauno onkologijos ligoninėje. Trimačiu (3D) spausdintuvu išspausdintą fantomą, panaudotą eksperimentinėje sąrankoje, sukūrė Benas Gabrielis Urbonavičius ir Ieva Masiulytė Kauno technologijos universitete.

Apšvitos procedūras rentgeno spindulių terapijos aparatu GULMAY D3225 atliko Jurgita Laurikaitienė Kauno onkologijos ligoninėje.

Kvantinės chemijos skaičiavimus, kurių rezultatai buvo naudojami kaip įvesties duomenys kurtam polimerizacijos modeliui, atliko Žilvinas Rinkevičius (Karališkasis technologijų institutas, Švedija). Jis taip pat buvo pagrindinis polimerizacijos modelio konsultantas.

6.1.7. Autoriaus indėlis

Autorius sukūrė visus programinius įrankius, kodus ir modelius, taip pat atliko visus modeliavimo ir simuliacijos darbus.

FLUKA modeliavimai atlikti Kauno technologijos universitete (Lietuva), polimerizacijos modelio simuliacijos vyko naudojant KTH Karališkojo technologijų instituto (Švedija) išteklius.

6.1.8. Rezultatų aprobavimas

Pagrindiniai disertacijos rezultatai paskelbti penkiuose moksliniuose leidiniuose: trys su disertacijos tema susiję straipsniai paskelbti žurnaluose, įtrauktuose į *Clarivate Analytics Web of Science* duomenų bazę, ir du straipsniai paskelbti konferencijų pranešimuose, įtrauktuose į *CA WoS* duomenų bazę. A. Ševčik buvo visų *CA WoS* publikacijų pirmasis autorius.

Dar penki įvairūs konferencijų straipsniai, santraukos ir stendiniai pranešimai buvo pristatyti tarptautinėse konferencijose.

6.1.9. Disertacijos struktūra

Disertaciją sudaro penki skyriai. Pirmajame skyriuje pristatomas darbo tikslas ir uždaviniai, autoriaus indėlis, aprobavimas, darbo aktualumas ir naujumas. Antrajame pateikiama literatūros apžvalga apie Monte Karlo modeliavimą, esamus modelių kodus bei jų sistemą ir tokių modeliavimų taikymą. Trečiajame skyriuje aprašytos priemonės ir metodika, pateikiamos naudotos eksperimentinės priemonės, medžiagos, taip pat naudojami skaičiavimo ištekliai. Ketvirtasis skyrius skirtas rezultatams ir jų interpretacijai. Disertacija baigiama paskutiniu penktuoju skyriumi, kuriame pateikiama rezultatų santrauka ir išvados. Darbo pabaigoje yra literatūros sąrašas, priedai, mokslinių publikacijų sąrašas ir žurnaluose publikuotų straipsnių sąrašas.

Bendra disertacijos apimtis – 148 puslapiai, sudarantys apie 8 autorinius lankus, 50 paveikslų, 9 lentelės, 271 literatūros šaltinis.

6.2. MK simuliacijų taikymas sudėtingiems klinikiniams scenarijams

Saviryškės (radiochrominės) plėvelės – tai polimeriniai dozimetrai, kurie keičia spalvą veikiant jonizuojančiajai spinduliuotei. Šių plėvelių pagrindą sudaro spinduliuotei jautrus monomeras, įterptas į polimerinę matricą ir susluoksniuotas tarp poliesterio sluoksnių. Spinduliuotės sukeltos diacetileninių molekulių polimerizacijos metu susidaro polidiacetileninių dažiklių polimerai, dėl kurių plėvelėse vyksta spalvinimo procesas. Tam tikros atsako charakteristikos gali priklausyti nuo daugelio veiksnių, įskaitant plėvelės modelį, partijos numerį, cheminę sudėtį, sluoksnių konfigūraciją ir sugerties spektrus. Be to, gali būti svarbios spinduliuotės savybės, susijusios su dalelių tipu (fotonai, elektronai, protonai) ir energija (MeV, keV). Šviesos šaltinio tipas ir jautrumas tam tikram bangos ilgio diapazonui, plėvelės orientacija skeneryje, skenavimo spalvos gylis, skenavimo tipas, skenerio stiklo temperatūra ir plėvelės padėtis skeneryje – visa tai gali turėti įtakos plėvelės nuskaitymui. Įtakos gali turėti ir laikas, praėjęs nuo apšvitos iki nuskaitymo, dar vadinamas nuskaitymo laiku.

Eksperimentams naudotos saviryškės EBT3 ir RTQA2 tipo plėvelės. Saviryškės EBT3 plėvelės paprastai naudojamos kaip dozimetrai radioterapijos kokybės užtikrinimui, o saviryškės RTQA2 plėvelės skirtos daugiausia greitintuvų dozėms registruoti. Tačiau šios plėvelės taip pat gali būti naudojamos mažos energijos rentgeno spinduliuotės kokybės užtikrinimo patikroms. Plėvelių aktyviojo sluoksnio elementinė sudėtis yra ta pati, skiriasi tik apsauginių sluoksnių struktūra. Todėl yra rekomenduojamas skirtingas skenavimo tipas kiekvienai plėvelei: EBT3 plėvelę galima tiksliau nuskaityti taikant transmisinį skenavimą, o štai RTQA2 plėvelė turi nepermatomą pagrindo medžiagą, todėl ją nuskaitant turėtų būti taikomas reflektinis skenavimo tipas. Remiantis Palmerio [240] ir Butsono [241] pateiktais duomenimis, plėvelės buvo modeliuojamos atsižvelgiant į abiejų tipų plėvelių konstrukciją, o modelio elementinė sudėtis pateikta 8 lentelėje.

8 lentelė. Saviryškių plėvelių cheminė sudėtis

Sluoksnio tipas	Tankis (g/cm^3)	Elementinė sudėtis, atominės masės %								
		H	**Li**	**C**	**N**	**O**	**Na**	**Al**	**S**	**Cl**
Aktyvusis	1,20	56,5	0,6	27,4	0,3	13,3	0,1	1,6	0,1	0,1
Tarpinis	1,27	50,0	–	33,0	–	17,0	–	–	–	–
Pagrindas	1,35	36,4	–	45,5	–	18,2	–	–	–	–

Monte Karlo metodas taikomas spinduliuotės pernašos lygtims spręsti, kai kiti analitiniai, spektriniai ar kitokie skaičiavimai yra netinkami. Šis metodas leidžia efektyviai nagrinėti įvairius spinduliuotės laukus ir geometriją, dažnai būdamas vieninteliu tinkamu sprendimo būdu spinduliuotės pernašos uždaviniams spręsti.

Europos branduolinių tyrimų organizacijoje (CERN) sukurta FLUKA (*FLUktuierende KAskade*) [249] – tai Monte Karlo modeliavimo programa, plačiai naudojama dalelių, įskaitant fotonus, elektronus ir protonus, pernašai modeliuoti. Ja galima modeliuoti įvairius fizikinius reiškinius, įskaitant dalelių sąveiką, energijos perdavimą ir dozės sugertį. Programa naudojama įvairiose srityse, įskaitant dalelių fiziką, branduolinę inžineriją ir medicinos fiziką. FLUKA leidžia pasiekti itin tikslių rezultatų ir yra verifikuota pagal įvairius eksperimentinius duomenis. Šiame darbe ji buvo naudojama kaip pagrindinė spinduliuotės dalelių pernašos modeliavimo priemonė.

Didelio tankio objektai, pavyzdžiui, metaliniai implantai, gali turėti didelės įtakos dozės pasiskirstymui radioterapijos metu. Dėl to gydomiems audiniams gali būti skiriama per maža arba per didelė dozė, todėl gali sumažėti gydymo veiksmingumas ir padidėti šalutinio poveikio rizika. Tyrime, kuriame buvo nagrinėjamas didelio tankio objektų poveikis dozės pasiskirstymui, naudojant Geant4/GATE buvo imituojamas gydymas ortopediniais implantais, tokiais kaip titano ir PEEK (polieterio eterketono) implantai. Šio tyrimas įrodė, kad palei titano implantų ribas susidarė dideli dozės gradientai, o PEEK implantai tokių gradientų neturėjo. Buvo nustatyta, kad dozė, gaunama į titano implantų vidines ertmes, buvo 10–15 % didesnė nei planuota. Tai parodė, kad didelio tankio objektai gali žymiai pakeisti dozės pasiskirstymą anatominėje srityje.

Dantų implantai taip pat sukelia iškraipymus taikant spindulinę terapiją galvos ir kaklo srityje. Šie implantai sukelia trikdžius, kurie nepageidaujamai paveikia spinduliuotės pasiskirstymą. Serap [132] tyrimu siekta įvertinti titaninių dantų implantų poveikį didelės energijos rentgeno ir gama spindulių dozės pasiskirstymui pacientams, sergantiems galvos ir kaklo vėžiu, taikant Monte Karlo modeliavimą. Nustatyta, kad dėl implantų poveikio dozės pasiskirstymas išsikreipia ir vyksta didelė spinduliuotės sklaida kauliniame audinyje, kuris tiesiogiai liečiasi su implantu. Šios išvados rodo, kad terapeutai, planuodami spindulinį gydymą, turėtų atsižvelgti į pacientų implantus, siekdami sumažinti osteoradionekrozės riziką. Sarigul [133] savo tyrimui taikė Monte Karlo modeliavimą ir išnagrinėjo apšvitos lauko dydžio įtaką procentinei gylio dozei heterogeninėje terpėje. Rezultatai parodė, kad, kai metalinės medžiagos buvo patalpintos į vandens modelį, iš karto prieš pat metalo paviršių sparčiai didėjo dozė, o už metalinių medžiagų esančiai dozei įtakos turėjo lauko dydis.

Tai rodo, kad būtina atsižvelgti į didesnio tankio kūnus pacientų anatomijoje, taikant spindulinę terapiją, idant būtų sumažinta šalutinių poveikių rizika ir užtikrintas optimalus onkologinis gydymas.

FLUKA simuliacinis paketas buvo naudojamas analizuojant mažos energijos rentgeno spinduliuotės energijos perdavimo modelius ir dozių pasiskirstymus apšvitintame trimačiu (3D) spausdintuvu išspausdintame antropomorfiniame galvos ir kaklo modelyje su integruotu metaliniu artefaktu (metalinis dantis apatiniame žandikaulyje) (41 pav.). Svarbu pabrėžti, kad modeliavimų metu pateikiama visa trimatės erdvės informacija apie dozės pasiskirstymą; tačiau, siekiant palyginti su apšvitintų EBT2 plėvelių dozės pasiskirstymu, modeliavimo rezultatai pateikiami kaip plokštuminiai vaizdai.

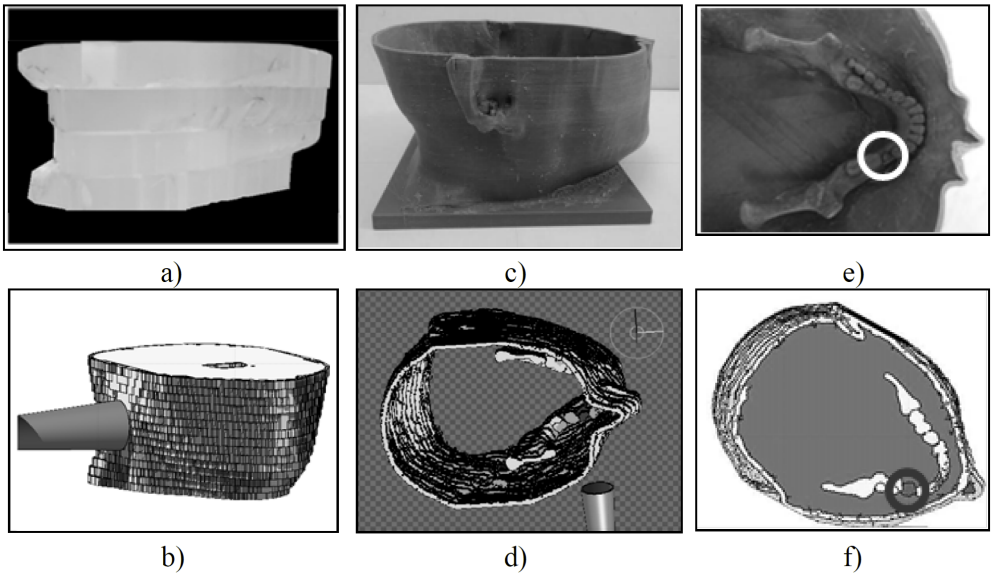

41 pav. Fantomai dozės pasiskirstymui įvertinti: a) PMMA plokštės fantomas; b) simuliuotas plokštės fantomas; c) trimačiu (3D) spausdintuvu išspausdintas antropomorfinis fantomas, rekonstruotas iš tikro paciento kompiuterinės tomografijos vaizdų; d) simuliuotas antropomorfinio fantomo modelis; e) trimačiu (3D) spausdintuvu išspausdinto fantomo, vaizduojančio apatinio žandikaulio su dantimis vietą ir nurodančio metalinį artefaktą viduje, skersinis vaizdas; f) simuliuoto vandeniu užpildyto fantomo skersinis vaizdas, nurodantis metalinio danties vietą jame (šaltinis: [A1])

Rezultatų analizė patvirtino ankstesnių autorių tvirtinimus, kad dozės pasiskirstymas esant metaliniam implantui yra sudėtingesnis ir komplikuotesnis, palyginti su dozės pasiskirstymu modelyje be metalinio implanto. Galima interpretuoti, kad didesnio tankio kūne vyksta intensyvesnė energijos sugertis, lyginant su biologiniu audiniu; dėl šios priežasties susidaro antriniai elektronai, papildomai iškreipiantys galutinį dozės pasiskirstymo vaizdą.

Monte Karlo modeliavimas buvo palygintas su eksperimentiniais rezultatais, gautais vertinant energijos pasiskirstymo modelius apšvitintose EBT2 plėvelėse.

Nustatyta, kad eksperimentiniai ir sumodeliuoti dozės pasiskirstymai yra ekvivalentūs. FLUKA kodo taikymas leidžia papildomai įvertinti dozės pasiskirstymą trimatėje erdvėje, esant neheterogeniškai aplinkai su didesnio tankio artefaktais.

Apšvitintos EBT2 plėvelės rezultatai pateikti 42 pav. ir atitinka eksperimentinių matavimų, atliekamų kaip kokybės užtikrinimo programos dalis, rezultatus. Apskaičiuota, kad didžiausias 4 Gy dozės, gautos veikiant rentgeno spindulių generatoriui, kurio įtampa 80 kVp, įsiskverbimo gylis yra 6 mm. Eksperimentų metu skvarbos gylis buvo įvertintas kaip 6–7 mm, o tai rodo tik nedidelį netikslumą ir įrodo, kad FLUKA modeliavimą galima taikyti matuojant plokštuminį dozės pasiskirstymą. Didžiausią įtaką nurodytam netikslumui turėjo dozės vertinimo metodas saviryškėse plėvelėse.

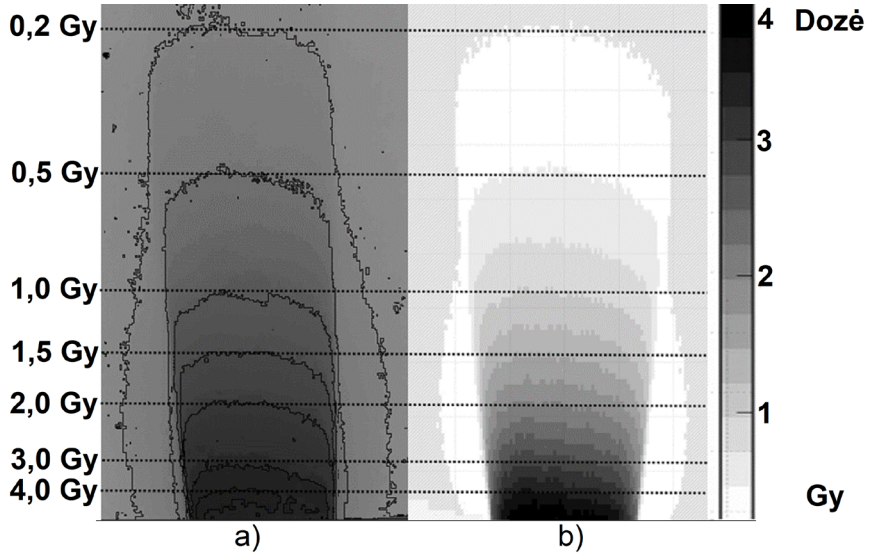

42 pav. Dvimatis (2D) dozės pasiskirstymas toje pačioje švitinamo PMMA plokštės fantomo skersinėje plokštumoje: a) – EBT2 plėvelė F2, įvertinta taikant Image J2 kodą; b) – FLUKA modeliavimas [A1]

Siekiant nustatyti, ar FLUKA modeliavimas gali būti patikimas dozės planui patikrinti, buvo atlikti bandomieji ir modeliavimo eksperimentai su antropomorfiniu fantomu, turinčiu viduje integruotą metalinį artefaktą. Kaip matyti 43 pav., didelių neatitikimų tarp eksperimentinių EBT2 plėvelės matavimų ir FLUKA modelio rezultatų nebuvo. Išmatuotos dozės nuokrypis tarp eksperimentinių ir modeliavimo rezultatų siekė iki 5,4 %. Gauti rezultatai panašiai koreliuoja su kitų autorių panašių darbų rezultatais (iki 5,1 %) [62, 266].

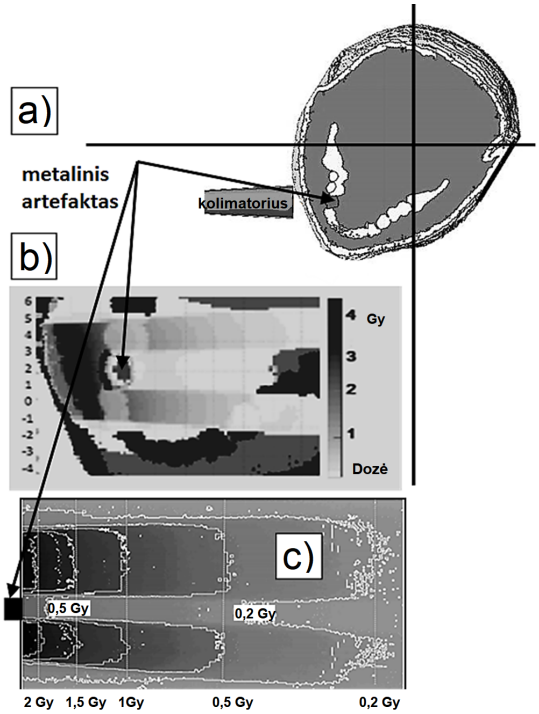

43 pav. Dvimatis (2D) dozės pasiskirstymas skersinėje plokštumoje apšvitintame fantome su viduje integruotais metaliniais artefaktais: a) dominanti sritis FLUKA modeliuotame fantome; b) FLUKA modeliuojamos dozės pasiskirstymas; c) dozės pasiskirstymas ant EBT2 plėvelės, stebimas iškart už metalinio artefakto vandeniu užpildytame švitinamame antropomorfiniame fantome (a), b) ir c) masteliai skiriasi) [A1]

6.3. Gama indekso taikymas simuliacijos ir saviryškių plėvelių palyginimui

Harms [242] pasiūlė matematinį metodą, skirtą kiekybiniam dozės pasiskirstymo, gauto taikant du skirtingus dozimetrijos metodus, įvertinimui. Šis vertinimas grindžiamas dviejų parametrų taikymu vienu metu: atstumo iki taškų geometrinio nesutapimo (DTA) ir procentinio dozių skirtumo (DD). DTA apibrėžiamas kaip trumpiausias atstumas tarp etaloninės dozės taško ir to paties dozės taško lyginamame dozės pasiskirstyme. Jis taikomas kaip rodiklis, rodantis, kaip gerai abu pasiskirstymai yra suderinti. Procentinis dozių skirtumas DD apibrėžiamas kaip procentinis dozių skirtumas, jei abu pasiskirstymai yra geometriškai tame pačiame taške. Nustačius DD ir DTA priimtinumo kriterijus, galima bendrai įvertinti dviejų lyginamų dozės pasiskirstymų sutapimą. Low [271] pateikė gama vertinimo metodą (gama indekso analizę), kuris leido du kintamuosius – DD ir DTA – suvesti į vieną parametrą.

Naudojant šio darbo metu sukurtą programinį įrankį galima įvertinti dvimatį (2D) dozės ir atstumo indeksą (2DDI), tiksliai pavaizduojant dvimačio (2D) dozės

pasiskirstymo duomenis, gautus iš kelių šaltinių. Palyginus MC modeliavimo duomenis su eksperimentiniais duomenimis, surinktais vertinant saviryškes plėveles, kodas buvo pritaikytas 2DDI pasiskirstymo žemėlapiams sudaryti. Buvo nustatyti 3 % / 3 mm tikslumo reikalavimai DD ir DTA atžvilgiu, kurie įprastai taikomi klinikinėje praktikoje atliekant spindulinio gydymo procedūrų kokybės kontrolę (44 pav.). Eksperimentai ir modeliavimas buvo atliekami pagal geometrines schemas, pavaizduotas 45 pav. Geriausiai eksperimentinių ir modeliuojamų dozių verčių panašumas buvo nustatytas tose plėvelėse, kurios buvo apšvitintos iš šono, kai rentgeno spindulių pluošto ašis yra lygiagreti su PMMA plokštės paviršiumi. RTQA2 plėvelės apskaičiuotas 2DDI praeinamumo lygis buvo atitinkamai 87 % ir 90 % EBT3 paveikslėliui. Šios vertės buvo mažesnės už 95 % praeinamumo rodiklį, kuris buvo nustatytas kaip minimali ribinė vertė didelės energijos spindulinėje terapijoje, siekiant užtikrinti didelį gydymo tikslumą ir sėkmingumą. Vertinimo rezultatai atskleidė, jog pasirinkti standartiniai 3 % / 3 mm kriterijai buvo per griežti, kad juos būtų galima taikyti mažos energijos radioterapijai dėl palyginti didelių eksperimentinių ir modeliavimo rezultatų skirtumų.

Kriterijų reikšmės buvo padidintos (6 % / 6 mm), siekiant pamatuoti vertinimo kriterijų taikymo apribojimus mažos energijos terapijoje. Abiejų plėvelių bendro praeinamumo skaičiavimai pateikti 9 lentelėje.

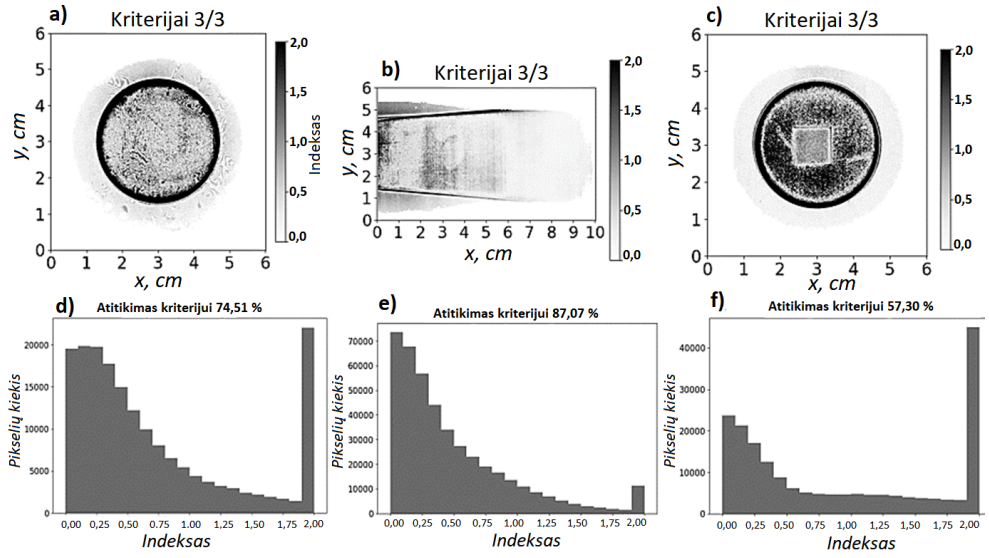

44 pav. 2DDI skaičiavimų taikymas RTQA saviryškės plėvelės ir Monte Karlo modelio rezultatų palyginimui pagal 3 % dozių skirtumo ir 3 mm atstumo atitikimo kriterijus: a) b) c) kriterijų vizualusis atitikmuo skirtingose geometrijose d) e) f) atitikimų kriterijui histogramos skirtingose geometrijose [A2]

9 lentelė. Palyginimo suvestinė

Plėvelė	Kriterijai	Indekso palyginimo vertės		
		Geometrija nr. 1	Geometrija nr. 2	Geometrija nr. 3
EBT3	3 % / 3 mm	80,62 %	90,82 %	60,15 %
RTQA2	3 % / 3 mm	74,51 %	87,07 %	57,30 %
EBT3	6 % / 6 mm	91,34 %	99,31 %	86,77 %
RTQA2	6 % / 6 mm	88,48 %	97,68 %	77,93 %

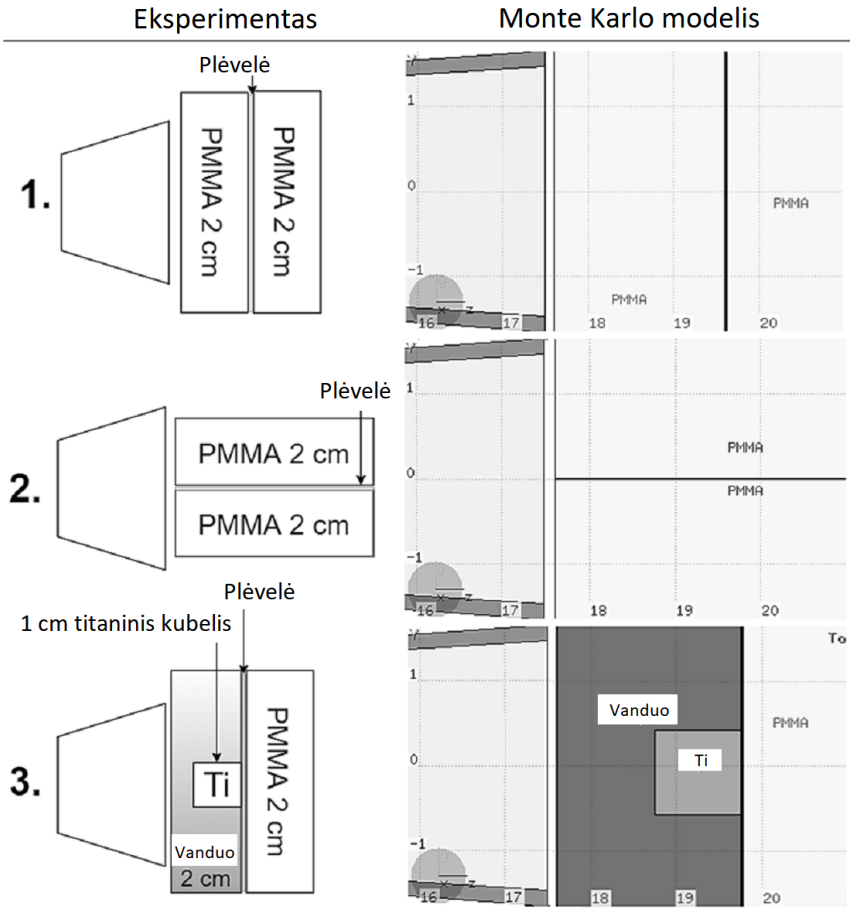

45 pav. Eksperimentams taikytos geometrijos [A2]

6.4. Metakrilo rūgšties polimerizacijos veikiant apšvitai MK modelis

Šiame darbe pristatėme Monte Karlo modelį, skirtą spinduliuotės sukeltai metakrilo rūgšties (MAA) monomerų polimerizacijai vandeniniame tirpale modeliuoti taikant Monte Karlo metodą. Kinetiniai modeliai dažniausiai neatspindi viso polimerų augimo mechanizmo sudėtingumo, ir naudoja statistinius vidurkius aprašant MAA polimerų struktūras. Mūsų taikytas modelio algoritmas (5 pav.) siekia ištirti spinduliuotės sukeltos MAA polimerizacijos vandeniniame tirpale mikrostruktūrą ir augimo dėsningumus, siekiant optimizuoti poli(metakrilo rūgšties) hidrogelių, tinkamų geliniams dozimetrams, sintezę.

Polimerų augimas spinduliuotės metu gali būti aprašytas tikimybiškai. Norint simuliuoti šį procesą, inicijuojama norimo dydžio modeliavimo dėžė, į kurią kartu su pradine konfigūracija įdedama tam tikros koncentracijos dominanti medžiaga. Tada Monte Karlo ciklas pradedamas pagal nustatytą algoritmą (46 pav.). Per kiekvieną ciklo iteraciją modelio dėžės ribose pasirenkama atsitiktinė vieta, kad būtų imituojama atsitiktinio radikalo atsiradimo galimybė. Tada patikrinama, ar tam tikru atstumu yra dominanti molekulė, kurią paveiktų radikalas. Jei tokia molekulė egzistuoja, atliekamas radiacinės žalos ir sugerties koeficiento skaičiavimas, kurio metu nustatoma galima jungimosi arba skilimo įvykių seka, pagrįsta šiais energijos skaičiavimais.

Vertinami trys atvejai: (1) molekulinė struktūra pasikeičia po sėkmingo sujungimo įvykio, (2) molekulinė struktūra pasikeičia po sėkmingo skilimo įvykio arba (3) struktūra lieka nepakitusi, jei nė vienas iš šių įvykių nebuvo sėkmingas. Visais atvejais kitame etape apskaičiuojamas inertinis struktūros pasisukimas ir lokacijos pakeitimas. Galiausiai atliekamas baigiamasis galimybių patikrinimas, kurio metu vertinama, ar įvykę pakeitimai fiziškai įmanomi, t. y. ar nėra nepriimtino modeliuojamų kūnų susikirtimo. Pagal galimybių patikros rezultatus, atlikti pakeitimai išsaugomi arba atmetami.

Monte Karlo modeliavimas itin priklauso nuo pseudoatsitiktinių skaičių generatorių (RNG). Tai algoritmai, taikomi nenuspėjamai skaičių sekai generuoti. *Intel Math Kernel Collection* (*Intel MKL*) *299* – viena populiariausių mokslinių matematinių paprogramių bibliotekų. Šiame projekte taikomas vektorinio tipo *Mersenne Twister* pseudoatsitiktinių skaičių generatorius (MT19937) iš MKL, siekiant užtikrinti vienodus diskrečiųjų imčių pasiskirstymus.

Metakrilo rūgšties ($C_4H_6O_2$) molekulė buvo geometriškai aproksimuota kaip šešiakampis, kurio matmenys 5 Å × 5 Å × 2 Å. Ryšio kampas lygus 109,5°, kuris atitinka anglies atomų ryšio kampus. Sukimosi bei judėjimo įvykis apskaičiuojamas pagal atitinkamos struktūros inercijos momentą, ir objektas pasukamas bei pastumiamas išilgai *x*, *y* bei *z* ašių atsitiktine tvarka. Didžiausias leistinas atstumas yra 30 Å.

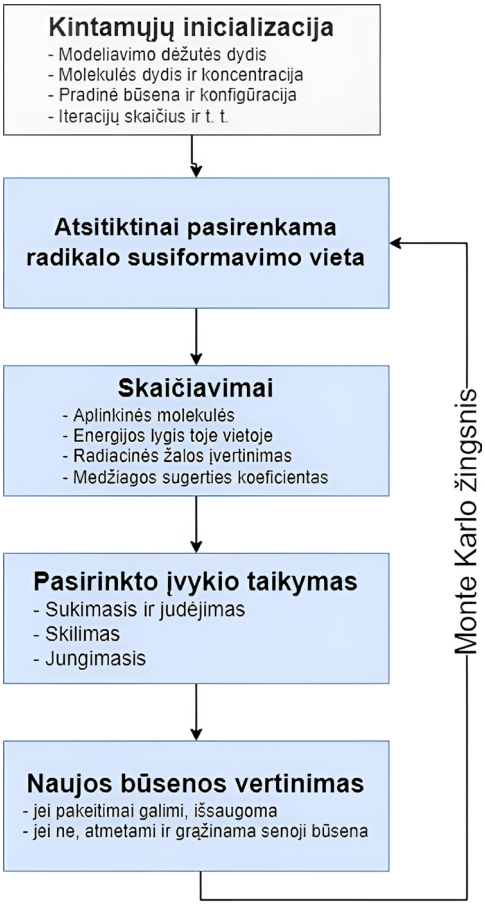

46 pav. Polimerų augimo modelio įgyvendinimo schema [A3]

Skilimo procesas pasirinktą struktūrą atitinkamame taške segmentuoja į naujus atskirus objektus. Jungimosi procesas įgyvendina galimus struktūrų sujungimo scenarijus, kai aktyvintoji molekulė yra tam tikru atstumu nuo kitų aplinkinių kūnų. Tikslaus jungimo scenarijaus pasirinkimas priklauso nuo dominančių struktūrų konfigūracijos, vietos ir dydžio. Objektai gali jungtis tarpusavyje sudarydami naujus didesnius darinius. Kai abu arba vienas iš objektų yra nedidelis arba kai aktyvavimo taškas yra netoli polimero galų, trumpesnis objektas prisijungia prie ilgesnio, ir šitaip grandinė padidėja. Jeigu tai didesnės, sudėtingos, šakotos struktūros, susijungimas aktyvavimo taške gali sukurti visiškai naują struktūrinį darinį. Kitais atvejais objektas gali tapti kitos struktūros atšaka, sudarydamas šakotą darinį. Objekto dydis ir aktyvavimo taškas lemia, ar susijungimo metu atsiras viena šaka, ar aktyvavimo taške objektas bus suskaidytas į dvi atšakas. Kiti jungimosi scenarijai apima sudėtingus mainymosi procesus, kai aktyvintosios struktūros gali skilti tam tikrose vietose ir prisijungti prie kito suskilusio darinio dalies, taip sukurdamos naujais ryšiais ir santykiais susijusius objektus.

Galimybių patikrą sudaro netinkamų susidūrimų nustatymas, ir ji reikalinga RNG generuojamų fiziškai neįmanomų atvejų kontrolei bei atmetimui. Susidūrimų nustatymas – tai dviejų ar daugiau objektų susikirtimo aptikimo skaičiavimo problema. Tai matematiškai itin sudėtinga sritis, turinti įvairių sprendimų. Pasirinktai molekulės aproksimacijai reikia sudėtingesnio metodo, kuris turi būti kuo veiksmingesnis dėl didelio kuboidų ir iteracijų skaičiaus. Šiame darbe nuspręsta taikyti Gilberto–Džonsono–Kerčio (Gilbert-Johnson-Keerthi, GJK) atstumo skaičiavimo metodą, kuriuo apskaičiuojamas trumpiausias atstumas tarp dviejų išgaubtųjų aibių.

Metakrilo rūgšties monomero cheminės aktyvacijos (ryšio) tikimybė $Pact(U)$ apskaičiuojama pagal lygtį

$$Pact(U) = X\big((1 - F) + F * \mathrm{erf}(G * U)\big) \qquad \text{(25 lygtis)}$$

Metakrilo rūgšties monomero cheminio suardymo (skilimo) tikimybė $Pbrk(U)$ apskaičiuojama pagal lygtį

$$Pbrk(U) = X\big((1 - F) + F * \mathrm{erf}(G * U^2\big) \qquad \text{(26 lygtis)}$$

Jose išvesti nedimensiniai parametrai (*fitting*) *X, F, G* buvo gauti atlikus MAA polimerų susidarymo ir skilimo cheminių reakcijų energijų skaičiavimus, o *U* žymi lokalios reakcijos energijos dydį. Duomenys cheminės aktyvacijos ir skilimo tikimybių skaičiavimams paimti iš kvantinės chemijos skaičiavimo modelio, kuriame molekulės elektroninė struktūra prognozuojama taikant hibridinį B3LYP mainų–koreliacijos funkcionalą ir def2-SVPD bazių rinkinį.

Modeliavimo trukmė priklauso nuo formuojamų struktūrų sudėtingumo ir kinta nuo 1,3 val. milijonui iteracijų iki 1,9 val. milijonui iteracijų 50 nm × 50 nm × 50 nm dydžio simuliacinei dėžutei, turinčiai 5875 molekules. Modeliuojant 30 nm × 30 nm × 30 nm dydžio dėžutes gaunami cheminiu požiūriu neįmanomi rezultatai; tokie rezultatai rodo, kad dėžutės dydis nebeturi įtakos rezultatams tik pasiekus 40 nm × 40 nm × 40 nm dydį.

Siekiant įvertinti sukurtų struktūrų atsitiktinumą, simuliavimo dėžutė buvo padalinta į 125 mažesnes 10 nm × 10 nm × 10 nm × 10 nm dydžio dėžutes. Kiekvienos mažesnės dėžutės monomerų kiekis buvo suskaičiuotas ir palygintas su monomerų kiekiu, apskaičiuotu analogiškam kubeliui kitose dėžutėse. Iš viso tokiu būdu buvo ištirta 10 numatyto dydžio dėžučių struktūrinių panašumų. Nustatytas 51,9 vidutinis nuokrypis rodo, kad skirtingose dėžutėse pagamintos struktūros tarpusavyje nesusijusios (47 pav.). Tai patvirtina, kad pasirinkto RNG generuojamų skaičių kokybė yra tinkama.

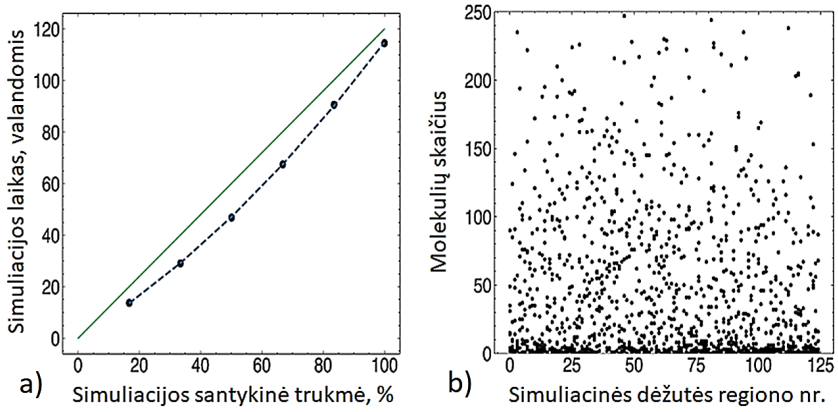

47 pav. a) Modeliavimo greitis 50 nm × 50 nm × 50 nm dėžutėje su numatytąja koncentracija (5875 molekulės) svyruoja nuo 1,3 val. milijonui iteracijų modeliavimo pradžioje iki 1,9 val. milijonui iteracijų. b) Dėžutės struktūros atsitiktinumo įvertinimas pagal monomerų skaičių mažesniuose dėžutės plotuose.

Kiekvienoje simuliacinėje dėžutėje buvo atlikta 60 mln. iteracijų cheminių įvykių erdvėje, siekiant imituoti MAA polimerų augimą esant homogeniškam pastovios gama spinduliuotės srautui. Visais 420 atvejų stebėtas sudėtingų šakotų MAA polimerų susidarymas. Tipiškas MAA polimerų augimo vizualusis modelis pavaizduotas 48 pav., kuriame pradinis MAA polimerų aglomeracijos centrų susidarymas stebimas jau po 10 mln. žingsnių. Polimerų konsolidacija tęsiasi iki 50 mln. žingsnių, tada pasiekiama palyginti stabili MAA polimerų aglomeracija. Pasiektas polimerizacijos laipsnio vidurkis dėžutėje siekia 40–60.

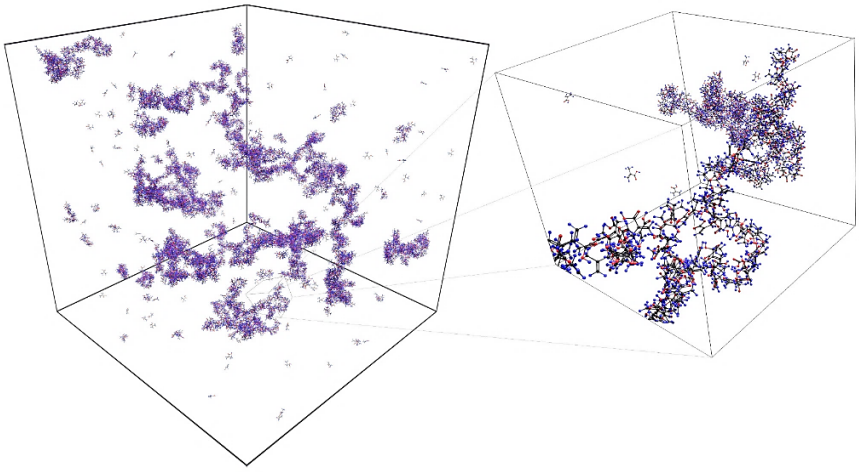

48 pav. Vizualusis polimerizacijos modelio vaizdavimas

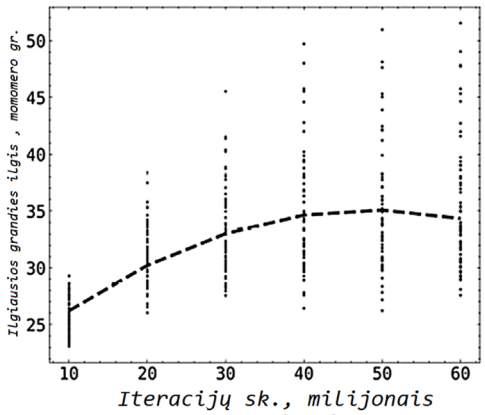

(a) Ilgiausios grandinės polimere dinamika

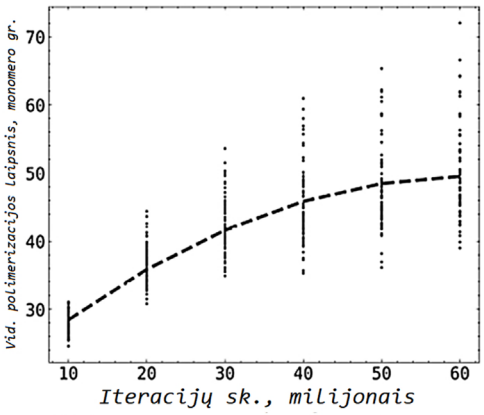

(b) Polimerizacijos laipsnio dinamika

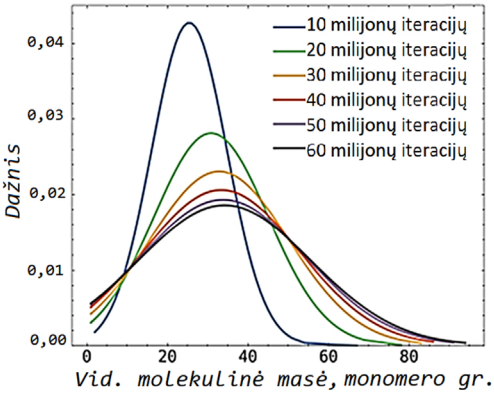

(c) Ilgiausios grandinės pasiskirstymas

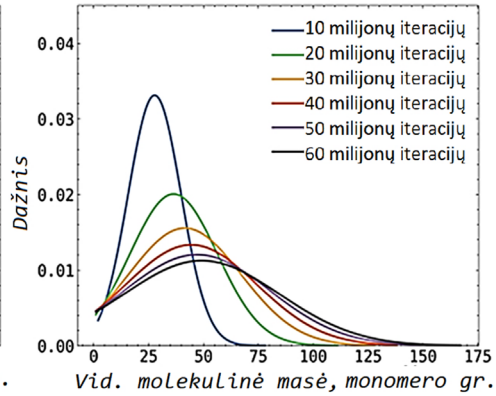

(d) Vid. molek. masės pasiskirstymas

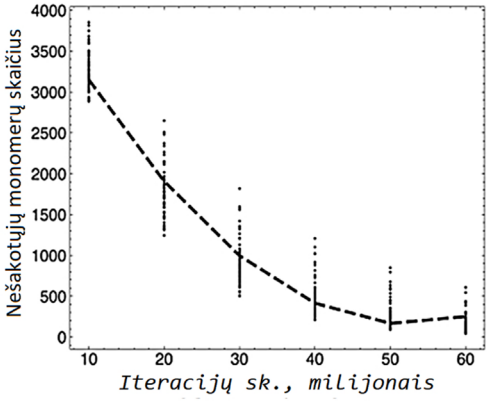

(e) Nešakotųjų monomerų dalis

49 pav. Polimerų augimo modeliavimo rezultatai

MAA polimerų augimo statistinė analizė pateikiama 49 pav., jame galima įvertinti konversiją, polidispersiją ir polimerizacijos laipsnį. Matoma, kad polimerų augimas tęsiasi iki 50 mln. žingsnių, vėliau augimas susilygina su irimo procesu, pasiekiama konversija >90 %. Šių dviejų procesų pusiausvyra lemia stabilią MAA polimerų struktūrą simuliacinėje dėžutėje. Pasiekiamas vidutinis polimerizacijos laipsnis siekia 50–60 [monomerų grandžių]. Šis rezultatas gerai koreliuoja su eksperimentiniais darbais lazeriu indukuojant radikalų inicijuotą polimerizaciją metakrilo rūgščiai [269, 270].

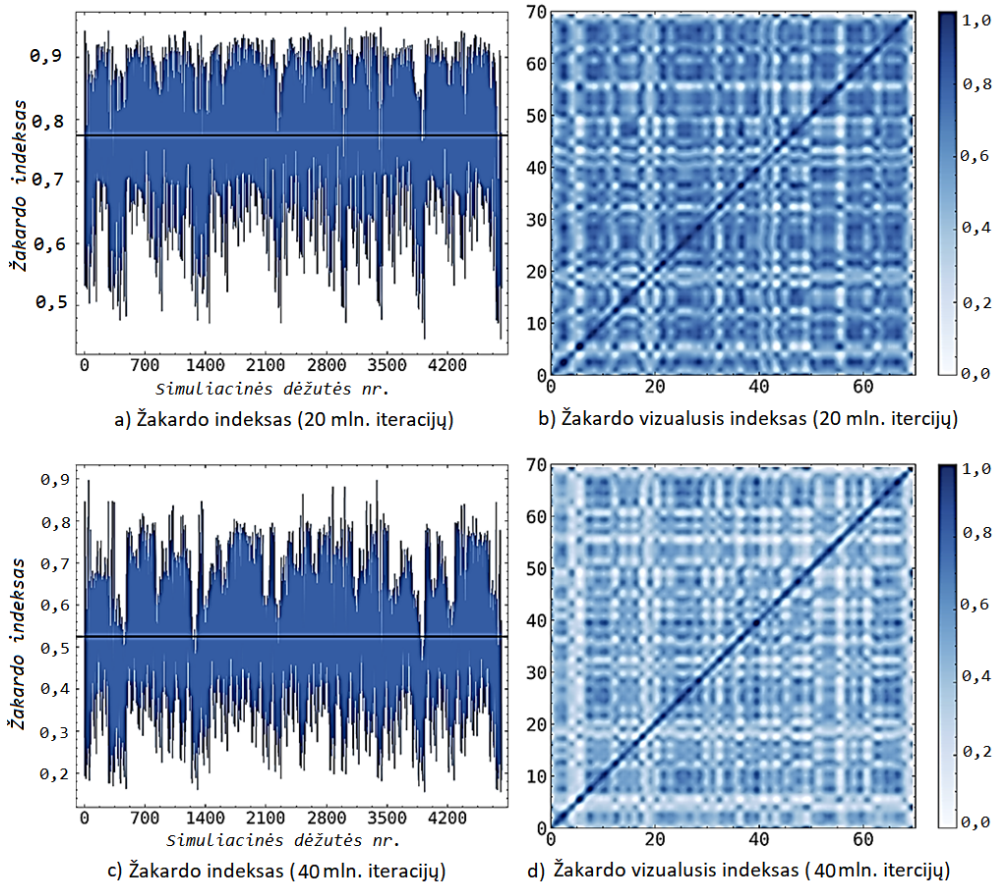

50 pav. Žakardo panašumo indekso rezultatai

Taikant Monte Karlo modelius būtina įvertinti modelio statistinę neapibrėžtį (*A* tipo neapibrėžtis). Žakardo (Jaccard) indeksas – tai panašumo skaičiavimas, pagal kurį dviejų rinkinių susikirtimo dydis lyginamas su jų sąjungos dydžiu, siekiant nustatyti jų panašumą. Jis buvo taikomas šiame disertaciniame darbe Monte Karlo modeliavimo neapibrėžtumui kiekybiškai įvertinti, lyginant visus 420 simuliacinių dėžučių rezultatus. Šiuo indeksu kiekybiškai įvertintas rezultatų nenuspėjamumo lygis, pateikiant rinkinių panašumo skaitines vertes. Didesnė Žakardo indekso vertė

reiškia, kad rinkiniai yra panašesni, todėl jų neapibrėžtumo lygis mažesnis, o mažesnė Žakardo indekso vertė rodo, kad rinkiniai yra mažiau panašūs.

Iš 50 pav. matyti, kad Žakardo indeksas ir indekso žemėlapiai patvirtina nuoseklius rezultatus ir kartu atspindi tikėtiną polimerų augimo kintamumo laipsnį. Po 10 mln. ir 20 mln. iteracijų panašumas išlieka pakankamai didelis, o tai rodo, jog modeliavimo metu taikyti parametrai yra tokie, kad rezultatai nuoseklūs visose nepriklausomose simuliacijose, nepriklausomai nuo atsitiktinės imties. Tačiau iteracijų skaičiui vis didėjant, modeliavimo rezultatų panašumas, kaip ir tikėtasi, mažėja, nes sudėtingesnės struktūros susidaro dėl vis sudėtingesnių jungimosi įvykių su mažesnėmis tikimybėmis, o tai galiausiai lemia didesnę galutinės dėžutės būsenos neapibrėžtį. Svarbu pabrėžti, kad visų simuliacijų iteracijų kintamumo perėjimai yra itin nuoseklūs.

Modeliuojant Monte Karlo metodu Žakardo panašumo indeksas, svyruojantis nuo 0,4 iki 0,5, iš tiesų rodo gerai veikiantį modelį. Per didelis indeksas rodytų, kad Monte Karlo modeliavimams reikalingas atsitiktinumas yra nepakankamas, o tai rodytų prastą RNG veikimą. Pernelyg mažas indeksas reikštų pernelyg skirtingus duomenų rinkinius, tai verstų manyti, kad nesusidaro statistiškai reikšmingų neatsitiktinių modelių.

6.5. Išvados

1. Monte Karlo spinduliuotės pernašos modeliavimas taikant sukurtą virtualųjį modelį (fantomą) stipriai koreliuoja su eksperimentiniu būdu gautais rezultatais. Tai patvirtina tokio modeliavimo pritaikomumą analizuojant dozės pasiskirstymą ir padeda sumažinti dozės neapibrėžtį esant didelio tankio artefaktams mažos energijos rentgeno spinduliuotės terapijos metu. Lyginant eksperimentinių matavimų ir FLUKA modelio rezultatus, nustatyti nedideli (iki 5,4 %) neatitikimai, kuriuos lėmė modeliavimo geometrijos netikslumai ir implantų modeliavimo bei saviryškės plėvelės padėties nustatymo neapibrėžtumai.

2. Sukurta gama indekso skaičiavimais pagrįsta programinė priemonė, leidžianti kiekybiškai palyginti skirtingus dozimetrijos metodus mažos energijos rentgeno terapijoje. Lyginant simuliacijos rezultatus su eksperimentu, apskaičiuotas dvimatis (2D) dozių skirtumo indeksas (2DDI) RTQA2 plėvelei buvo 87 %, o EBT3 plėvelei – 90 % taikant 3 % / 3 mm kriterijus. Pakoregavus kriterijų vertes iki 6 % / 6 mm, didžiausias panašumas tarp eksperimentinių ir modeliavimo rezultatų buvo pastebėtas šonu apšvitintoms plėvelėms – apskaičiuotas EBT3 plėvelių praeinamumo rodiklis buvo 99,31 %, o RTQA2 plėvelių – 97,68 %.

3. Sukurtas kvantinės chemijos simuliacijų rezultatus naudojantis Monte Karlo modelis, skirtas tirti spinduliuotės sukelto MAA polimerų augimo dinamikai. Įrankis padeda įvertinti dozimetriniuose įrankiuose naudojamų medžiagų polimerizacijos mechanizmus. Iš viso atlikta 420 simuliacijų po 60 mln. iteracijų, atkartojant MAA polimerų augimą esant pastoviai dozės galiai. Simuliacijų rezultatai rodo, kad

apšvitos metu susiformuoja sudėtingi šakoti MAA polimerai, kurie jungiasi į didesnius klasterius. Vidutinis polimerizacijos laipsnis siekė apie 50 monomerų grandžių, mažiausias laipsnis – 38, didžiausias – 72. Simuliacijos pabaigoje vidutiniškai simuliacinėje dėžutėje nešakotųjų monomerų dalis siekė < 0,1. Rezultatai koreliuoja su eksperimentiniais kitų autorių darbais, tiriant MAA radikalinę polimerizaciją.

REFERENCES

[1] Alfouzan AF. Radiation therapy in head and neck cancer. Saudi Med J 2021;42:247.

[2] Fierens SK, Van Steenberge PHM, Reyniers M-F, D'hooge DR, Marin GB. Analytical and advanced kinetic models for characterization of chain-growth copolymerization: the state-of-the-art. React Chem Eng 2018;3:128–45.

[3] Brandao ALT, Soares JBP, Pinto JC, Alberton AL. When polymer reaction engineers play dice: applications of Monte Carlo models in PRE. Macromol React Eng 2015;9:141–85.

[4] Meimaroglou D, Kiparissides C. Review of Monte Carlo methods for the prediction of distributed molecular and morphological polymer properties. Ind Eng Chem Res 2014;53:8963–79.

[5] Morin RL. Monte Carlo Simulation in the Radiological Sciences. CRC Press; 2019. doi:10.1201/9780429277085.

[6] Krim DE, Bakari D, Zerfaoui M, Rrhioua A, Oulhouq Y. Monte Carlo evaluation of particle interactions within the patient-dependent part of Elekta 6 MV photon beam applying IAEA phase space data. Reports Pract Oncol Radiother 2021;26:928–38. doi:10.5603/RPOR.a2021.0111.

[7] Kling A, Barao FJC, Nakagawa M, Tavora L, Vaz P. Advanced Monte Carlo for Radiation Physics, Particle Transport Simulation and Applications: Proceedings of the Monte Carlo 2000 Conference, Lisbon, 23–26 October 2000. Springer Science & Business Media; 2014.

[8] Peraud J-PM, Landon CD, Hadjiconstantinou NG. Monte Carlo Methods for Solving the Boltzmann Transport Equation. Annu Rev Heat Transf 2014;17:205–65. doi:10.1615/annualrevheattransfer.2014007381.

[9] Bielajew AF. Fundamentals of the Monte Carlo method for neutral and charged particle transport. Sci York 2000;1.

[10] Rubinstein RY, Kroese DP. Simulation and the Monte Carlo method. John Wiley & Sons; 2016.

[11] Fano U, McVoy KW, Albers JR. Sauter theory of the photoelectric effect. Phys Rev 1959;116:1147–56. doi:10.1103/PhysRev.116.1147.

[12] Hubbell JH. Review of photon interaction cross section data in the medical and biological context. Phys Med Biol 1999;44:1–22. doi:10.1088/0031-9155/44/1/001.

[13] Koch HW, Motz JW. Bremsstrahlung cross-section formulas and related data. Rev Mod Phys 1959;31:920–55. doi:10.1103/RevModPhys.31.920.

[14] Tsai YS. Pair production and bremsstrahlung of charged leptons. Rev Mod Phys 1974;46:815–51. doi:10.1103/RevModPhys.46.815.

[15] Heitler W. The Quantum Theory of Radiation. Oxford, At the Clarendon Press 1954.

[16] Berger MJ, Coursey JS, Zucker MA, Chang J. Stopping-Power and Range Tables for Electrons, Protons, and Helium Ions | NIST. NIST Stand Ref Database 124 1998.

[17] Brice DK. Stopping powers for electrons and positrons (ICRU report 37; International commission on radiation units and measurements, Bethesda, Maryland, USA, 1984). Nucl Instruments Methods Phys Res Sect B Beam Interact with Mater Atoms 1985;12:187–8. doi:10.1016/0168-583x(85)90718-9.

[18] Berger MJ, Coursey JS, Zucker MA, Chang J. ESTAR, PSTAR, and ASTAR: Computer Programs for Calculating Stopping-Power and Range Tables for Electrons, Protons, and Helium Ions (version 1.2.3). Natl Inst Stand Technol 2005.

[19] Kawrakow I, Rogers DWO, Mainegra-Hing E, Tessier F, Townson RW, Walters BRB. EGSnrc toolkit for Monte Carlo simulation of ionizing radiation transport 2000.

[20] Kawrakow I, Mainegra-Hing E, Tessier F, Walters B. The EGSnrc C++ class library. Technical Report No. PIRS–898 (rev A). NRC Rep PIRS-898 (Rev A) 2009.

[21] Agostinelli S, Allison J, Amako K, Apostolakis J, Araujo H, Arce P, et al. Geant4—a simulation toolkit. Nucl Instruments Methods Phys Res Sect A Accel Spectrometers, Detect Assoc Equip 2003;506:250–303. doi:10.1016/S0168-9002(03)01368-8.

[22] Allison J, Amako K, Apostolakis J, Araujo H, Dubois PA, Asai M, et al. Geant4 developments and applications. IEEE Trans Nucl Sci 2006;53:270–8. doi:10.1109/TNS.2006.869826.

[23] Allison J, Amako K, Apostolakis J, Arce P, Asai M, Aso T, et al. Recent developments in Geant4. Nucl Instruments Methods Phys Res Sect A Accel Spectrometers, Detect Assoc Equip 2016;835:186–225. doi:10.1016/J.NIMA.2016.06.125.

[24] Incerti S, Kyriakou I, Bernal MA, Bordage MC, Francis Z, Guatelli S, et al. Geant4-DNA example applications for track structure simulations in liquid water: A report from the Geant4-DNA Project. Med Phys 2018;45:e722–39. doi:10.1002/MP.13048.

[25] Incerti S, Baldacchino G, Bernal M, Capra R, Champion C, Francis Z, et al. THE Geant4-DNA project. Int J Model Simulation, Sci Comput 2010;1:157–78. doi:10.1142/S1793962310000122.

[26] Incerti S, Ivanchenko A, Karamitros M, Mantero A, Moretto P, Tran HN, et al. Comparison of GEANT4 very low energy cross section models with experimental data in water. Med Phys 2010;37:4692–708. doi:10.1118/1.3476457.

[27] Bernal MA, Bordage MC, Brown JMC, Davídková M, Delage E, El Bitar Z, et al. Track structure modeling in liquid water: A review of the Geant4-DNA very low energy extension of the Geant4 Monte Carlo simulation toolkit. Phys Medica 2015;31:861–74. doi:10.1016/J.EJMP.2015.10.087.

[28] Battistoni G, Cerutti F, Chin W, Esposito LS, Fassò A, Ferrari A, et al. Overview of the FLUKA code. Ann Nucl Energy 2015;82:10–8. doi:10.1016/j.anucene.2014.11.007.

[29] Fassò A, Ferrari A, Roesler S, Ranft J, Sala PR, Battistoni G, et al. The FLUKA code: present applications and future developments. Comput High Energy Nucl Phys 2003:24–8.
[30] Böhlen TT, Cerutti F, Chin MPW, Fassò A, Ferrari A, Ortega PG, et al. The FLUKA Code: Developments and Challenges for High Energy and Medical Applications 2014. doi:10.1016/j.nds.2014.07.049.
[31] Ballarini F, Battistoni G, Brugger M, Campanella M, Trovati S, Sommerer F, et al. The physics of the FLUKA code: Recent developments. Adv Sp Res 2007;40:1339–49. doi:10.1016/j.asr.2007.05.031.
[32] Salvat F, Fern M. PENELOPE – A Code System for Monte Carlo Simulation of Electron and Photon Transport. Nucl Energy Agency 2015.
[33] Werner CJ, Bull JS, Solomon CJ, Brown FB, McKinney GW, Rising ME, et al. MCNP6. 2 Release Notes—report LA-UR-18-20808. Los Alamos Natl Lab 2018:43.
[34] Werner CJ, Bull JS, Solomon CJ, Brown FB, McKinney GW, Rising ME, et al. MCNP6. 2 release notes. Los Alamos Natl Lab 2018.
[35] Fang Q, Yan S. MCX Cloud—a modern, scalable, high-performance and in-browser Monte Carlo simulation platform with cloud computing. J Biomed Opt 2022;27. doi:10.1117/1.JBO.27.8.083008.
[36] Yan S, Jacques SL, Ramella-Roman JC, Fang Q. Graphics-processing-unit-accelerated Monte Carlo simulation of polarized light in complex three-dimensional media. J Biomed Opt 2022;27. doi:10.1117/1.JBO.27.8.083015.
[37] Monte Carlo eXtreme: GPU-based Monte Carlo Simulations: Citation n.d. http://mcx.space/wiki/?Citation (accessed December 17, 2022).
[38] Iwase H, Niita K, Nakamura T. Development of General-Purpose Particle and Heavy Ion Transport Monte Carlo Code. Http://DxDoiOrg/101080/1881124820029715305 2012;39:1142–51. doi:10.1080/18811248.2002.9715305.
[39] Sato T, Iwamoto Y, Hashimoto S, Ogawa T, Furuta T, Abe S ichiro, et al. Features of Particle and Heavy Ion Transport code System (PHITS) version 3.02. J Nucl Sci Technol 2018;55:684–90. doi:10.1080/00223131.2017.1419890.
[40] PHITS. PHITS Homepage 2018:1–2. https://phits.jaea.go.jp (accessed December 17, 2022).
[41] Ogawa T, Hirata Y, Matsuya Y, Kai T. Development and validation of proton track-structure model applicable to arbitrary materials. Sci Rep 2021;11. doi:10.1038/S41598-021-01822-1.
[42] Jan S, Santin G, Strul D, Staelens S, Assié K, Autret D, et al. GATE: a simulation toolkit for PET and SPECT. Phys Med Biol 2004;49:4543–61. doi:10.1088/0031-9155/49/19/007.
[43] Wilson JW, Slaba TC, Badavi FF, Reddell BD, Bahadori AA. 3DHZETRN: Neutron leakage in finite objects. Life Sci Sp Res 2015;7:27–38.
[44] Wilson JW, Slaba TC, Badavi FF, Reddell BD, Bahadori AA. 3DHZETRN: shielded ICRU spherical phantom. Life Sci Sp Res 2015;4:46–61.

[45] Wilson JW, Slaba TC, Badavi FF, Reddell BD, Bahadori AA. Advances in NASA radiation transport research: 3DHZETRN. Life Sci Sp Res 2014;2:6–22.
[46] RITRACKS: A software for simulation of stochastic radiation track structure, micro- and nano-dosimetry, radiation chemistry and DNA damage by heavy ions(MSC-25937-1) | NASA Software Catalog n.d. https://software.nasa.gov/software/MSC-25937-1 (accessed December 17, 2022).
[47] Andreo P. Monte Carlo simulations in radiotherapy dosimetry. Radiat Oncol 2018;13:1–15. doi:10.1186/s13014-018-1065-3.
[48] Baumann K-S, Kaupa S, Bach C, Engenhart-Cabillic R, Zink K. Monte Carlo calculation of perturbation correction factors for air-filled ionization chambers in clinical proton beams using TOPAS/GEANT. Z Med Phys 2021;31:175–91.
[49] Kretschmer J, Dulkys A, Brodbek L, Stelljes TS, Looe HK, Poppe B. Monte Carlo simulated beam quality and perturbation correction factors for ionization chambers in monoenergetic proton beams. Med Phys 2020;47:5890–905.
[50] Moradi F, Saraee KRE, Bradley DA. Skin dose assessment at diagnostic and therapeutic photon energies: A Monte Carlo study on TLDs. Radiat Phys Chem 2021;185:109502.
[51] Moradi F, Olatunji MA, Sani SFA, Ung NM, Forouzeshfar F, Khandaker MU, et al. Composition and thickness dependence of TLD relative dose sensitivity: A Monte Carlo study. Radiat Meas 2019;129:106191.
[52] Park CR, Kang S-H, Lee Y. Optimization of mask size with median modified Wiener filter algorithm for gamma images using pixelated semiconductor detector: Monte Carlo simulation study. Nucl Instruments Methods Phys Res Sect A Accel Spectrometers, Detect Assoc Equip 2020;980:164472.
[53] Koch-Mehrin KAL, Bugby SL, Lees JE. Modelling Spectroscopic Performance of Pixelated Semiconductor Detectors Through Monte-Carlo Simulation. Adv. X-ray Detect. Technol., Springer; 2022, p. 59–85.
[54] Lee Y, Park C. Evaluation of TlBr semiconductor detector in gamma camera imaging: Monte Carlo simulation study. Nucl Eng Technol 2022.
[55] Hartmann GH, Zink K. A Monte Carlo study on the PTW 60019 microDiamond detector. Med Phys 2019;46:5159–72.
[56] Talamonti C, Kanxheri K, Pallotta S, Servoli L. Diamond Detectors for Radiotherapy X-Ray Small Beam Dosimetry. Front Phys 2021;9:632299.
[57] Hugtenburg RP, Reynard DDH. Monte Carlo based corrections for the dosimetry of x-ray microbeams with diamond detectors. J. Phys. Conf. Ser., vol. 1662, IOP Publishing; 2020, p. 12013.
[58] Waldner L, Rääf C, Hinrichsen Y, Herrnsdorf L, Bernhardsson C. Experimentally determined and Monte Carlo–calculated energy dependence of NaCl pellets read by optically stimulated luminescence for photon beams in the energy range 30 keV to 1.25 MeV. J Radiol Prot 2020;40:1321.
[59] Talbi M, Messaoud M Ben, Sebihi R, Erraoudi M, Azakhmam Y, Khalis M.

Local radiation dosimetry method using optically stimulated pulsed luminescence and Monte Carlo simulation. Adv Life Sci 2021;8:160–6.
[60] Devic S, Liang L, Tomic N, Bekerat H, Morcos M, Popovic M, et al. Dose measurements nearby low energy electronic brachytherapy sources using radiochromic film. Phys Medica 2019;64:40–4.
[61] Vera-Sánchez JA, Ruiz-Morales C, González-López A. Monte Carlo uncertainty analysis of dose estimates in radiochromic film dosimetry with single-channel and multichannel algorithms. Phys Medica 2018;47:23–33.
[62] Parwaie W, Geraily G, Mehri-Kakavand G, Babaloui S, Rezvani S, Pursamimi M. Dosimetry of small photon fields in the presence of bone heterogeneity using MAGIC polymer gel, Gafchromic film, and Monte Carlo simulation. Reports Pract Oncol Radiother 2022.
[63] Buizza G, Paganelli C, Ballati F, Sacco S, Preda L, Iannalfi A, et al. Improving the characterization of meningioma microstructure in proton therapy from conventional apparent diffusion coefficient measurements using Monte Carlo simulations of diffusion MRI. Med Phys 2021;48:1250–61.
[64] Widesott L, Lorentini S, Fracchiolla F, Farace P, Schwarz M. Improvements in pencil beam scanning proton therapy dose calculation accuracy in brain tumor cases with a commercial Monte Carlo algorithm. Phys Med Biol 2018;63:145016.
[65] Poon DMC, Wu S, Ho L, Cheung KY, Yu B. Proton Therapy for Prostate Cancer: Challenges and Opportunities. Cancers (Basel) 2022;14:925.
[66] Maes D, Saini J, Zeng J, Rengan R, Wong T, Bowen SR. Advanced proton beam dosimetry part II: Monte Carlo vs. pencil beam-based planning for lung cancer. Transl Lung Cancer Res 2018;7:114.
[67] Botas P, Kim J, Winey B, Paganetti H. Online adaption approaches for intensity modulated proton therapy for head and neck patients based on cone beam CTs and Monte Carlo simulations. Phys Med Biol 2018;64:15004.
[68] Han DY, Webster MJ, Scanderbeg DJ, Yashar C, Choi D, Song B, et al. Direction-modulated brachytherapy for high-dose-rate treatment of cervical cancer. I: Theoretical design. Int J Radiat Oncol Biol Phys 2014;89:666–73.
[69] Wang C, McNamara A, Shin J, … JS-IJ of, 2020 undefined. End-of-range radiobiological effect on rib fractures in patients receiving proton therapy for breast cancer. Elsevier n.d.
[70] Shin WG, Testa M, Kim HS, Jeong JH, Lee SB, Kim YJ, et al. Independent dose verification system with Monte Carlo simulations using TOPAS for passive scattering proton therapy at the National Cancer Center in Korea. Phys Med Biol 2017;62:7598–616. doi:10.1088/1361-6560/aa8663.
[71] Besemer AE, Yang YM, Grudzinski JJ, Hall LT, Bednarz BP. Development and validation of RAPID: a patient-specific Monte Carlo three-dimensional internal dosimetry platform. Cancer Biother Radiopharm 2018;33:155–65.
[72] Souris K, Barragan Montero A, Janssens G, Di Perri D, Sterpin E, Lee JA. Monte Carlo methods to comprehensively evaluate the robustness of 4D treatments in proton therapy. Med Phys 2019;46:4676–84.

[73] Kozłowska WS, Böhlen TT, Cuccagna C, Ferrari A, Fracchiolla F, Magro G, et al. FLUKA particle therapy tool for Monte Carlo independent calculation of scanned proton and carbon ion beam therapy. Phys Med Biol 2019. doi:10.1088/1361-6560/ab02cb.
[74] Schmitz H, Rabe M, Janssens G, - al, J Qiu RL, Lei Y, et al. Online adaption approaches for intensity modulated proton therapy for head and neck patients based on cone beam CTs and Monte Carlo simulations. Phys Med Biol 2018;64:015004. doi:10.1088/1361-6560/AAF30B.
[75] Dong P, Liu H, Xing L. Monte Carlo tree search-based non-coplanar trajectory design for station parameter optimized radiation therapy (SPORT). Phys Med Biol 2018;63:135014.
[76] Ma J, Wan Chan Tseung HS, Herman MG, Beltran C. A robust intensity modulated proton therapy optimizer based on Monte Carlo dose calculation. Med Phys 2018;45:4045–54.
[77] Kumada H, Takada K, Sakurai Y, Suzuki M, Takata T, Sakurai H, et al. Development of a multimodal monte carlo based treatment planning system. Radiat Prot Dosimetry 2018;180:286–90.
[78] Dauvergne D, Dedes G, Létang JM, Parodi K, Quiñones CT, Testa E, et al. Monte Carlo comparison of x-ray and proton CT for range calculations of proton therapy beams. Phys Med Biol 2015;60:7585.
[79] Alhamada H, Simon S, Philippson C, Vandekerkhove C, Jourani Y, Pauly N, et al. 3D Monte Carlo dosimetry of intraoperative electron radiation therapy (IOERT). Phys Medica 2019;57:207–14.
[80] Almén A, Andersson M, O'Connor U, Abdelrahman M, Camp A, García V, et al. Personal dosimetry using Monte-Carlo simulations for occupational dose monitoring in interventional radiology: the results of a proof of concept in a clinical setting. Radiat Prot Dosimetry 2021;195:391–8.
[81] Peng Z, Fang X, Yan P, Shan H, Liu T, Pei X, et al. A method of rapid quantification of patient-specific organ doses for CT using deep-learning-based multi-organ segmentation and GPU-accelerated Monte Carlo dose computing. Med Phys 2020;47:2526–36.
[82] Deng Y, Chen Z, Wang Q, Yepes P, Shen Z, Chen H, et al. Comparison of pencil beam and Monte Carlo calculations with ion chamber array measurements for patient-specific quality assurance. Radiat Med Prot 2022;3:115–22.
[83] Miksys N, Vigneault E, Martin A-G, Beaulieu L, Thomson RM. Large-scale retrospective Monte Carlo dosimetric study for permanent implant prostate brachytherapy. Int J Radiat Oncol Biol Phys 2017;97:606–15.
[84] Famulari G, Renaud M-A, Poole CM, Evans MDC, Seuntjens J, Enger SA. RapidBrachyMCTPS: a Monte Carlo-based treatment planning system for brachytherapy applications. Phys Med Biol 2018;63:175007.
[85] Glickman H, Antaki M, Deufel C, Enger SA. RapidBrachyMCTPS 2.0: A comprehensive and flexible Monte Carlo-based treatment planning system for brachytherapy applications. ArXiv Prepr ArXiv200702902 2020.

[86] Lemaréchal Y, Bert J, Falconnet C, Després P, Valeri A, Schick U, et al. GGEMS-Brachy: GPU GEant4-based Monte Carlo simulation for brachytherapy applications. Phys Med Biol 2015;60:4987.
[87] Caribé PRR V, Vandenberghe S, Diogo A, Pérez-Benito D, Efthimiou N, Thyssen C, et al. Monte Carlo simulations of the GE Signa PET/MR for different radioisotopes. Front Physiol 2020;11:525575.
[88] Carter LM, Kesner AL, Pratt EC, Sanders VA, Massicano AVF, Cutler CS, et al. The impact of positron range on PET resolution, evaluated with phantoms and PHITS Monte Carlo simulations for conventional and non-conventional radionuclides. Mol Imaging Biol 2020;22:73–84.
[89] Morphis M, van Staden JA, du Raan H, Ljungberg M. Modelling of energy-dependent spectral resolution for SPECT Monte Carlo simulations using SIMIND. Heliyon 2021;7:e06097.
[90] Adnani S, Pil-Ali A, Scott CC, Karim KS. Monte Carlo simulation of an amorphous selenium-based multi-layer photon-counting detector for SPECT applications. Med. Imaging 2021 Phys. Med. Imaging, vol. 11595, SPIE; 2021, p. 306–12.
[91] Sheikhzadeh P, Sabet H, Ghadiri H, Geramifar P, Ghafarian P, Ay MR. Concept design and Monte Carlo performance evaluation of HeadphonePET: a novel brain-dedicated PET system based on partial cylindrical detectors. J Instrum 2018;13:P07008.
[92] Zeraatkar N, Ay MR, Kamali-Asl AR, Zaidi H. Accurate Monte Carlo modeling and performance assessment of the X-PET™ subsystem of the FLEX Triumph™ preclinical PET/CT scanner. Med Phys 2011;38:1217–25.
[93] Khodajou-Chokami H, Hosseini SA, Ay MR, Zaidi H. Mcnp-fbsm: Development of mcnp/mcnpx source model for simulation of multi-slice fan-beam x-ray ct scanners. 2019 IEEE Int. Symp. Med. Meas. Appl., IEEE; 2019, p. 1–6.
[94] Zhao C, Herbst M, Vogt S, Ritschl L, Kappler S, Siewerdsen JH, et al. A robotic X-ray cone-beam CT system: trajectory optimization for 3D imaging of the weight-bearing spine. Med. Imaging 2019 Phys. Med. Imaging, vol. 10948, SPIE; 2019, p. 399–405.
[95] Waeleh N, Saripan MI, Mashohor S. Optimizing positron emission tomography radiation dose using Monte Carlo N-particle simulations 2020.
[96] Tereshchenko SA, Lysenko AY. Reconstruction of the radiation source spatial distribution in a proportional scattering medium. Tech Phys 2021;66:805–14.
[97] Xiang H, Lim H, Fessler JA, Dewaraja YK. A deep neural network for fast and accurate scatter estimation in quantitative SPECT/CT under challenging scatter conditions. Eur J Nucl Med Mol Imaging 2020;47:2956–67.
[98] Nguyen D, Barkousaraie AS, Bohara G, Balagopal A, McBeth R, Lin M-H, et al. A comparison of Monte Carlo dropout and bootstrap aggregation on the performance and uncertainty estimation in radiation therapy dose prediction with deep learning neural networks. Phys Med Biol 2021;66:54002.
[99] Eulitz J, Lutz B, Wohlfahrt P, Dutz A, Enghardt W, Karpowitz C, et al. A

Monte Carlo based radiation response modelling framework to assess variability of clinical RBE in proton therapy. Phys Med Biol 2019;64:225020.
[100] Kayal G, Chauvin M, Vergara-Gil A, Clayton N, Ferrer L, Moalosi T, et al. Generation of clinical 177Lu SPECT/CT images based on Monte Carlo simulation with GATE. Phys Medica 2021;85:24–31.
[101] Moradi F, Saraee KRE, Sani SFA, Bradley DA. Metallic nanoparticle radiosensitization: The role of Monte Carlo simulations towards progress. Radiat Phys Chem 2021;180:109294.
[102] Chow JCL. Recent progress in Monte Carlo simulation on gold nanoparticle radiosensitization. AIMS Biophys 2018;5:231–44.
[103] Li WB, Stangl S, Klapproth A, Shevtsov M, Hernandez A, Kimm MA, et al. Application of High-Z Gold Nanoparticles in Targeted Cancer Radiotherapy—Pharmacokinetic Modeling, Monte Carlo Simulation and Radiobiological Effect Modeling. Cancers (Basel) 2021;13:5370.
[104] Forster JC, Douglass MJJ, Phillips WM, Bezak E. Monte Carlo simulation of the oxygen effect in DNA damage induction by ionizing radiation. Radiat Res 2018;190:248–61.
[105] Margis S, Magouni M, Kyriakou I, Georgakilas AG, Incerti S, Emfietzoglou D. Microdosimetric calculations of the direct DNA damage induced by low energy electrons using the Geant4-DNA Monte Carlo code. Phys Med Biol 2020;65:45007.
[106] Sakata D, Belov O, Bordage M-C, Emfietzoglou D, Guatelli S, Inaniwa T, et al. Fully integrated Monte Carlo simulation for evaluating radiation induced DNA damage and subsequent repair using Geant4-DNA. Sci Rep 2020;10:1–13.
[107] Chatzipapas KP, Papadimitroulas P, Emfietzoglou D, Kalospyros SA, Hada M, Georgakilas AG, et al. Ionizing radiation and complex DNA damage: Quantifying the radiobiological damage using Monte Carlo simulations. Cancers (Basel) 2020;12:799.
[108] Yeh J-K, Chen C-H. Estimated radiation risk of cancer from dental cone-beam computed tomography imaging in orthodontics patients. BMC Oral Health 2018;18:1–8.
[109] Saghi MH, Mohammadi AA, Ghaderpoori M, Ghaderpoury A, Alinejad A. Estimate the effective dose of gamma radiation in Iran cities: lifetime cancer risk by Monte Carlo simulation model. Environ Geochem Health 2019;41:2549–58.
[110] Lai Y, Jia X, Chi Y. Modeling the effect of oxygen on the chemical stage of water radiolysis using GPU-based microscopic Monte Carlo simulations, with an application in FLASH radiotherapy. Phys Med Biol 2021;66:25004.
[111] Liew H, Mein S, Dokic I, Haberer T, Debus J, Abdollahi A, et al. Deciphering time-dependent DNA damage complexity, repair, and oxygen tension: a mechanistic model for FLASH-dose-rate radiation therapy. Int J Radiat Oncol Biol Phys 2021;110:574–86.
[112] Alloni D, Prata M, Smilgys B. Experimental and Monte Carlo characterization

of radionuclidic impurities originated from proton irradiation of [18O] H2O in a modern medical cyclotron. Appl Radiat Isot 2019;146:84–9.
[113] Rigby A, Blower JE, Blower PJ, Terry SYA, Abbate V. Targeted Auger electron-emitter therapy: Radiochemical approaches for thallium-201 radiopharmaceuticals. Nucl Med Biol 2021;98:1–7.
[114] Pampena R, Palmieri T, Kyrgidis A, Ramundo D, Iotti C, Lallas A, et al. Orthovoltage radiotherapy for nonmelanoma skin cancer (NMSC): comparison between 2 different schedules. J Am Acad Dermatol 2016;74:341–7.
[115] Shah C, Kamrava M, Thaker NG. Evaluating reimbursement of skin radiation therapy: Technique and fractionation. Brachytherapy 2020;19:700–4.
[116] Duinkerken CW, Lohuis PJFM, Crijns MB, Navran A, Haas RLM, Hamming-Vrieze O, et al. Orthovoltage X-rays for postoperative treatment of resected basal cell carcinoma in the head and neck area. J Cutan Med Surg 2017;21:243–9.
[117] Khoo AM, Cho SH, Reynoso FJ, Aliru M, Aziz K, Bodd M, et al. Radiosensitization of prostate cancers in vitro and in vivo to erbium-filtered orthovoltage X-rays using actively targeted gold nanoparticles. Sci Rep 2017;7:1–13.
[118] Bell BI, Vercellino J, Brodin NP, Velten C, Nanduri LSY, Nagesh PKB, et al. Orthovoltage x-rays exhibit increased efficacy compared with γ-rays in preclinical irradiation. Cancer Res 2022;82:2678–91.
[119] Buonanno F, Di Lillo F, Sarno A, Mettivier G, Russo P. 188 Orthovoltage rotational breast radiotherapy: A Monte Carlo and experimental study. Phys Medica Eur J Med Phys 2018;56:177–8.
[120] Kamali-Zonouzi P, Shutt A, Nisbet A, Bradley DA. Feasibility of employing thick microbeams from superficial and orthovoltage kVp x-ray tubes for radiotherapy of superficial cancers. Radiat Phys Chem 2017;140:237–41.
[121] Cheraghi N, Cognetta Jr A, Goldberg D. Radiation therapy for the adjunctive treatment of surgically excised keloids: a review. J Clin Aesthet Dermatol 2017;10:12.
[122] Adlienė D, Jaselskė E, Urbonavičius BG, Laurikaitienė J, Rudžianskas V, Didvalis T. Development of 3D printed phantom for dose verification in radiotherapy for the patient with metal artefacts inside. IFMBE Proc 2019;68:643–7. doi:10.1007/978-981-10-9023-3_119/COVER.
[123] Adlienė D, Jaselskė E, Rudžianskas V, Šeperienė N. First approach to ionizing radiation based 3D printing: fabrication of free standing dose gels using high energy gamma photons. Nucl Instruments Methods Phys Res Sect B Beam Interact with Mater Atoms 2018. doi:10.1016/j.nimb.2018.01.033.
[124] Ilina A, Pinter C, Lasso A, Lai I, Joshi C, Alexander K, et al. Target Definition with 3D Surface Scanning for Orthovoltage Radiation Therapy Planning n.d.
[125] Nikandrovs M, McClean B, Shields L, McCavana P, Vintró LL. Clinical treatment planning for kilovoltage radiotherapy using EGSnrc and Python. J Appl Clin Med Phys 2022. doi:10.1002/ACM2.13832.

[126] Penchev P, Mäder U, Fiebich M, Zink K. Design and evaluation of a Monte Carlo based model of an orthovoltage treatment system. Z Med Phys 2015;25:341–52. doi:10.1016/J.ZEMEDI.2015.05.005.
[127] Schneider F, Bludau F, Clausen S, Fleckenstein J, Obertacke U, Wenz F. Precision IORT–Image guided intraoperative radiation therapy (igIORT) using online treatment planning including tissue heterogeneity correction. Phys Medica 2017;37:82–7.
[128] Chow JCL, Grigorov GN. Effect of the bone heterogeneity on the dose prescription in orthovoltage radiotherapy: A Monte Carlo study. Reports Pract Oncol Radiother 2012;17:38–43.
[129] Hernandez AM, Seibert JA, Boone JM. Breast dose in mammography is about 30% lower when realistic heterogeneous glandular distributions are considered. Med Phys 2015;42:6337–48.
[130] S Chu VW, K Kan MW, Y Lee LK, - al, Rabus H, Gargioni E, et al. Monte Carlo simulation on pre-clinical irradiation: A heterogeneous phantom study on monoenergetic kilovoltage photon beams. J Phys Conf Ser 2012;385:012013. doi:10.1088/1742-6596/385/1/012013.
[131] Katsifis GA, McKenzie DR, Suchowerska N. Monte Carlo calculations of radiotherapy dose distributions within and around orthopaedic implants. Phys Imaging Radiat Oncol 2022;22:123. doi:10.1016/J.PHRO.2022.04.011.
[132] Çatli S. High-density dental implants and radiotherapy planning: Evaluation of effects on dose distribution using pencil beam convolution algorithm and Monte Carlo method. J Appl Clin Med Phys 2015;16:46–52. doi:10.1120/jacmp.v16i5.5612.
[133] Sarigul N. Evaluation of the effect of field sizes on radiation dose in the presence of metal materials using Monte Carlo simulation. Appl Radiat Isot 2022;182:110143. doi:10.1016/J.APRADISO.2022.110143.
[134] Rousselle A, Amelot A, Thariat J, Jacob J, Mercy G, De Marzi L, et al. Metallic implants and CT artefacts in the CTV area: Where are we in 2020? Cancer/Radiothérapie 2020;24:658–66.
[135] Laftah WA, Hashim S, Ibrahim AN. Polymer hydrogels: A review. Polym Plast Technol Eng 2011;50:1475–86.
[136] Naficy S, Brown HR, Razal JM, Spinks GM, Whitten PG. Progress toward robust polymer hydrogels. Aust J Chem 2011;64:1007–25.
[137] Li W, Lu H, Zhang N, Ma M. Enhancing the properties of conductive polymer hydrogels by freeze–thaw cycles for high-performance flexible supercapacitors. ACS Appl Mater Interfaces 2017;9:20142–9.
[138] Gotovtsev PM, Badranova GU, Zubavichus Y V, Chumakov NK, Antipova CG, Kamyshinsky RA, et al. Electroconductive PEDOT: PSS-based hydrogel prepared by freezing-thawing method. Heliyon 2019;5:e02498.
[139] Wu Q, Therriault D, Heuzey M-C. Processing and properties of chitosan inks for 3D printing of hydrogel microstructures. ACS Biomater Sci Eng 2018;4:2643–52.
[140] Küçüktürkmen B, Öz UC, Bozkir A. In situ hydrogel formulation for intra-

articular application of diclofenac sodium-loaded polymeric nanoparticles. Turkish J Pharm Sci 2017;14:56.
[141] Lee S, Lee H, Sim JH, Sohn D. Graphene oxide/poly (acrylic acid) hydrogel by γ-ray pre-irradiation on graphene oxide surface. Macromol Res 2014;22:165–72.
[142] Li L, Scheiger JM, Levkin PA. Design and applications of photoresponsive hydrogels. Adv Mater 2019;31:1807333.
[143] Nho Y-C, Park J-S, Lim Y-M. Preparation of poly (acrylic acid) hydrogel by radiation crosslinking and its application for mucoadhesives. Polymers (Basel) 2014;6:890–8.
[144] Maitra J, Shukla VK. Cross-linking in hydrogels-a review. Am J Polym Sci 2014;4:25–31.
[145] Hennink WE, van Nostrum CF. Novel crosslinking methods to design hydrogels. Adv Drug Deliv Rev 2012;64:223–36.
[146] Davis NE, Ding S, Forster RE, Pinkas DM, Barron AE. Modular enzymatically crosslinked protein polymer hydrogels for in situ gelation. Biomaterials 2010;31:7288–97.
[147] Johnston TG, Yuan S-F, Wagner JM, Yi X, Saha A, Smith P, et al. Compartmentalized microbes and co-cultures in hydrogels for on-demand bioproduction and preservation. Nat Commun 2020;11:1–11.
[148] Zhang Q, Chen B, Tao L, Yan M, Chen L, Wei Y. Microorganism inspired hydrogels: hierarchical super/macro-porous structure, rapid swelling rate and high adsorption. RSC Adv 2014;4:32475–81.
[149] Deng C, Li F, Hackett JM, Chaudhry SH, Toll FN, Toye B, et al. Collagen and glycopolymer based hydrogel for potential corneal application. Acta Biomater 2010;6:187–94.
[150] Bhattarai N, Gunn J, Zhang M. Chitosan-based hydrogels for controlled, localized drug delivery. Adv Drug Deliv Rev 2010;62:83–99.
[151] Ahmadi F, Oveisi Z, Samani SM, Amoozgar Z. Chitosan based hydrogels: characteristics and pharmaceutical applications. Res Pharm Sci 2015;10:1.
[152] Zhang M, Zhao X. Alginate hydrogel dressings for advanced wound management. Int J Biol Macromol 2020;162:1414–28.
[153] Zhao W, Jin X, Cong Y, Liu Y, Fu J. Degradable natural polymer hydrogels for articular cartilage tissue engineering. J Chem Technol Biotechnol 2013;88:327–39.
[154] Yan C, Kramer PL, Yuan R, Fayer MD. Water dynamics in polyacrylamide hydrogels. J Am Chem Soc 2018;140:9466–77.
[155] Zhu J. Bioactive modification of poly (ethylene glycol) hydrogels for tissue engineering. Biomaterials 2010;31:4639–56.
[156] Ahmadian Y, Bakravi A, Hashemi H, Namazi H. Synthesis of polyvinyl alcohol/CuO nanocomposite hydrogel and its application as drug delivery agent. Polym Bull 2019;76:1967–83.
[157] Millon LE, Mohammadi H, Wan WK. Anisotropic polyvinyl alcohol hydrogel for cardiovascular applications. J Biomed Mater Res Part B Appl Biomater An

Off J Soc Biomater Japanese Soc Biomater Aust Soc Biomater Korean Soc Biomater 2006;79:305–11.
[158] Zhou C, Wu Q. A novel polyacrylamide nanocomposite hydrogel reinforced with natural chitosan nanofibers. Colloids Surfaces B Biointerfaces 2011;84:155–62.
[159] Rodríguez-Rodríguez R, Espinosa-Andrews H, Velasquillo-Martínez C, García-Carvajal ZY. Composite hydrogels based on gelatin, chitosan and polyvinyl alcohol to biomedical applications: a review. Int J Polym Mater Polym Biomater 2020;69:1–20.
[160] Peppas NA, Huang Y, Torres-Lugo M, Ward JH, Zhang J. Physicochemical foundations and structural design of hydrogels in medicine and biology. Annu Rev Biomed Eng 2000;2:9–29.
[161] Vasile C, Pamfil D, Stoleru E, Baican M. New developments in medical applications of hybrid hydrogels containing natural polymers. Molecules 2020;25:1539.
[162] Yang Z, Chen L, McClements DJ, Qiu C, Li C, Zhang Z, et al. Stimulus-responsive hydrogels in food science: A review. Food Hydrocoll 2022;124:107218.
[163] Li J, Jia X, Yin L. Hydrogel: Diversity of structures and applications in food science. Food Rev Int 2021;37:313–72.
[164] Puoci F, Iemma F, Spizzirri UG, Cirillo G, Curcio M, Picci N. Polymer in agriculture: a review. Am J Agric Biol Sci 2008;3:299–314.
[165] Sharma G, Thakur B, Naushad M, Kumar A, Stadler FJ, Alfadul SM, et al. Applications of nanocomposite hydrogels for biomedical engineering and environmental protection. Environ Chem Lett 2018;16:113–46.
[166] Baldock C, De Deene Y, Doran S, Ibbott G, Jirasek A, Lepage M, et al. Polymer gel dosimetry. Phys Med Biol 2010. doi:10.1088/0031-9155/55/5/R01.
[167] Jirasek A, Hilts M, McAuley KB. Polymer gel dosimeters with enhanced sensitivity for use in x-ray CT polymer gel dosimetry. Phys Med Biol 2010;55:5269.
[168] Dhakal R, Yosofvand M, Moussa H. Development and application of magic-f gel in cancer research and medical imaging. Appl Sci 2021;11:7783.
[169] Valente M, Vedelago J, Chacón D, Mattea F, Velásquez J, Pérez P. Water-equivalence of gel dosimeters for radiology medical imaging. Appl Radiat Isot 2018;141:193–8.
[170] Farhood B, Geraily G, Abtahi SMM. A systematic review of clinical applications of polymer gel dosimeters in radiotherapy. Appl Radiat Isot 2019;143:47–59.
[171] Vandecasteele J, De Deene Y. On the validity of 3D polymer gel dosimetry: III. MRI-related error sources. Phys Med Biol 2012;58:63.
[172] Vandecasteele J, De Deene Y. On the validity of 3D polymer gel dosimetry: I. Reproducibility study. Phys Med Biol 2012;58:19.
[173] Vandecasteele J, De Deene Y. On the validity of 3D polymer gel dosimetry:

II. Physico-chemical effects. Phys Med Biol 2012;58:43.
[174] Azadeh P, Amiri S, Mostaar A, Joybari AY, Paydar R. Evaluation of MAGIC-f polymer gel dosimeter for dose profile measurement in small fields and stereotactic irradiation. Radiat Phys Chem 2022;194:109991.
[175] Silveira MA, Pavoni JF, Baffa O. Three-dimensional quality assurance of IMRT prostate plans using gel dosimetry. Phys Medica 2017;34:1–6.
[176] Schreiner LJ. Review of Fricke gel dosimeters. J. Phys. Conf. Ser., vol. 3, IOP Publishing; 2004, p. 3.
[177] Schreiner LJ. True 3D chemical dosimetry (gels, plastics): Development and clinical role. J. Phys. Conf. Ser., vol. 573, IOP Publishing; 2015, p. 12003.
[178] Fong PM, Keil DC, Does MD, Gore JC. Polymer gels for magnetic resonance imaging of radiation dose distributions at normal room atmosphere. Phys Med Biol 2001;46:3105.
[179] Hurley C, Venning A, Baldock C. A study of a normoxic polymer gel dosimeter comprising methacrylic acid, gelatin and tetrakis (hydroxymethyl) phosphonium chloride (MAGAT). Appl Radiat Isot 2005;63:443–56.
[180] Abtahi SM, Zahmatkesh MH, Khalafi H. Investigation of an improved MAA-based polymer gel for thermal neutron dosimetry. J Radioanal Nucl Chem 2016;307:855–68.
[181] De Deene Y, Vergote K, Claeys C, De Wagter C. The fundamental radiation properties of normoxic polymer gel dosimeters: a comparison between a methacrylic acid based gel and acrylamide based gels. Phys Med Biol 2006;51:653.
[182] Moftah B, Basfar AA, Almousa AA, Al Kafi AM, Rabaeh KA. Novel 3D polymer gel dosimeters based on N-(3-Methoxypropyl) acrylamide (NMPAGAT) for quality assurance in radiation oncology. Radiat Meas 2020;135:106372.
[183] Basfar AA, Moftah B, Rabaeh KA, Almousa AA. Novel composition of polymer gel dosimeters based on N-(Hydroxymethyl) acrylamide for radiation therapy. Radiat Phys Chem 2015;112:117–20.
[184] Kozicki M, Jaszczak M, Maras P, Dudek M, Cłapa M. On the development of a VIPARnd radiotherapy 3D polymer gel dosimeter. Phys Med Biol 2017;62:986.
[185] Hiroki A, Yamashita S, Sato Y, Nagasawa N, Taguchi M. New polymer gel dosimeters consisting of less toxic monomers with radiation-crosslinked gel matrix. J. Phys. Conf. Ser., vol. 444, IOP Publishing; 2013, p. 12028.
[186] Hiroki A, Yamashita S, Taguchi M. Enhancement in dose sensitivity of polymer gel dosimeters composed of radiation-crosslinked gel matrix and less toxic monomers. J. Phys. Conf. Ser., vol. 573, IOP Publishing; 2015, p. 12028.
[187] Gallo S, Giorgio C, Giuseppina I, Anna L, Luigi T, Antonio B, et al. Preliminary magnetic resonance relaxometric analysis of Fricke gel dosimeters produced with polyvinyl alcohol and glutaraldehyde 2017.
[188] Rabaeh KA, Hailat TF, Eyadeh MM, Al-Shorman MY, Aldweri FM, Alheet SM, et al. Dosimetric properties of sulfosalicylic acid-ferrous-polyvinyl

alcohol-glutaraldehyde hydrogel dosimeters using magnetic and optical techniques. Radiat Phys Chem 2020;177:109106.
[189] Hayashi S, Ono K, Fujino K, Ikeda S, Tanaka K. Novel radiochromic gel dosimeter based on a polyvinyl alcohol–Iodide complex. Radiat Meas 2020;131:106226.
[190] De Deene Y. Fundamentals of MRI measurements for gel dosimetry. J. Phys. Conf. Ser., vol. 3, IOP Publishing; 2004, p. 9.
[191] De Deene Y. How to scan polymer gels with MRI? J. Phys. Conf. Ser., vol. 250, IOP Publishing; 2010, p. 12015.
[192] Kroll F, Pawelke J, Karsch L. Preliminary investigations on the determination of three-dimensional dose distributions using scintillator blocks and optical tomography. Med Phys 2013;40:82104.
[193] Olding T, Schreiner LJ. Cone-beam optical computed tomography for gel dosimetry II: imaging protocols. Phys Med Biol 2011;56:1259.
[194] Wolodzko JG, Marsden C, Appleby A. CCD imaging for optical tomography of gel radiation dosimeters. Med Phys 1999;26:2508–13.
[195] Eyadeh MM, Smadi SA, Rabaeh KA, Oglat AA, Diamond KR. Effect of lithium chloride inorganic salt on the performance of N-(Hydroxymethyl) acrylamide polymer-gel dosimeter in radiation therapy. J Radioanal Nucl Chem 2021;330:1255–61.
[196] Hayashi S, Fujiwara F, Usui S, Tominaga T. Effect of inorganic salt on the dose sensitivity of polymer gel dosimeter. Radiat Phys Chem 2012;81:884–8.
[197] Behrouzkia Z, Zohdiaghdam R, Khalkhali HR, Mousavi F. Evaluation of gold nanoparticle size effect on dose enhancement factor in megavoltage beam radiotherapy using MAGICA polymer gel dosimeter. J Biomed Phys Eng 2019;9:89.
[198] Deyhimihaghighi N, Noor NM, Soltani N, Jorfi R, Haghir ME, Adenan MZ, et al. Contrast enhancement of magnetic resonance imaging (MRI) of polymer gel dosimeter by adding Platinum nano-particles. J. Phys. Conf. Ser., vol. 546, IOP Publishing; 2014, p. 12013.
[199] Farahani S, Alam NR, Haghgoo S, Shirazi A, Geraily G, Gorji E, et al. The effect of bismuth nanoparticles in kilovoltage and megavoltage radiation therapy using magnetic resonance imaging polymer gel dosimetry. Radiat Phys Chem 2020;170:108573.
[200] Mori H, Müller AHE. New polymeric architectures with (meth) acrylic acid segments. Prog Polym Sci 2003;28:1403–39.
[201] Qi X, Wei W, Li J, Liu Y, Hu X, Zhang J, et al. Fabrication and characterization of a novel anticancer drug delivery system: salecan/poly (methacrylic acid) semi-interpenetrating polymer network hydrogel. ACS Biomater Sci Eng 2015;1:1287–99.
[202] Schuurmans CCL, Mihajlovic M, Hiemstra C, Ito K, Hennink WE, Vermonden T. Hyaluronic acid and chondroitin sulfate (meth) acrylate-based hydrogels for tissue engineering: Synthesis, characteristics and pre-clinical evaluation. Biomaterials 2021;268:120602.

[203] Yan L, Han K, Pang B, Jin H, Zhao X, Xu X, et al. Surfactin-reinforced gelatin methacrylate hydrogel accelerates diabetic wound healing by regulating the macrophage polarization and promoting angiogenesis. Chem Eng J 2021;414:128836.
[204] He H, Xiao Z, Zhou Y, Chen A, Xuan X, Li Y, et al. Zwitterionic poly (sulfobetaine methacrylate) hydrogels with optimal mechanical properties for improving wound healing in vivo. J Mater Chem B 2019;7:1697–707.
[205] McAuley KB. Fundamentals of polymer gel dosimeters. J. Phys. Conf. Ser., vol. 56, IOP Publishing; 2006, p. 4.
[206] Storey R, Vana P, Yagci Y. Fundamentals of controlled/living radical polymerization. Royal Society of Chemistry; 2013.
[207] Kröger LC, Kopp WA, Leonhard K. Prediction of chain propagation rate constants of polymerization reactions in aqueous NIPAM/BIS and VCL/BIS systems. J Phys Chem B 2017;121:2887–95.
[208] Moad G, Solomon DH. The chemistry of radical polymerization. Elsevier; 2006.
[209] Libretexts C. 9.10: Bond Energies and Bond Lengths. ChemLibretextsOrg 2017.
[210] Ashfaq A, Clochard M-C, Coqueret X, Dispenza C, Driscoll MS, Ulański P, et al. Polymerization reactions and modifications of polymers by ionizing radiation. Polymers (Basel) 2020;12:2877.
[211] Beuermann S, Buback M, Hesse P, Kuchta F-D, Lacík I, Van Herk AM. Critically evaluated rate coefficients for free-radical polymerization Part 6: Propagation rate coefficient of methacrylic acid in aqueous solution (IUPAC Technical Report). Pure Appl Chem 2007;79:1463–9.
[212] Yamada B, Zetterlund PB. General chemistry of radical polymerization. Handb Radic Polym 2002:117–86.
[213] Drawe P, Buback M. The PLP-SEC Method: Perspectives and Limitations. Macromol Theory Simulations 2016;25:74–84.
[214] Marien YW, Edeleva M, Van Steenberge PHM, D'hooge DR. Exploiting the pulsed laser polymerization-size exclusion chromatography technique to retrieve kinetic parameters in radical polymerization: State-of-the-art and future challenges. Adv. Chem. Eng., vol. 56, Elsevier; 2020, p. 59–95.
[215] Gao H, Oakley LH, Konstantinov IA, Arturo SG, Broadbelt LJ. Acceleration of kinetic Monte Carlo method for the simulation of free radical copolymerization through scaling. Ind Eng Chem Res 2015;54:11975–85.
[216] Hamzehlou S, Reyes Y, Leiza JR. A new insight into the formation of polymer networks: a kinetic monte carlo simulation of the cross-linking polymerization of s/dvb. Macromolecules 2013;46:9064–73.
[217] Marien YW, Van Steenberge PHM, R. D 'hooge D, Marin GB. Particle by particle kinetic monte carlo tracking of reaction and mass transfer events in miniemulsion free radical polymerization. Macromolecules 2019;52:1408–23.
[218] Drache M, Drache G. Simulating controlled radical polymerizations with mcPolymer—A Monte Carlo approach. Polymers (Basel) 2012;4:1416–42.

[219] Vogiatzis GG, Voyiatzis E, Theodorou DN. Monte Carlo simulations of a coarse grained model for an athermal all-polystyrene nanocomposite system. Eur Polym J 2011;47:699–712.
[220] Schneider L, Müller M. Multi-architecture Monte-Carlo (MC) simulation of soft coarse-grained polymeric materials: SOft coarse grained Monte-Carlo Acceleration (SOMA). Comput Phys Commun 2019;235:463–76.
[221] Morgane M, Zhai Z, Perez M, Lame O, Fusco C, Chazeau L, et al. Polymer Chain Generation for Coarse-Grained Models Using Radical-Like Polymerization. Commun Comput Phys 2018;24:885–98.
[222] Rubinstein RY, Kroese DP. Simulation and the Monte Carlo Method: Third Edition. Simul Monte Carlo Method Third Ed 2016:1–414. doi:10.1002/9781118631980.
[223] Van Steenberge PHM, D'hooge DR, Reyniers M-F, Marin GB. Improved kinetic Monte Carlo simulation of chemical composition-chain length distributions in polymerization processes. Chem Eng Sci 2014;110:185–99.
[224] Desmet GB, Marien YW, Van Steenberge PHM, D'hooge DR, Reyniers M-F, Marin GB. Ab initio based kinetic Monte Carlo analysis to unravel the propagation kinetics in vinyl acetate pulsed laser polymerization. Polym Chem 2017;8:7143–50.
[225] Wang R, Lin T-S, Johnson JA, Olsen BD. Kinetic Monte Carlo simulation for quantification of the gel point of polymer networks. ACS Macro Lett 2017;6:1414–9.
[226] Pirman T, Ocepek M, Likozar B. Radical Polymerization of Acrylates, Methacrylates, and Styrene: Biobased Approaches, Mechanism, Kinetics, Secondary Reactions, and Modeling. Ind Eng Chem Res 2021;60:9347–67.
[227] Mulderrig J, Talamini B, Bouklas N. A statistical mechanics framework for polymer chain scission, based on the concepts of distorted bond potential and asymptotic matching. ArXiv Prepr ArXiv220807352 2022.
[228] Theodorakopoulos N. Statistical mechanics of simple polymer chain models. Stat Phys DNA 2020:1–17. doi:10.1142/9789811209543_0001.
[229] Demir B, Walsh TR. A versatile computational procedure for chain-growth polymerization using molecular dynamics simulations. ACS Appl Polym Mater 2019;1:3027–38.
[230] Binder K. Monte Carlo and molecular dynamics simulations in polymer science. Oxford University Press; 1995.
[231] Gissinger JR, Jensen BD, Wise KE. Modeling chemical reactions in classical molecular dynamics simulations. Polymer (Guildf) 2017;128:211–7.
[232] Perez M, Lame O, Leonforte F, Barrat J-L. Polymer chain generation for coarse-grained models using radical-like polymerization. J Chem Phys 2008;128:234904.
[233] Liu H, Zhu Y, Lu Z, Müller-Plathe F. A kinetic chain growth algorithm in coarse-grained simulations. J Comput Chem 2016;37:2634–46.
[234] Oliveira FA, Taylor PL. Breaking in polymer chains. II. The Lennard-Jones chain. J Chem Phys 1994;101:10118–25.

[235] Abrams CF, Kremer K. Effects of excluded volume and bond length on the dynamics of dense bead-spring polymer melts. J Chem Phys 2002;116:3162–5.
[236] Mattei MR, Frunzo L, D'acunto B, Pechaud Y, Pirozzi F, Esposito G. Continuum and discrete approach in modeling biofilm development and structure: a review. J Math Biol 2018;76:945–1003.
[237] Erol O, Pantula A, Liu W, Gracias DH. Transformer hydrogels: a review. Adv Mater Technol 2019;4:1900043.
[238] Markovic MD, Spasojevic PM, Seslija SI, Popovic IG, Veljovic DN, Pjanovic R V, et al. Casein-poly (methacrylic acid) hybrid soft networks with easy tunable properties. Eur Polym J 2019;113:276–88.
[239] Das IJ. Radiochromic film: Role and applications in radiation dosimetry. 2017. doi:10.1201/b20964.
[240] Palmer AL, Dimitriadis A, Nisbet A, Clark CH. Evaluation of Gafchromic EBT-XD film, with comparison to EBT3 film, and application in high dose radiotherapy verification. Phys Med Biol 2015. doi:10.1088/0031-9155/60/22/8741.
[241] Butson M, Niroomand-Rad A. Historical background, development, and construction of radiochromic films. Radiochromic Film Role Appl. Radiat. Dosim., 2017. doi:10.1201/b20964.
[242] Harms Sr WB, Low DA, Wong JW, Purdy JA. A software tool for the quantitative evaluation of 3D dose calculation algorithms. Med Phys 1998;25:1830–6.
[243] Low DA, Harms WB, Mutic S, Purdy JA. A technique for the quantitative evaluation of dose distributions. Med Phys 1998. doi:10.1118/1.598248.
[244] Winiecki J, Morgaś T, Majewska K, Drzewiecka B. The gamma evaluation method as a routine QA procedure of IMRT. Reports Pract Oncol Radiother 2009. doi:10.1016/S1507-1367(10)60031-4.
[245] Depuydt T, Van Esch A, Huyskens DP. A quantitative evaluation of IMRT dose distributions: Refinement and clinical assessment of the gamma evaluation. Radiother Oncol 2002. doi:10.1016/S0167-8140(01)00497-2.
[246] Jiang SB, Sharp GC, Neicu T, Berbeco RI, Flampouri S, Bortfeld T. On dose distribution comparison. Phys Med Biol 2006. doi:10.1088/0031-9155/51/4/001.
[247] Durán-Nava OE, Torres-García E, Oros-Pantoja R, Hernández-Oviedo JO. Monte Carlo simulation and experimental evaluation of dose distributions produced by a 6 MV medical linear accelerator. J. Phys. Conf. Ser., 2019. doi:10.1088/1742-6596/1221/1/012079.
[248] Hussein M, Clark CH, Nisbet A. Challenges in calculation of the gamma index in radiotherapy – Towards good practice. Phys Medica 2017. doi:10.1016/j.ejmp.2017.03.001.
[249] Ferrari A, Sala PR, Fassò A, Ranft J. FLUKA: A Multi-Particle Transport Code. 2005.
[250] Ballarini F, Battistoni G, Campanella M, Carboni M, Cerutti F, Empl A, et al.

The FLUKA code: An overview. J. Phys. Conf. Ser., vol. 41, 2006, p. 151–60. doi:10.1088/1742-6596/41/1/014.
[251] Fasso A, Ferrari A, Ranft J, Sala PR. FLUKA-2011 manual. 2011.
[252] Marsaglia G, Tsang WW. The 64-bit universal RNG. Stat Probab Lett 2004;66:183–7.
[253] Vlachoudis V. Flair: A powerful but user friendly graphical interface for FLUKA. Am. Nucl. Soc. - Int. Conf. Math. Comput. Methods React. Phys. 2009, M C 2009, 2009.
[254] Rajabi R, Taherparvar P. Monte Carlo dosimetry for a new 32P brachytherapy source using FLUKA code. J Contemp Brachytherapy 2019;11:76–90.
[255] Anjomrouz M, Sadeghi M, Haddadi A. Monte Carlo characterization of as a high-dose-rate source for brachytherapy application by FLUKA code. J Appl Clin Med Phys 2013;14:196–205.
[256] Hanouf N, Krim D, Zerfaoui M, Bakari D, Rrhioua A. Investigation of TG-43 Dosimetric Parameters for $$^{192} Ir $$ HDR Brachytherapy Source Using FLUKA. Int. Conf. Electron. Eng. Renew. Energy, Springer; 2020, p. 367–74.
[257] Anjomrouz M, Bakht MK, Sadeghi M. Feasibility study of FLUKA Monte Carlo simulation for a beta-emitting brachytherapy source: dosimetric parameters of 142Pr glass seed. J Radioanal Nucl Chem 2016;309:947–53.
[258] ICRP. ICRP Publication 110: Adult reference computational phantoms. Ann ICRP 2008;39:1–165.
[259] Theis C, Buchegger KH, Brugger M, Forkel-Wirth D, Roesler S, Vincke H. Interactive three-dimensional visualization and creation of geometries for Monte Carlo calculations. Nucl Instruments Methods Phys Res Sect A Accel Spectrometers, Detect Assoc Equip 2006;562:827–9. doi:10.1016/j.nima.2006.02.125.
[260] Waters LS, McKinney GW, Durkee JW, Fensin ML, Hendricks JS, James MR, et al. The MCNPX Monte Carlo radiation transport code. AIP Conf. Proc., 2007. doi:10.1063/1.2720459.
[261] TOP500. 2022 | TOP500 2022. https://www.top500.org/lists/top500/2022/11/ (accessed January 14, 2023).
[262] Poludniowski G, Landry G, Deblois F, Evans PM, Verhaegen F. SpekCalc: A program to calculate photon spectra from tungsten anode x-ray tubes. Phys Med Biol 2009;54. doi:10.1088/0031-9155/54/19/N01.
[263] Poludniowski GG. Calculation of x-ray spectra emerging from an x-ray tube. Part II. X-ray production and filtration in x-ray targets. Med Phys 2007;34:2175–86. doi:10.1118/1.2734726.
[264] Poludniowski GG, Evans PM. Calculation of x-ray spectra emerging from an x-ray tube. Part I. Electron penetration characteristics in x-ray targets. Med Phys 2007;34:2164–74. doi:10.1118/1.2734725.
[265] Niroomand-Rad A, Chiu-Tsao S, Grams MP, Lewis DF, Soares CG, Van Battum LJ, et al. Report of AAPM task group 235 radiochromic film dosimetry: an update to TG-55. Med Phys 2020;47:5986–6025.
[266] Parwaie W, Geraily G, Shirazi A, Yarahmadi M, Shakeri A, Ardekani MA.

Evaluation of lung heterogeneity effects on dosimetric parameters in small photon fields using MAGIC polymer gel, Gafchromic film, and Monte Carlo simulation. Appl Radiat Isot 2020;166:109233.
[267] Wang E, Zhang Q, Shen B, Zhang G, Lu X, Wu Q, et al. Intel Math Kernel Library. High-Performance Comput Intel® Xeon Phi™ 2014:167–88. doi:10.1007/978-3-319-06486-4_7.
[268] Gilbert EG, Johnson DW, Keerthi SS. A fast procedure for computing the distance between complex objects in three-dimensional space. IEEE J Robot Autom 1988;4:193–203.
[269] Lacik I, Ucnova L, Kukuckova S, Buback M, Hesse P, Beuermann S. Propagation rate coefficient of free-radical polymerization of partially and fully ionized methacrylic acid in aqueous solution. Macromolecules 2009;42:7753–61.
[270] Beuermann S, Buback M, Hesse P, Lacík I. Free-radical propagation rate coefficient of nonionized methacrylic acid in aqueous solution from low monomer concentrations to bulk polymerization. Macromolecules 2006;39:184–93.
[271] Low DA. Gamma dose distribution evaluation tool. J. Phys. Conf. Ser., 2010. doi:10.1088/1742-6596/250/1/012071.

CURRICULUM VITAE

Aleksandras Ševčik

SUMMARY

My research focuses on the modeling of energy transfer processes in photon irradiated polymer matrixes and radiation-induced changes in radio-sensitive gels. I am working with FLUKA high particle physics simulation package and C++/Python.

My principal emphasis is the development of a Monte Carlo code to simulate the evolution of polymers under irradiation. The program simulates the dynamics of polymer interactions, including connections, divisions, rotations, and translations, using input from ab-initio quantum models. Complex architectures of polymer geometries are seen in three dimensions, together with pertinent data. The code is developed in C++ version 17.

EDUCATION

2018 - 2023	Technological sciences, Materials engineering, PhD Kaunas University of Technology, Lithuania
2015 -2017	Medical Physics, MSc magna cum laude Kaunas University of Technology, Lithuania MSc topic: "Monte Carlo modelling of brachytherapy source in an anthropomorphic head phantom"
2012 -2014	Offshore Technology Engineering, MSc University of Stavanger, Norway

EXPERIENCE

09/2018 – present	PhD position in Kaunas University of Technology, Lithuania
05/2013 – 08/2015	Engineer , Aker Solutions, Norway

SKILLS

C++	2018 – ongoing	Intermediate
Python	2018 – ongoing	Intermediate
FLUKA	2019 – ongoing	Intermediate

LANGUAGES

English	Fluent

LIST OF PUBLICATIONS

Articles published in journals belonging to the scientific international databases Clarivate Analytics. Indexed in the Web of Science with Impact Factor

[**A1**] [S1; NL] Sevcik, Aleksandras; Adliene, Diana; Laurikaitiene, Jurgita; Nedzinskiene, Ruta; Masiulyte, Ieva. Low energy deposition patterns in irradiated phantom with metal artefacts inside: a comparison between FLUKA Monte Carlo simulation and GafChromic EBT2 film measurements // Nuclear instruments and methods in physics research section B: Beam interactions with materials and atoms. Amsterdam : Elsevier. ISSN 0168-583X. eISSN 1872-9584. 2020, vol. 478, p. 142-149. DOI: 10.1016/j.nimb.2020.06.003. [Science Citation Index Expanded (Web of Science); Scopus] [IF: 1,377; AIF: 2,890; IF/AIF: 0,476; Q3 (2020, InCites JCR SCIE)] [M.kr.: T 008, M 001] [Indėlis: 0,200]

[**A2**] [S1; GB] Sevcik, Aleksandras; Laurikaitiene, Jurgita; Adliene, Diana. Quantitative comparison of different dosimetry methods in orthovoltage X-ray therapy // Radiation physics and chemistry. Oxford : Elsevier. ISSN 0969-806X. eISSN 1879-0895. 2022, vol. 197, art. no. 110128, p. 1-10. DOI: 10.1016/j.radphyschem.2022.110128. [Science Citation Index Expanded (Web of Science); Scopus] [IF: 2,900; AIF: 4,466; IF/AIF: 0,649; Q1 (2022, InCites JCR SCIE)] [M.kr.: N 002, M 001] [Indėlis: 0,334]

[**A3**] [S1; CH; OA] Sevcik, Aleksandras; Rinkevicius, Zilvinas; Adliene, Diana. Radiation-driven polymerisation of methacrylic acid in aqueous solution: a chemical events Monte Carlo study // Gels. Basel : MDPI. ISSN 2310-2861. 2023, vol. 9, iss. 12, art. no. 947, p. 1-13. DOI: 10.3390/gels9120947. [Science Citation Index Expanded (Web of Science); Scopus] [IF: 4,600; AIF: 5,200; IF/AIF: 0,884; Q1 (2022, InCites JCR SCIE)] [M.kr.: N 002, T 008] [Indėlis: 0,334]

Publications in other international databases and WoS Proceeding

[**B1** [P1a; LT; OA] Ševčik, Aleksandras; Adlienė, Diana. Polychromatic X-ray attenuation properties of normoxic polymers gels // Medical physics in the Baltic States: proceedings of the 14th international conference on medical physics, Kaunas, Lithuania, 7-9 November, 2019 / executive editor Diana Adlienė. Kaunas : Kaunas University of Technology. ISSN 1822-5721. 2019, p. 79-84. [Conference Proceedings Citation Index - Science (Web of Science)]

[**B2**] [P1a; LT; OA] Ševčik, Aleksandras; Adlienė, Diana. Monte Carlo simulated diagnostic X-ray dose distribution in a human voxel phantom with visualisation // Medical physics in the Baltic States: proceedings of the 13th international conference on medical physics, Kaunas, Lithuania, 9-11 November, 2017 edited by D. Adliene. Kaunas : Kaunas University of Technology. ISSN 1822-5721. 2017, p. 122-125. [Conference Proceedings Citation Index - Science (Web of Science)]

Other publications

1.[P1d; LT] Ševčik, Aleksandras; Adlienė, Diana. Comparison of experimentally measured dose depth distributions with MC simulations in electron-irradiated dose gels // Medical physics in the Baltic states: proceedings of the 15th international conference on medical physics, Kaunas, Lithuania, 4-6 November, 2021 / executive editor Diana Adlienė. Kaunas : Kaunas university of technology. ISSN 1822-5721. 2021, p. 163-166.

2. [T3; US] Ševčik, Aleksandras; Adlienė, Diana. Monte Carlo simulation of radiation-induced polymerization impact on dose gel properties // Materials info 2021: 2nd virtual congress on materials science & engineering: Theme: Outlining the importance of materials science for a better future, March 29-31, 2021: book proceedings. [S.l.] : [s.n.]. 2021, p. 55.

3. [T2; LT] Ševčik, Aleksandras; Adlienė, Diana. Application of Monte Carlo modelling for the assessment of various gafchromic films feasibility to record the dose distribution in non-homogeneous media // Advanced materials and technologies: book of abstracts of 22nd international conference - school, 24-28 August 2020, Palanga, Lithuania. Kaunas : Kaunas University of Technology. ISSN 1822-7759. 2020, A-P97, p. 125.

4. [T3; KZ] Adliene, D.; Sevcik, A.; Laurikaitiene, J. Comparison of the low energy deposition patterns for orthovoltage photon beam obtained using FLUKA Monte Carlo simulation and GafChromic RTQA2 film measurements // 20th international conference on radiation effects in insulators, 19 August - 23 August, 2019, L.N. Gumilyov Eurasian National University, Nur-Sultan (Astana), Kazakhstan: book of abstracts. Astana : Eurasian National University. 2019, P2-10, p. 163.

5. [T3; CZ] Sevcik, Aleksandras; Adliene, Diana. Comparative analysis of polymer gels as dosimetry tools for high dose rate brachytherapy using Monte Carlo simulations // COST action CA20129 "MultIChem": the 2nd conference "Multiscale irradiation and chemistry driven processes and related technologies" MultIChem 2023, Prague, Czech Republic, April 26-28, 2023: book of abstracts. Prague : [s.n]. 2023, p. 71.

ACKNOWLEDGEMENTS

The author of the dissertation would like to express gratitude to several individuals who have played pivotal roles in their academic journey. Firstly, sincere thanks go to Professor Dr. Diana Adlienė, the scientific supervisor, for her unwavering support and patience during the doctoral studies and dissertation preparation.

The author would like to thank medical physicists Dr. Jurgita Laurikaitienė from the Hospital of Oncology of Lithuanian University of Health Sciences for advising in experimental work.

The author also extends their appreciation to Professor Dr. Žilvinas Rinkevičius for his guidance and mentorship. His expertise has been instrumental in shaping the author's research.

I would also like to thank my wife, Irena, for her constant love, encouragement, and understanding. Her belief in me has always been a source of motivation and strength. Additionally, I am grateful to my son, Kajus Augustas, who was born in the last year of my PhD studies. His arrival brought great joy and has been a wonderful reminder of life outside my academic pursuits.

ANNEXES

1. Annex 1: source code of MC polymer growth model

The source code is publicly available at:
https://github.com/aleksandras-sevcik-edu/growpoli_alpha

UDK 615.849+544.54+678.744.33+544.773.432](043.3)]

SL344. 2021-*-*, * leidyb. apsk. l. Tiražas 14 egz. Užsakymas *
Išleido Kauno technologijos universitetas, K. Donelaičio g. 73, 44249 Kaunas
Spausdino leidyklos „Technologija“ spaustuvė, Studentų g. 54, 51424 Kaunas